



Geotechnical Extreme Events Reconnaissance

Turning Disaster into Knowledge

Sponsored by the National Science Foundation

July 22, 2014

The 22 March 2014 Oso Landslide, Snohomish County, Washington



Jeffrey R. Keaton, AMEC Americas (Team Leader – GEER Steering Committee)

Joseph Wartman, University of Washington (Team Leader)

Scott Anderson, Federal Highway Administration (GEER Steering Committee)

Jean Benoît, University of New Hampshire (GEER Member)

John deLaChapelle, Golder Associates, Inc.

Robert Gilbert, University of Texas, Austin (GEER Steering Committee)

David R. Montgomery, University of Washington

THE 22 MARCH 2014 OSO LANDSLIDE, SNOHOMISH COUNTY, WASHINGTON

List of Tables and Figuresiii

1. Introduction1

2. Geographic and Geologic Setting.....6

2.1 Physiography.....6

2.2 Geologic Setting7

2.3 Groundwater Setting8

2.4 Vegetation History10

3. CLIMATE AND PRECIPITATION26

3.1 Climate and Average Precipitation26

3.2 March 2014 Precipitation28

3.3 Flow in North Fork Stillaguamish River33

4. OSO LANDSLIDE BACKGROUND48

4.1 History of Landsliding along the North Fork Stillaguamish River Valley48

4.2 History of Slope Stability at the Oso (Hazel) Landslide Site49

4.3 Prior Slope Stability Analyses51

4.4 Subsurface Characterization52

4.5 Land-Use and Risk53

5. DATA COLLECTION FOR THE 22 MARCH 2014 LANDSLIDE69

5.1 Site stratigraphy69

5.2 Field Observations71

5.3 Discussion of Observations80

5.4 Seismic Signals Generated by the Landslide84

5.5 Eyewitness Accounts86

5.6 Impacts on the built environment90

6. HYPOTHESIZED MECHANISMS OF THE MARCH 22 LANDSLIDE128

6.1 Introduction128

6.2 Stage 1128

6.3 Stage 2133

6.4 Summary134

7. DISCUSSION141

7.1 Historical Context141

7.2 Empirical Predictions of Runout142

7.3 Influence of Forest Practices on Groundwater Levels and Slope Stability .145

7.4 Influence of Renewed Riverbank Erosion on Slope Stability147

7.5 Benchmarks for Risk148

8. CONCLUSIONS AND RECOMMENDATIONS159

8.1 The 22 March Oso, Washington Landslide159

8.2 Recommendations159

9. ACKNOWLEDGMENTS165

10. REFERENCES166

APPENDIX A: Field reconnaissance

LIST OF TABLE AND FIGURES

TABLES

Table 3.1.1 Location information for weather stations and stream gauge shown in Figure 3.1.1.

Table 3.2.1 Cumulative rainfall for March 1 to 22, 2014.

Table 3.2.2 Cumulative precipitation for periods in March 2014 at nearby gauges and at the Oso Landslide.

Table 5.2.1: Tree characteristics in areas 1 through 10 as defined in Figure 5.2.4

Table 5.3.2: Summary of Atterberg Limit Testing

Table 5.3.3: Tabulated summary of sieve analysis results.

Table 5.3.4 USCS Soil Classification

Table 5.3.5 Radiocarbon dates for material collected from exposures in the eastern lateral scarp of the 2014 Oso landslide.

Table 5.5.1 Summary of Eyewitness Accounts

Table 7.2.1 Regression coefficients for Equation 7-2 (adapted from Hungr et al. 2005).

Table 7.2.2 Parameters for empirical relationships of Legros (2002) in Equation 7-4.

Table 7.2.3 Predicted runout distances for 2014 Oso Landslide based on estimated total volume of 7.6 million cubic meters.

FIGURES

Figure 1.1 Site and vicinity map

Figure 1.2 The 22 March 2014 Oso, Washington Landslide

Figure 2.1.1 Physiographic provinces of Washington.

Figure 2.1.2 Topography in the vicinity of the Oso Landslide.

Figure 2.1.3 Slope inclination in the area around the Oso Landslide.

Figure 2.1.4 Valley width indexed to distance between the 200-m elevation contours.

Figure 2.2.1 Location of the 2014 landslide superimposed on geologic map of the Oso Landslide area.

Figure 2.2.2 Hillshade map of 2003 ground conditions. Base image from 2003 lidar data.

Figure 2.2.3 View of Oso Landslide and geologic exposures in scarps.

Figure 2.4.1 Aerial photograph of Oso Landslide area taken in 1933.

Figure 3.1.1 Map of the Oso Landslide region showing locations of selected weather stations and a stream gauge.

Figure 3.1.2 Monthly average precipitation data for four NWS cooperative weather stations and monthly precipitation values for January 2012 to March 2014.

Figure 3.1.3 Monthly precipitation values for three RAWS gauges for January 2012 to March 2014.

Figure 3.1.4 Daily and cumulative annual precipitation at three RAWS gauges in the vicinity of the Oso Landslide for 2012, 2013, and the winter months of 2014.

Figure 3.2.1 Cumulative precipitation preceding March 22, 2014, and associated return period at the Darrington Ranger Station gauge.

Figure 3.2.2 Daily and cumulative monthly precipitation recorded at Darrington and the three RAWS gauges during the first three months of 2014.

Figure 3.2.3 Exponential regression predicting rainrate (R_r) as a function of composite Doppler radar reflectivity (dBZ).

Figure 3.2.4 NEXRAD Reflectivity at the Oso Landslide on 19 March 2014 from 12:29 to 13:42 PDT.

Figure 3.2.5 Example of NEXRAD composite reflectivity showing highly variable conditions.

Figure 3.2.6 Composite precipitation diagram showing radar rainfall and gauge precipitation for the Oso Landslide and four gauge locations.

Figure 3.3.1 Discharge hydrograph of North Fork Stillaguamish River near Arlington, WA, January 2012 through March 2014.

Figure 3.3.2 Hydrograph of North Fork Stillaguamish River, January through March 2014.

Figure 3.3.3 North Fork Stillaguamish River stage showing effects of Oso Landslide dam.

Figure 3.3.4 Stillaguamish River stage showing effects of Oso Landslide dam and tidal influence from Puget Sound.

Figure 4.1.1 North Fork Stillaguamish River Valley (2003 lidar map).

Figure 4.1.2: Relative age classes of pre-2014 landslides in the immediate vicinity of the 2014 Oso Landslide.

Figure 4.1.3: Oso Landslide area 2003 lidar map.

Figure 4.1.4: Oso Landslide area 2013 lidar map.

Figure 4.1.5: Elevation differences between 2013 and 2003 lidar data sets.

Figure 4.1.6: Oso Landslide area 2014 lidar map.

Figure 4.1.7: Elevation differences between 2014 and 2013 lidar data sets.

Figure 4.1.8: Topographic Profile Section A-A'.

Figure 4.2.1 Historic Oso/Hazel Landslide disturbances and scarps from 1958 to 2013.

Figure 4.4.1 Reproduced boring logs from Shannon (1952).

Figure 4.5.1: Land-use at Time of Slide.

Figure 4.5.2: Land classified as geologically hazardous areas in vicinity of the slide.

Figure 5.2.1 Locations of key observations of GEER team during site reconnaissance.

Figure 5.2.2. Seeps along western (right) margin of the landslide.

Figure 5.2.3: Interpreted landslide zone map.

Figure 5.2.4 Photograph of Zone A1, recessional outwash and gray glacial till exposed in landslide headscarp.

Figure 5.2.5a: Photograph of Zone A2 as seen from top of landslide headscarp, view to south.

Figure 5.2.5b: Photograph of Zone A2 as seen from top of landslide headscarp; view to southwest.

Figure 5.2.6 Onlap of gray till in Zone A4 over eastern portion of the downed-tree-covered slump block of Zone A2.

Figure 5.2.7 Photograph of the eastern margin of Zone A; view toward northeast.

Figure 5.2.8 Rotational block field of Zone B seen from the air looking west.

Figure 5.2.9: Zone B slickensides in lacustrine clay.

Figure 5.2.10a. Oblique view of two approximately 100-ft-long (30 m) fallen trees (near the center of the image) that have been dragged downslope after they were felled. They indicate the extension in this part of the slide mass.

Figure 5.2.10b. Aerial view of indicator trees showing trails at least (45 m) 150 ft long showing skid marks from dragging. Location 48.28332, -121.84838.

Figure 5.2.10c. pair of track-like impressions in the loose sand indicate that the log impacted violently and bounced before coming to rest.

Figure 5.2.11: Lacustrine sediment exposed in western lateral margin in Zone B.

Figure 5.2.12 View looking northeast at sand ejecta deposits in Zone B near the Zone C interface.

Figure 5.2.13A Liquefied lacustrine sediments in Zone C.

Figure 5.2.13B Map showing locations where several actively flowing seeps along the eastern margin of the landslide correspond to the uppermost areas of Zone C.

Figure 5.2.14 Seepage and piping near interface between Advance Outwash sand overlying Glacial Lacustrine clay.

Figure 5.2.15: Hand auger boring (HA-3) into lacustrine material on the northern margin of Zone D.

Figure 5.2.16: Southern margin of Zone D (gray on left) overriding northern trailing margin of Zone E debris (brown on right).

Figure 5.2.17. View west at loose and sloughing channel slopes in glacial lacustrine deposits within the landslide in Zone D.

Figure 5.2.18 Preserved areas of intact forest floor in Zone E.

Figure 5.2.19 Tilted subvertical trees in Zone E.

Figure 5.2.20 Tumbled and broken trees in the impact zone between Stage 1 and Stage 2.

Figure 5.2.21 Typical gray veneer that appears to be a splash deposit.

Figure 5.2.23 Sub-vertical tree rafted into current location near HA-10.

Figure 5.2.24 View from north end of Zone F toward rafted deciduous trees in Zone E, in background.

Figure 5.2.25 Maple trees north of SR 530 that appear to be in place.

Figure 5.2.26 Typical sand ejecta deposit.

Figure 5.2.27 Typical sand boil.

Figure 5.2.28 Recreational vehicle (RV) at the distal edge of the flow.

Figure 5.2.29 Vehicle wrapped around tree as if pushed from the southwest.

Figure 5.2.30 Log that formed part of the log revetment constructed after the 2006 landslide and found in distal portion of Zone F (note steel cables).

Figure 5.2.31 Revetment logs with metal identification tags and drilled holes with steel cables being examined by GEER team members on May 23, 2014.

Figure 5.2.32 Asphalt with intact base course from SR 530 road bed plucked and transported by the debris flow. Note piece of asphalt in lower right with yellow paint stripe.

Figure 5.2.33 Drainage pipe and filter fabric from SR 530 transported to the southwest by initial debris flow.

Figure 5.2.34. Section of guard rail (top) and timber support (bottom) transported from SR 530 by initial debris flow.

Figure 5.2.35. Example of one of several Highway 530 pavement sections that were uplifted and transported by the landslide.

Figure 5.2.36 The travel vectors (vector from point of origin to depositional location) of identifiable materials.

Figure 5.3.1 Digitized trees and sections of trees within the landslide boundary.

Figure 5.3.2 Areas used for evaluating tree density within landslide boundary.

Figure 5.3.3 Example of tree density within area.

Figure 5.3.4 Tree density within landslide mass and runout.

Figure 5.3.5 Rose diagrams for each tree area shown in Figure 5.3.2.

Figure 5.3.6 Average tree azimuths for each area.

Figure 5.3.7: Varved clay test specimen.

Figure 5.3.8 Grain size distribution plot for data in Table 5.4.2.

Figure 5.3.9 Photographs of dried and sieved specimens.

Figure 5.4.1 Velocity-time histories generated by the Oso Landslide.

Figure 5.4.2: Landslide-generated velocity-time histories presented plotted as smoothed, high-pass filtered (<1 Hz), smoothed envelopes.

Figure 6.1.1: Schematic cross section (modified from A-A' from Figure 4.1.8) showing conceptualized 2006 and ancient slide surfaces (upper diagram).

Figure 6.1.2 Schematic cross section (modified from A-A' from Figure 4.1.8) with conceptualized boundaries of Stage 1 and Stage 2 shown by hatch marks.

Figure 6.1.3. Conceptual landslide stage map.

Figure 6.2.1 View of the distal zones of the deposit from the headscarp showing excavation of Highway SR 530 in the approximate center of the photograph.

Figure 7.2.1 Definition of angle of reach or fahrböschung (after McDougall, 2006).

Figure 7.2.2 Travel Angle versus Volume of Mass Movement (adapted from Jakob and Hungr 2005).

Figure 7.2.3 Relationship between volume and runout distance (after Legros, 2002).

Figure 7.2.4 Profile showing starting locations for Stage 1 and Stage 2 events at Oso.

Figure 7.4.1a Google Earth image from 7/2005.

Figure 7.4.1b Google Earth image from 3/2006

Figure 7.4.1c Google Earth image from 8/2005

Figure 7.4.1d Google Earth image from 4/2009.

Figure 7.4.1e Google Earth image from 6/2009.

Figure 7.4.1f Google Earth image from 9/2011.

Figure 7.4.1g Google Earth image from 7/2013.

Figure 7.5.1 Rough approximation of risk from landslides in 5-km stretch of North Fork Stillaguamish River Valley in vicinity of Oso compared with related benchmarks for human safety risk.

1.0 INTRODUCTION

The Oso Landslide struck the community of Oso, Snohomish County, Washington (Figure 1.1) on Saturday, 22 March 2014, at approximately 10:37 a.m. local time on a clear, sunny day. Winter precipitation in the region was generally high but not atypical for the Pacific Northwest. Still, the landslide occurred immediately after a three-week period that was marked by unusually high levels of rainfall locally. The Oso Landslide initiated within an approximately 200-m-high (650 ft) hillslope comprised of unconsolidated glacial and colluvial (i.e., previous landslide) deposits (Figure 1.2). It transitioned to a catastrophic debris flow (often referred to as a "mudslide") and rapidly inundated "Steelhead Haven," a neighborhood of approximately 35 single-family residences that was established in the 1960's. The debris flow separated into east and west segments as it traveled more than a kilometer (0.6 mi) across the valley floor. The overall size of the Oso Landslide was approximately 7.6 million cubic meters (~ 270 million cubic feet) [USGS 2014], placing it among the upper tier of mass movements that have occurred in Washington over recent decades. The slope at the location of the landslide has slid several times since the 1930's and also is the site of an ancient landslide. The most recent prior activity took place in 2006, when a landslide known as the "Hazel Landslide" occurred and blocked the North Fork Stillaguamish River. This 2006 landslide traveled over 100 m (300 feet), but came to rest before reaching the Steelhead Haven neighborhood.

The Oso Landslide's human toll was heart wrenching. The event claimed the lives of 43 people, making it the deadliest landslide event in United States history. Of the approximately 10 individuals who were struck by the landslide and survived, several sustained serious injuries. Many residents of the local community as well as members of search-and-rescue teams dispatched to the area in the days following the landslide have reported ongoing psychological distress as a result of the disaster. The landslide additionally caused significant economic losses, which Washington State officials have estimated to be more than \$50 million. The landslide completely destroyed the Steelhead Haven neighborhood, as well as several homes located off of the nearby State Highway 530. Approximately 600 m (~ 2,000 ft) of highway was buried under up to 6 m (20 ft) of debris, which closed this major east-west transportation route for over 2 months.

In addition to its tragic human toll, the Oso Landslide has a number of important aspects that make it a highly significant geologic disaster.

- 1) After its initiation, portions of the landslide transitioned into a rapidly moving debris flow that traveled long distances across the downslope floodplain. This aspect of the landslide appears to be largely responsible for the significant loss-of-life.
- 2) Topographic conditions in the area of the landslide are well documented in a series of high-resolution airborne lidar surveys taken before the 2006 landslide, after the 2006 landslide but before the 2014 landslide, and after the 2014 landslide. Analysis of these

data sets allows for high resolution mapping of the landslide source area and depositional zones, and for characterization of the hazard.

3) The landslide was recorded at several seismographic stations deployed as part of the Pacific Northwest Seismic Network. The recordings provide unique insight to the landslide's failure sequence and duration.

4) The landslide produced unique morphologic features that are rarely observed in the field. These include regions of "sand boils" within the distal portion of the landslide debris and high mud splashes on surviving trees and nearby ground.

5) Despite having no precipitation monitoring instruments onsite, rain and stream gauges in the vicinity and NEXRAD Doppler weather radar data make it possible to bracket the possible range of antecedent rainfall over a wide range of time intervals (days, months and years).

6) Eyewitness accounts of the landslide have been reported by multiple individuals who observed and survived the event, including several who were struck by and subsequently became entrained in the debris flow.

This report presents the findings of the National Science Foundation (NSF)-supported Geotechnical Extreme Events Reconnaissance (GEER) Association scientific research team that performed a field reconnaissance of the Oso Landslide beginning approximately 8 weeks after its occurrence. The GEER team consisted of interdisciplinary group of professionals with expertise in geology, geomorphology, engineering geology, hydrology, hydrogeology, risk assessment and geotechnical engineering. The primary goals of the GEER field reconnaissance were to document conditions at the landslide and to collect potentially perishable field data. The report primarily focuses on observations made and data collected at the landslide site, but also reviews regional and local geologic conditions, climatic setting, eyewitness accounts, local land-use and landslide risk assessment. Based on this information, preliminary hypotheses are proposed that addresses landslide initiation, mobilization, and subsequent runout behavior. This report is based largely on data collected during a four-day team reconnaissance across the entire landslide area in late May 2014, two months after the Oso Landslide occurred. Additional information was obtained from review of airborne lidar, aerial photographs, and satellite imagery; pre- and post-event photographs and videos (including ultra-high resolution gigapixel panoramic images), precipitation- and stream-gauge data, Doppler weather radar data, professional reports and articles, seismologic data, interviews with community officials and residents, media accounts, and limited laboratory testing. The field reconnaissance and data products are described in more detail in Appendix A.

The publication of this report two months after the field reconnaissance reflects GEER's commitment to timely and open dissemination of data and findings. Field access to the landslide

was granted to the GEER team shortly after search-and-rescue (SAR) and recovery activities had nearly concluded at the site. The SAR and recovery activities extended over a multi-week period due to the treacherous conditions at the site and the difficulty emergency response officials had in locating victims. The GEER investigation is not intended to be a final, conclusive study of the landslide; instead, it should be regarded as a preliminary assessment based on reconnaissance observations and other available data. It is recommended that additional research be conducted to test and challenge the interpretations and hypotheses presented in this report.

Figure 1.1 Site and vicinity map

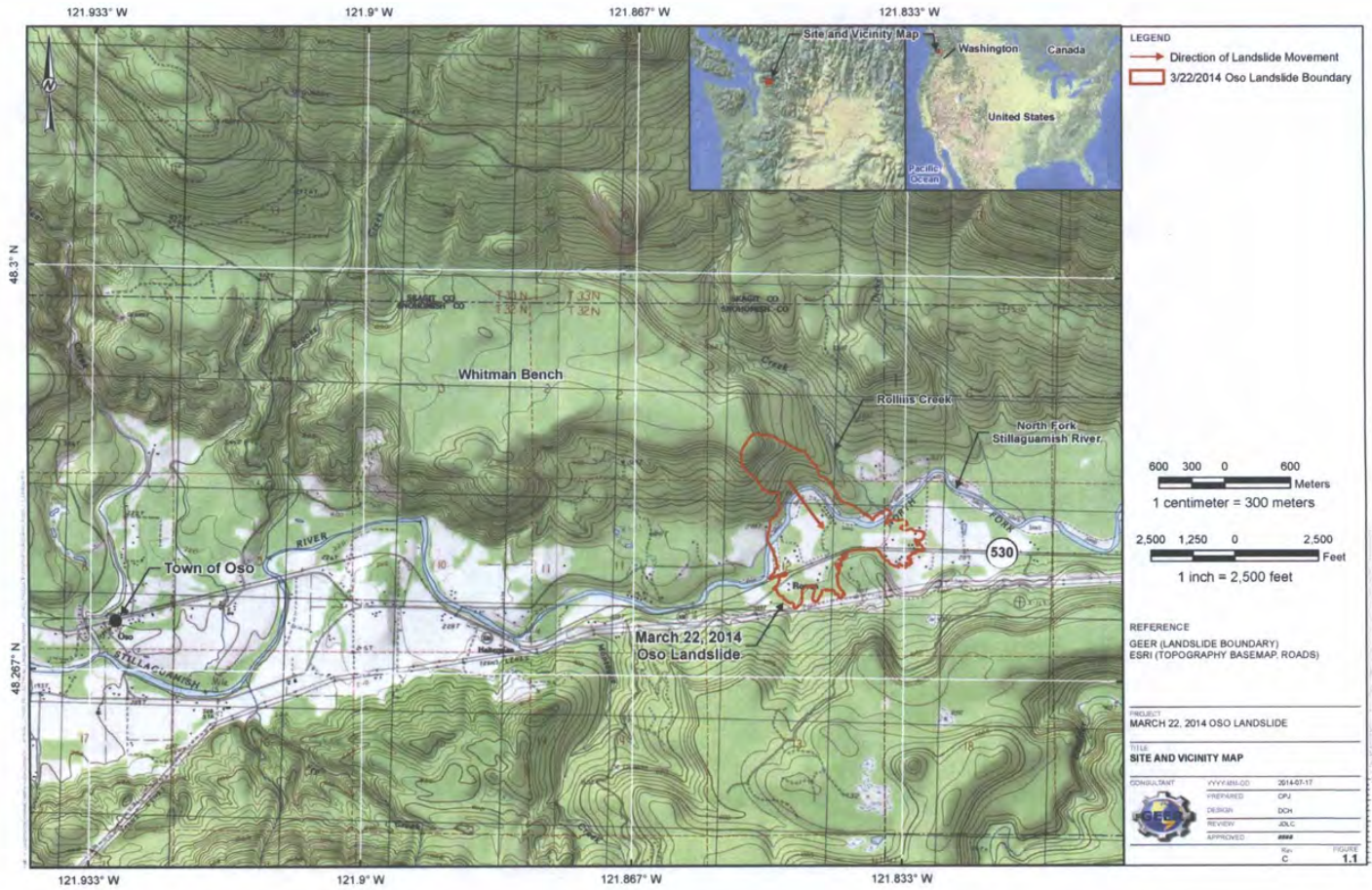




Figure 1.2 The 22 March 2014 Oso, Washington Landslide (photograph courtesy of the Washington Dept. of Transportation)

2. GEOGRAPHIC AND GEOLOGIC SETTING

2.1 Physiography

The Oso Landslide is situated in a west-trending valley within the northern Cascade Range physiographic province (Figure 2.1.1). The Cascade Range is a volcanic arc that hosts active volcanoes that exceed elevations of 3,000 m (~10,000 ft) above sea level (asl), with the most recent historical activity being the 1980 eruption of Mount St. Helens (west of Mt. Adams in Figure 2.1.1). The Puget Lowland province is immediately west of the Cascade Range.

Topographic conditions in the area around the Oso Landslide are dominated by major valleys surrounding mountains with ridges and some sharp peaks (Figure 2.1.2). Mountains in the southeast part of Figure 2.1.2 have peaks that rise to elevations of nearly 2,100 m (~6,900 ft) asl. The North Fork Stillaguamish River valley is east-west trending and the river flows to the west. The north-trending valley on the east side of Figure 2.1.2 is the Sauk River valley.

Slope inclinations in the area immediately around the Oso Landslide (Figure 2.1.3) are dominated by relatively gently sloping valley bottoms and prominent upland benches with strip-like zones of steep slopes running along the valley walls. Channels of the North Fork Stillaguamish River and Rollins Creek have cut down into geologic materials deposited by glaciers, pro-glacial streams, or in glacier-dammed lakes. The scalloped morphology of the valley side slopes is clearly visible in the map of slope inclination (Figure 2.1.3).

Whitman Bench is one of the upland benches defining a low-relief landscape element at an elevation of about 275 m (900 ft) at its eastern end, adjacent to the Oso Landslide, and between bedrock slopes to the north and the river valley to the south. An unnamed bench at the same elevation as Whitman Bench is located on the southern side of the valley in the southeast part of Figure 2.1.3 implying that in early post-glacial time the bench-forming deposits likely extended across the valley bottom. The scalloped shape of the valley sides, the low-relief upland benches, and the strip-like pattern of steeper slopes implies repeated rotational slope movements (referred to as “slumps”) that involved the full height of the valley-sides. The river elevation prior to the 2014 Oso Landslide was approximately 76 m (250 ft) asl, amounting to approximately 200 m (650 ft) of local relief at the site of the Oso Landslide.

The 250-m topographic contour in Figure 2.1.2 suggests that the Oso Landslide is in the narrowest location within the North Fork Stillaguamish River valley. A more detailed, yet simple, analysis of the valley width was performed using the 200-m contour lines. The width between the 200-m contours shows that the Oso Landslide occurred within a relatively narrow (i.e., 2 to 2.4 km wide; 1.2 to 1.5 mi), roughly 10-km (~6 mi) long valley reach (Figure 2.1.4). In such a relatively narrow valley reach the geomorphic effects of both lateral channel migration on valley-wall landsliding, and therefore landslide-induced shifts in river-channel position, would be expected to be more pronounced than in the wider valley reaches both upstream and downstream.

2.2 Geologic Setting

The Oso Landslide occurred at a location where earlier landslides had been documented along the North Fork Stillaguamish River near a location called Hazel on an old railroad line (east part of Figure 2.2.1). The river drains part of the west slope of the Cascade Range and is underlain by rocks of variable lithology including Jurassic metasedimentary, metavolcanic, and ultramafic rocks in the western portion and Tertiary sedimentary and volcanic rocks in its eastern portion (Dragovich et al., 2002). The seismically-active, left-lateral Darrington-Devils Mountain Fault is mapped as running through the 2014 landslide runout zone beneath the valley bottom (Dragovich et al., 2003). Surficial Quaternary deposits of glacial-fluvial outwash, till, and glacial-lacustrine silts and clays blanket bedrock and form extensive topographic surfaces into which the river incised and carved its modern valley during the Holocene. Preservation of relatively large terraces underlain by unconsolidated glacial-fluvial outwash above thick deposits of glacially-associated lacustrine silts and clays is typical of west-draining valleys in the northern Cascade Range (Tabor et al., 1988; Booth, 1989).

Whitman Bench is one such terrace (Figures 2.1.3 and 2.2.1) that probably was a continuous topographic surface across the North Fork Stillaguamish River valley and contiguous with a similar but unnamed bench at the time the glaciers receded. The scalloped valley walls below Whitman Bench and below the companion unnamed bench are the heads of landforms mapped as landslides by Dragovich et al. (2003).

Dragovich et al. (2003) mapped the site of the 2014 Oso Landslide as part of a massive landslide complex, with local in-place exposures of Olympia non-glacial sediments (fluvial sands where exposed at the base of the section), overlain in turn by Vashon stage advance lacustrine deposits and till, with Everson interstage recessional lacustrine and outwash deposits forming the top of the section and the topographic surface of the Whitman Bench. Dragovich et al. (2003) report two radiocarbon dates (ages) of $35,040 \pm 450$ b.p. and $38,560 \pm 640$ b.p. for detrital wood fragments collected from forest beds in well-sorted oxidized sands from an exposure of Olympia age fluvial sediments exposed at river-level along the right bank in the area that was to become the eastern margin of the 2014 Oso Landslide.

Dragovich et al. (2003) mapped extensive areas of landsliding along the valley of the North Fork Stillaguamish River upstream and downstream of the Oso Landslide. In a cross-section constrained by well logs, Dragovich et al. (2003) show that the modern valley bottom alluvium overlies deposits from older (Holocene) landslide complexes beneath the valley floor in the runout zone of the 2014 Oso Landslide (Figure 2.2.1 shows the cross-section location in the runout zone, but the cross-section example is for the prehistoric landslide complex covering the valley bottom immediately west of the Oso Landslide). A well boring at station W55 on the cross section in Figure 2.2.1 shows landslide deposits burying valley bottom alluvial deposits. Together the cross-sections on the Dragovich et al. (2003) geologic map indicate a history of

Holocene landslides on valley slopes with deposits locally accumulating on the valley bottom in the immediate vicinity of the 2014 Oso Landslide location.

The stratigraphy of the landslide site is disrupted below the elevation of the “ancient headscarp” apparent on the 2003 hillshade image (Figure 2.2.2). But the undisturbed section now exposed in the 2014 landslide headscarp (Figure 2.2.3), together with exposures on the landslide lateral margins, indicates that the site geology consists of deposits that are typical of the sequence found throughout the Puget Lowland. [Note that “headscarp” in this report would be called “main scarp” by Cruden and Varnes (1996).]

Following glacial retreat approximately 16,000 years before present (b.p.) in northern Puget Sound (Porter and Swanson, 1998), the Stillaguamish River incised into the glacial sediments, with an early post-glacial landscape characterized by a wide valley bottom with low-relief terraces and low-gradient tributaries (Beechie et al., 2001). Immediately after glacial retreat the land surface was about 200 m (~ 650 ft) lower than today (due to isostatic depression), sea level was about 90 m (300 ft) lower, and the river valley at Arlington was close to sea level (Beechie et al., 2001). Around 12,500 b.p., lahar deposits from an eruption of Glacier Peak diverted the Sauk River from its course as a headwater tributary to the Stillaguamish and redirected it to flow into the upper Skagit River, significantly decreasing the stream power of the North Fork Stillaguamish River (Dragovich et al., 2000).

Post-glacial evolution of the valley involved river incision and lateral channel migration undermining the valley walls. Incision of the glacially-associated valley filling deposits created conditions conducive to mass wasting, as recorded in the scalloped morphology of the valley walls. Lateral river erosion where the outside of meander bends impinged upon the base of valley walls contributed to instability that could produce large landslides capable of shifting the river to the far side of the valley, which could, in turn, destabilize the opposite valley wall. The resulting back and forth would have contributed to gradual valley widening to form the modern valley bottom. As shown in Figure 2.1.4, the area near the landslide is now the narrowest part of the valley.

2.3 Groundwater Setting

The groundwater setting of the Oso Landslide is poorly known in detail, but groundwater flow to the Oso Landslide is controlled generally by local topography and stratigraphy. The recessional outwash sand and gravel capping the local slope above the Oso Landslide and the advance outwash separating the glacial till and the glacial-lacustrine deposits are highly permeable, whereas the glacial till and glacial-lacustrine silt and clay formations are of much lower permeability. These differences in permeability create the potential for an unconfined aquifer perched on the glacial till and a confined aquifer between the till and glacial-lacustrine deposits. Evidence for local seeps along the recessional outwash/till contact was apparent on the headscarp face after the 2014 landslide during the field reconnaissance. In addition, active seepage and

associated hydrophyllic vegetation was observed at and over the topmost exposure of till seen along the trail leading down from the Whitman Bench on the east side of the Oso Landslide through Headache Creek (a tributary to Rollins Creek in Figure 2.2.2). Seepage from advance outwash and glacial-lacustrine deposits was also observed locally, as described later in this report.

A consulting report prepared in 1952 by Shannon and Associates identified two spring-fed streams within a landslide mass that apparently was active in 1949 and one spring-fed stream adjacent to the east of the landslide. The streams were assigned names in the Shannon and Associates report for discussion purposes: Slide Creek and Mud Flow Creek were used for the two spring-fed streams within the landslide, whereas Headache Creek was used for the spring-fed stream adjacent to the landslide. The Shannon and Associates report noted that land movements within the landslide had formed depressions that collect surface water, which can infiltrate into the mass of clay. The two streams within the landslide flowed year round at about ~1.6 L/s (25 gal/min), had made deep incisions into clay in the slide area, and were continuously carrying clay in suspension down to the river. Flow in Headache Creek was reported by Shannon and Associates (1952) at a more-or-less constant rate of ~14.2 L/s (225 gal/min). The Shannon and Associates report further notes that the landslide at the time their report was being prepared had progressed to within 45 m (150 feet) of Headache Creek.

Benda et al. (1988) reviewed the Shannon and Associates (1952) report and identified two primary groundwater source areas, which they interpreted, to be feeding springs within the Hazel landslide. The first groundwater source was identified as the ground surface above an aquifer that exists approximately 210 m (700 ft) below the Whitman Bench and includes the hillside adjacent to the Bench; this area is identified in a sketch included in the Benda et al. (1988) report as the area adjacent to and above the Hazel landslide scarp and extending a relatively short distance onto the Whitman Bench beyond the limits of the prehistoric landslide. The second groundwater source was identified as slopes below Whitman Bench within the Headache Creek drainage basin.

Benda et al. (1988) interpreted a series of springs emerging on the western half of the Hazel landslide as indication of a horizontal aquifer being fed by the first groundwater source. They noted that the first groundwater source did not feed springs in the eastern half of the Hazel landslide directly because of the topography of the slope and the horizontal orientation of the aquifer. Benda et al. (1988) noted that the first groundwater source supplied some water to the second groundwater source in the Headache Creek drainage basin, but that the Headache Creek aquifer was separate because groundwater emerges as springs at different elevation than those on the west side of the Hazel landslide. They further noted that the Headache Creek aquifer supplies groundwater to the springs that emerge on the eastern half of the Hazel landslide. The Headache Creek drainage basin was recognized having major landslide deposits which resulted in the aquifer being complicated and leaking groundwater into the eastern part of the Hazel landslide. Benda et al. (1988) state that the Headache Creek aquifer is results in springs in the Hazel landslide that are "responsible for past and present mudflow activity."

Miller and Sias (1997) performed groundwater flow modeling using MODFE and evaluated effects of clear cutting on groundwater recharge to the Oso Landslide. The groundwater model assumed that recharge occurred primarily through infiltration into outwash sand on Whitman Bench and the slope itself perching on lacustrine clay and moving laterally to discharge on the slope. Sensitivity analyses of the effect of tree cover and clear cutting were included in the groundwater flow modeling.

Some groundwater recharge may occur from Rollins Creek into advance outwash deposits at a location about 1 km (0.6 mi) north of the Oso Landslide. At this location, the elevation of Rollins Creek should be within the elevation range of the advance outwash deposits. The area was not visited during the field reconnaissance, and no further information about recharge at this location is available at this time.

2.4 Vegetation History

The native forest community is typical of the *Tsuga heterophylla* Zone (Western Hemlock Zone), consisting of dense old-growth stands of Douglas fir (*Pseudotsuga menziesii*), western hemlock (*Tsuga heterophylla*), and true fir (*Abies* spp.) (Franklin and Dyrness, 1973). The earliest available aerial photographs, from 1933, show evidence of contemporary logging activity to the west on the Whitman Bench and the lower valley wall. In this image, shown in Figure 2.4.1, the area north of the 2014 landslide, and the Headache Creek basin both appear covered in mature timber, whereas the lower portion of the slope appears to be covered in immature or deciduous vegetation suggestive of either prior disturbance or conditions too wet for conifers. Miller and Sias (1997) report that an extensive area of timber harvest apparent on 1965 aerial photographs adjacent to the Hazel slide in the neighboring Headache Creek watershed immediately adjacent on the East side of the Oso Landslide occurred around 1960. Based on a sequence of aerial photographs presented in Miller and Sias (1997; 1998) extensive forest harvest on the Whitman Bench occurred in the vicinity of the Oso Landslide sometime between 1987 and 1991 with further harvest in 2006-2007 based on photos viewed on Google Earth (Figure 2.4.2A through F). A smaller, 7 acre, triangular area was clearcut in 2004 (visible in Figure 2.4.2E, Image 20050731 but not in Figure 2.4.2D Image 20030721) in the area immediately upslope of the area that failed in 2006.

Aerial photographs were obtained from USGS Earth Explorer website (<http://earthexplorer.usgs.gov/>) and Google Earth for the area in the immediate vicinity of the Oso Landslide (Figures 2.4.2A through 2.4.2F). The earliest aerial photo was taken in 1933, as described above (Figure 2.4.1 and 2.4.2A). An aerial survey of part of the North Fork Stillaguamish River valley was performed on July 9, 1941 (Figure 2.4.2A) to the west of the Oso Landslide area. Features in the 1941 photograph suggest that logging had been active on Whitman Bench prior to the date of the photograph. An aerial oblique photograph was taken in

May 1949 and used with annotations in Shannon and Associates (1952) (Figure 2.4.2B). This image indicates that substantial logging had occurred on the north side of Rollins Creek to the north of the Oso Landslide location. The topographic map used in the Shannon and Associates (1952) report identifies an "area being logged" in September through December 1951 that is situated just upslope of the active scarp of the Hazel landslide (Figure 2.4.2A). This area being logged in 1951 is on the prehistoric landslide that reactivated to some extent in 2006 and completely in 2014. An aerial photograph taken on August 13, 1953 (Figure 2.4.2A) shows some evidence of logging in the Oso Landslide vicinity but it does not appear to indicate areas of substantial clearcutting.

A photograph taken on 1 September 1974 (Figure 2.4.2C) shows a distinctive rectangular area of clearcutting to the west of the Oso Landslide location, an irregular area of logging to the north-northwest of the landslide location, and a nearly rectangular clearcut area to the east of the landslide location. By 16 July 1979 (Figure 2.4.2C), the features in the 1974 aerial photograph are mostly subdued.

False-color infrared photographs taken on July 26, 1985 (Figure 2.4.2D) show a nearly square area of clearcutting west of the Oso Landslide location, as well as texture in the images that suggest past logging areas. A photograph taken four years later on 5 September 5 1989 (Figure 2.4.2D) shows substantial areas of clearcutting to the northwest of the Oso Landslide location and four adjacent smaller areas to the north of the landslide location on the Snohomish-Skagit County boundary.

The next aerial photograph that was available was taken on July 21, 2003 (Figure 2.4.2D). Areas of clearcutting visible in the September 5, 1989 photograph appear in the 2003 photograph to have been enlarged probably during the 1990s. The area closest to the head of the Oso Landslide location in the 1989 photograph appears to be substantially the same 14 years later in 2003.

A relatively small triangle-shaped area of clearcutting is visible on Whitman Bench in the aerial photograph taken on July 31, 2005 (Figure 2.4.2E) northwest of the Oso Landslide location. Other noticeable areas of clearcutting in the 31 July 2005, photograph are near the east edge of the image in Figure 2.4.2E, on the east side of Rollins Creek and more than 1 km (3,300 ft) from the Oso Landslide location.

The Hazel landslide occurred in January 2006, and its features are visible in the aerial photograph taken on 31 March 2006 (Figure 2.4.2E). The character of the channel of the North Fork Stillaguamish River at the toe of the slope where the Hazel landslide occurred is noticeably different in the two images. Clearcutting at a location on the east side of the 2006 image has been enlarged relative to the shape of clearcutting in the 2005 photograph. A photograph taken on August 27, 2007 (Figure 2.4.2E) shows a pattern of clearcutting on the northeast side of Rollins Creek, but no noticeable change near the Hazel landslide location.

A photograph taken on 25 June 2009 (Figure 2.4.2F) shows little change relative to the 2007 image in Figure 2.4.2E). A photograph taken on 25 September 2011 (Figure 2.4.2F) shows clearcutting northwest of the Hazel landslide on the west edge of the photograph straddling the Snohomish-Skagit County boundary. Two small areas of clearcutting are visible in a photograph taken on 14 July 2013 (Figure 2.4.2F) north of the triangle-shaped area of clearcutting that was visible on Whitman Bench in the aerial photograph taken on 31 July 2005 (Figure 2.4.2E) northwest of the Oso Landslide location. The photograph taken on 31 March 2014 (Figure 2.4.2E) was after the Oso Landslide occurred; vegetation changes are not apparent between the 2013 and 2014 photographs. The head of the Oso Landslide intersects the southeast tip of the triangle-shaped area of clearcutting that was first visible in the 2005 photograph. A correlation between clearcutting timber and landslide activity does not appear to be indicated by the aerial photographs presented in the Figure 2.4.2 series. Conversely, it is clear that large landslides mapped by Dragovitch et al. (2003) in the vicinity of the Oso Landslide and shown in Figure 2.2.1 pre-date logging activities in this region.



Figure 2.1.1 Physiographic provinces of Washington. Modified from http://www.dnr.wa.gov/Publications/ger_geol_map_washington_pagesize.pdf

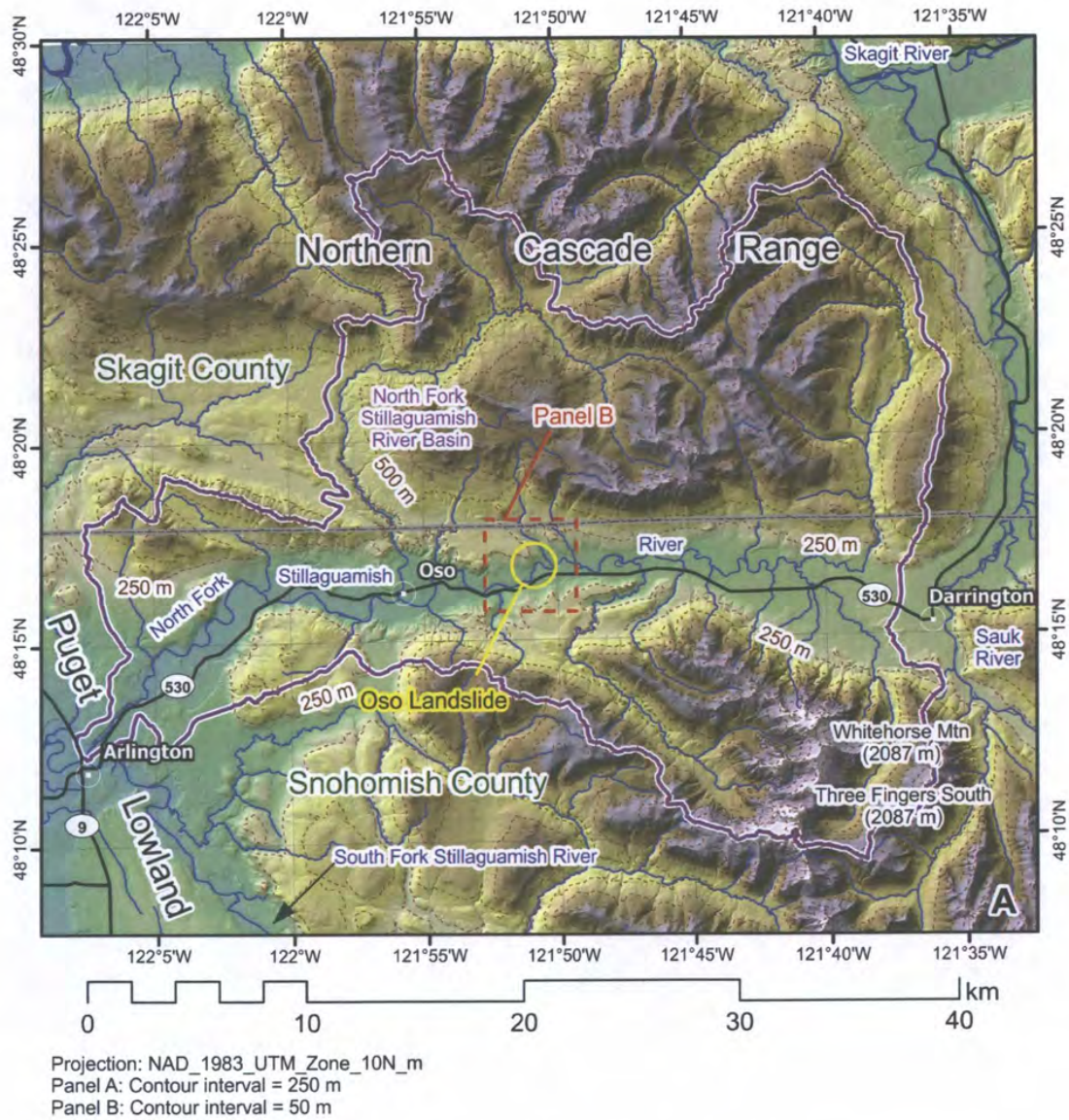


Figure 2.1.2 Topography in the vicinity of the Oso Landslide.

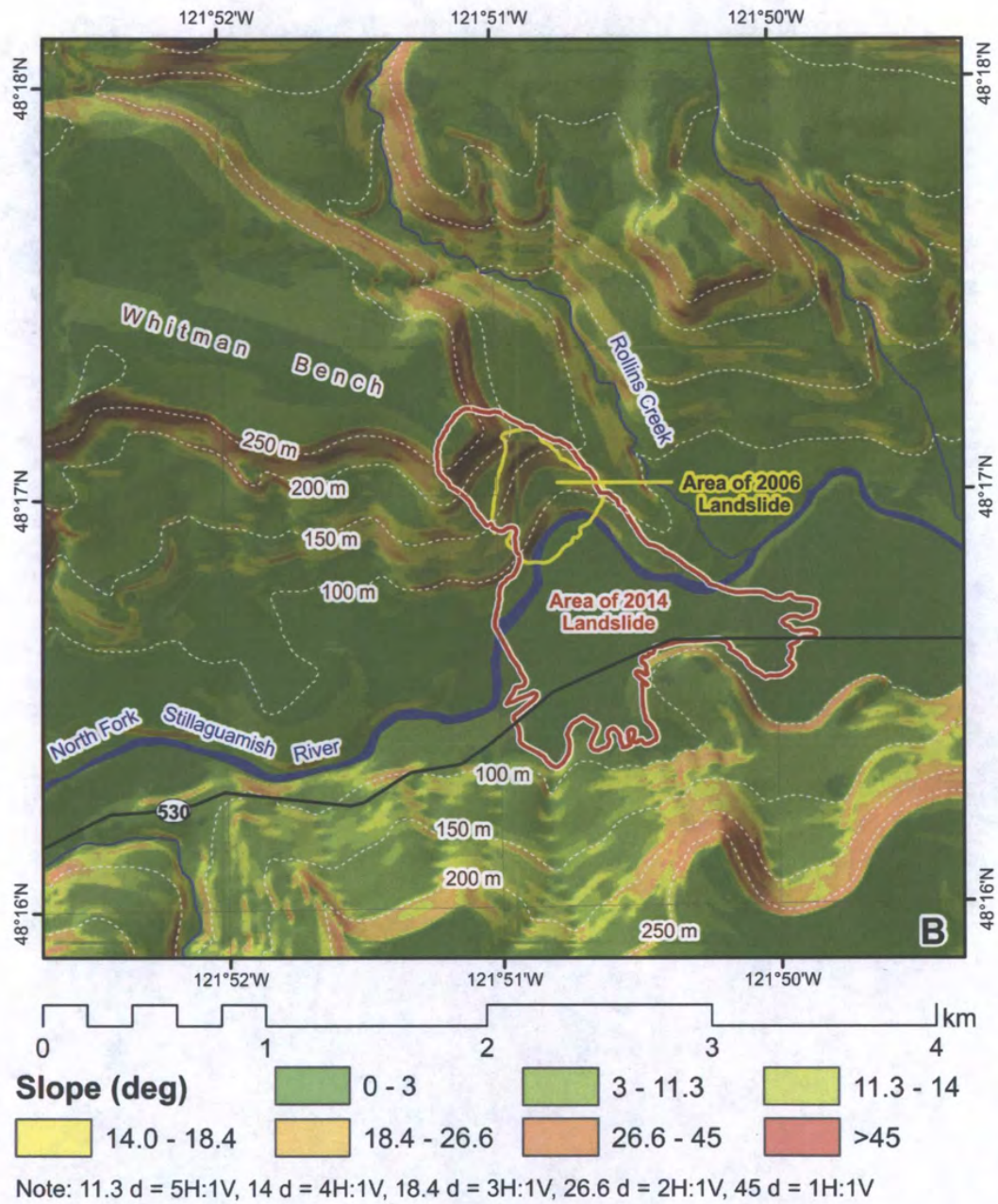


Figure 2.1.3 Slope inclination in the area around the Oso Landslide (red outline).

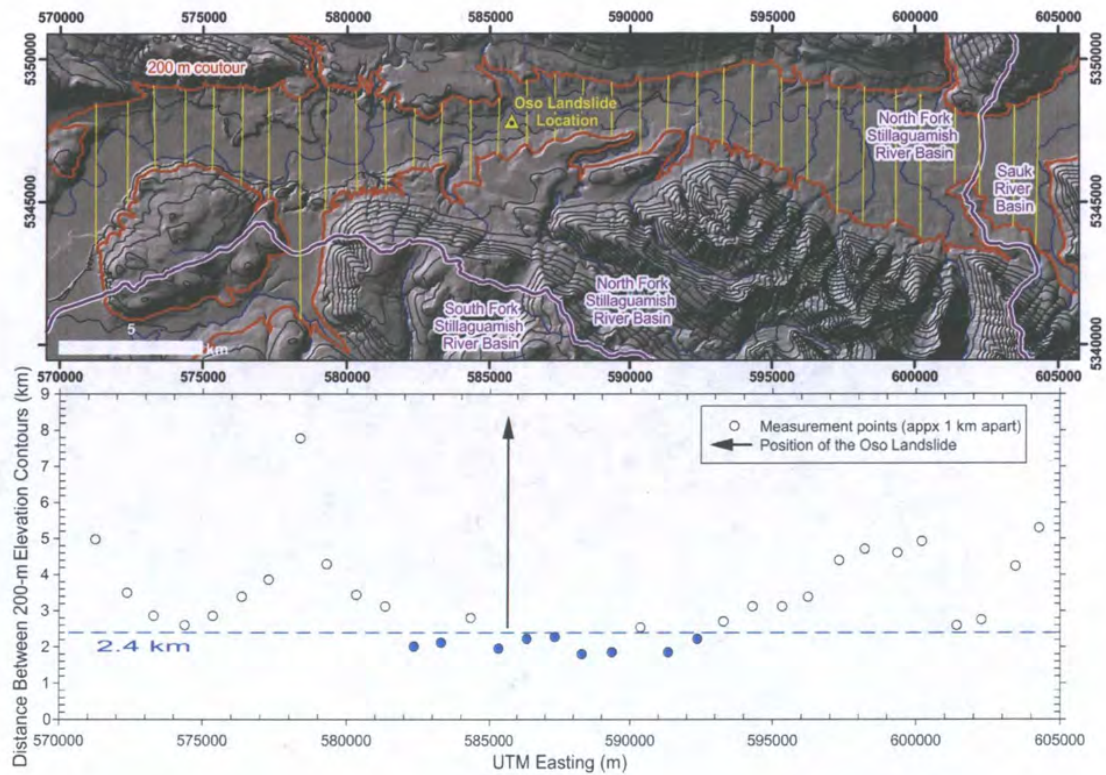


Figure 2.1.4 Valley width indexed to distance between the 200-m elevation contours (narrowest part of the valley width index is indicated by blue circles).

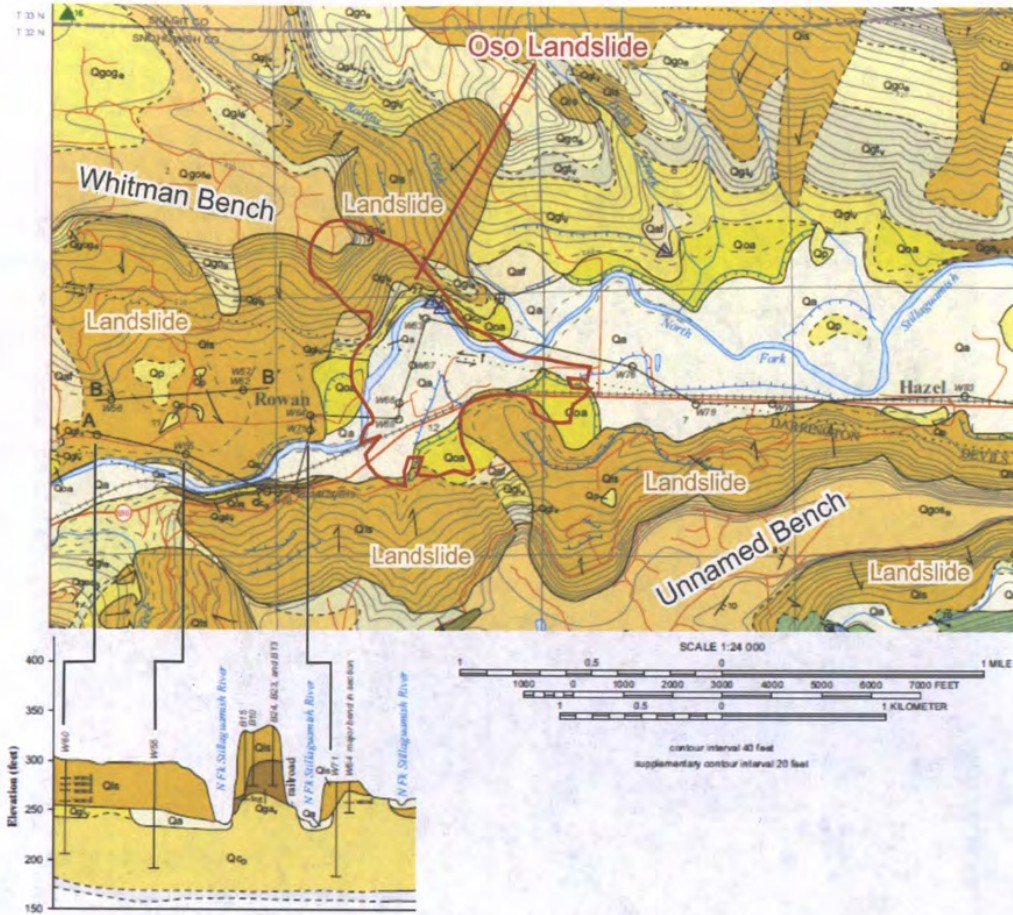


Figure 2.2.1 Location of the 2014 landslide superimposed on geologic map of the Oso Landslide area (from Dragovich et al., 2003). For the complete map and explanation of units and symbols, see http://www.dnr.wa.gov/Publications/ger_ofr2003-12_geol_map_mounthiggins_24k.pdf.

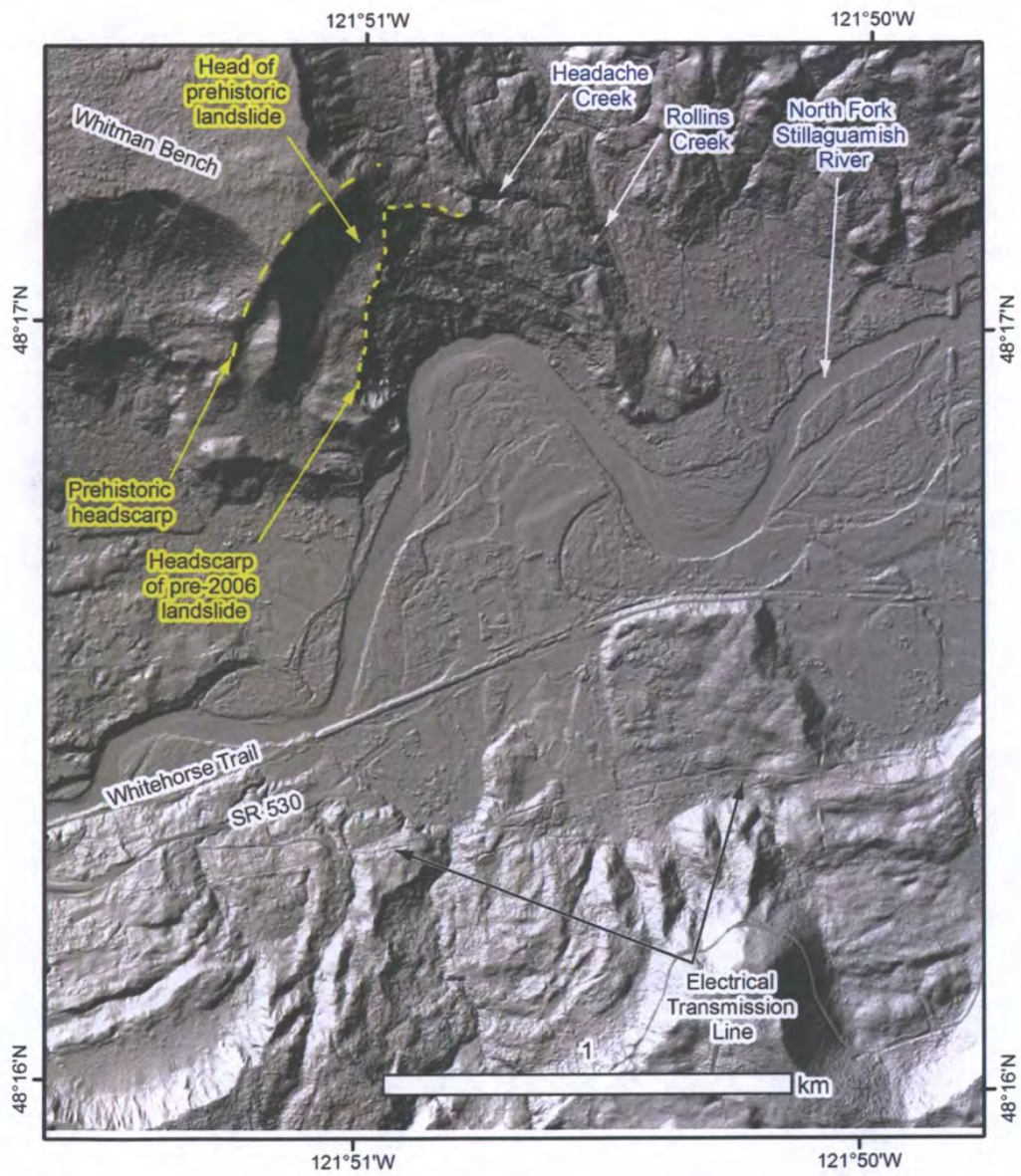


Figure 2.2.2 Hillshade map of 2003 ground conditions. Base image from 2003 lidar data.

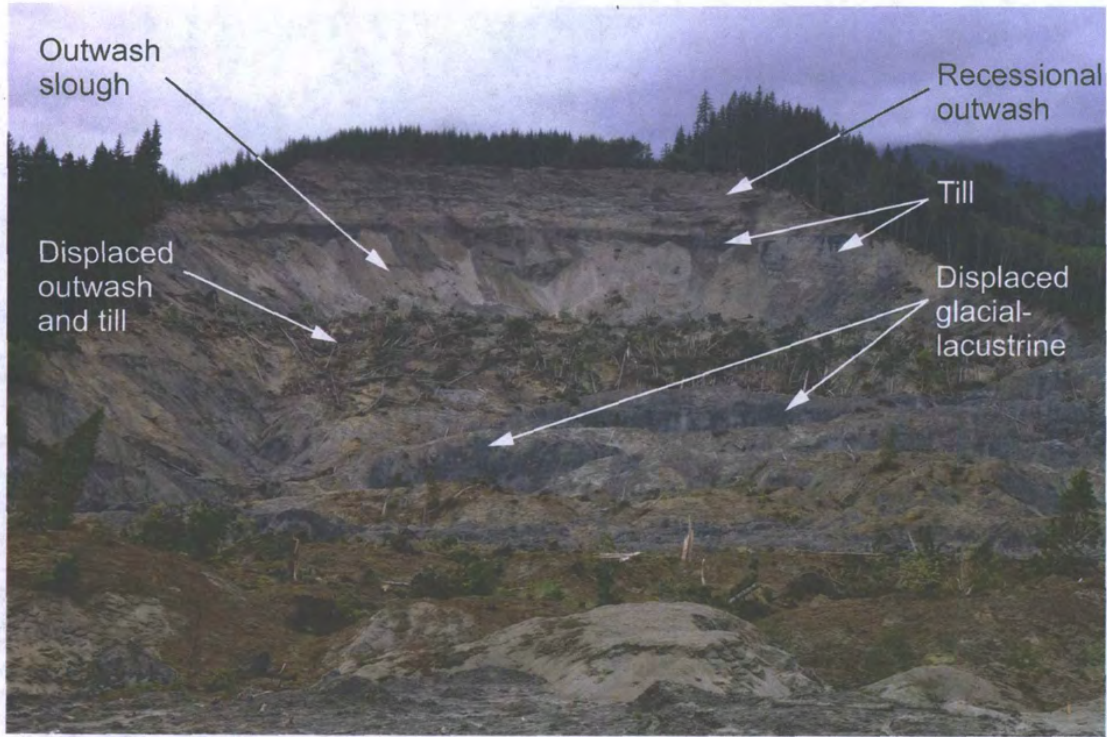
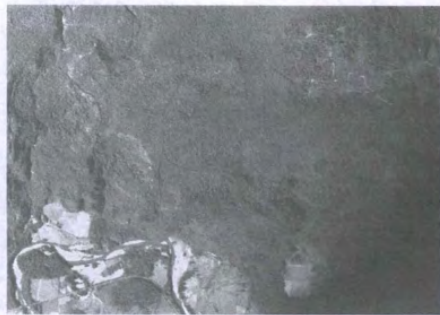


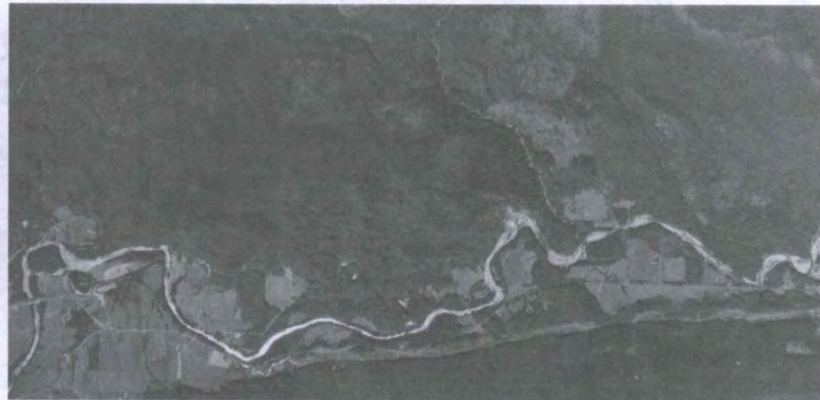
Figure 2.2.3 View of Oso Landslide and geologic exposures in scarps.
Camera position: 48.27690°N, -121.83967°W; view direction: 327°.



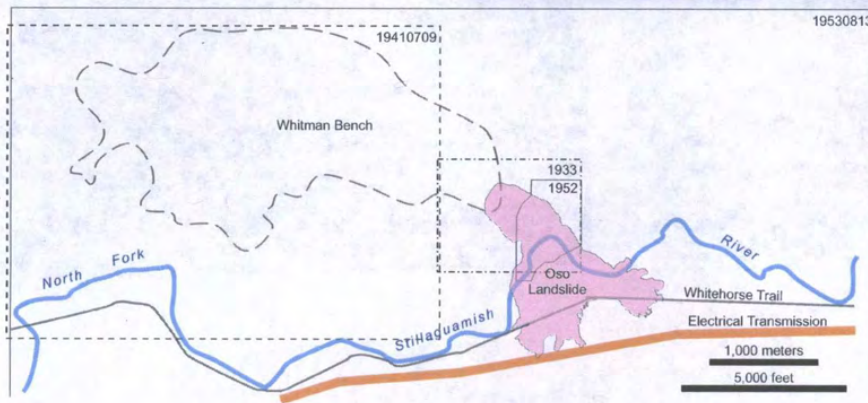
Figure 2.4.1 Aerial photograph of Oso Landslide area taken in 1933.



19410709



19530813



1933



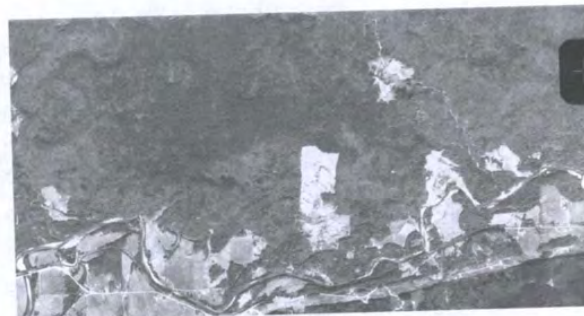
1952

- Notes:
- 1) Date of image in YYYYMMDD (e.g., 19530813)
 - 2) Scales of images vary
 - 3) Outlines of images on location map are approximate
 - 4) See text for discussion

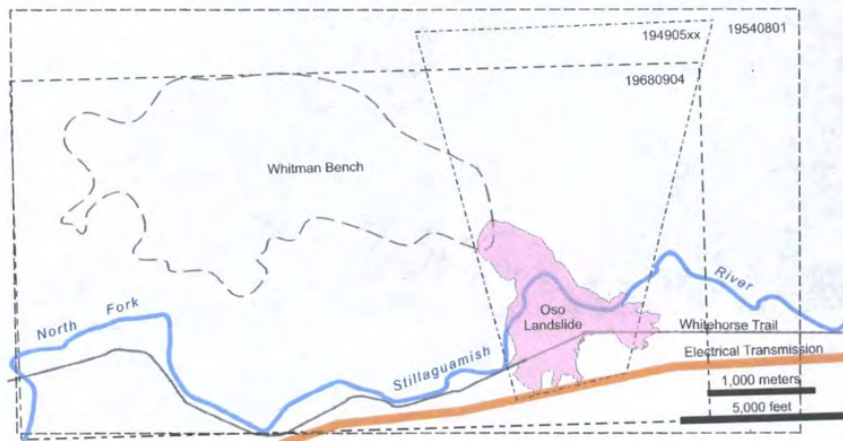
Figure 2.4.2A. Images showing features indicating forest harvest (1933, 1941, 1952, 1953)



19540801



19680904



194905xx

1) slide area in May 1949; 2) North Fork Stillaguamish River; 3) Rolland (Rollins) Creek; 4) county road; 5) Northern Pacific Railroad. From Shannon & Associates (1952).

Figure 2.4.2B. Images showing features indicating forest harvest (1949, 1954, 1968)

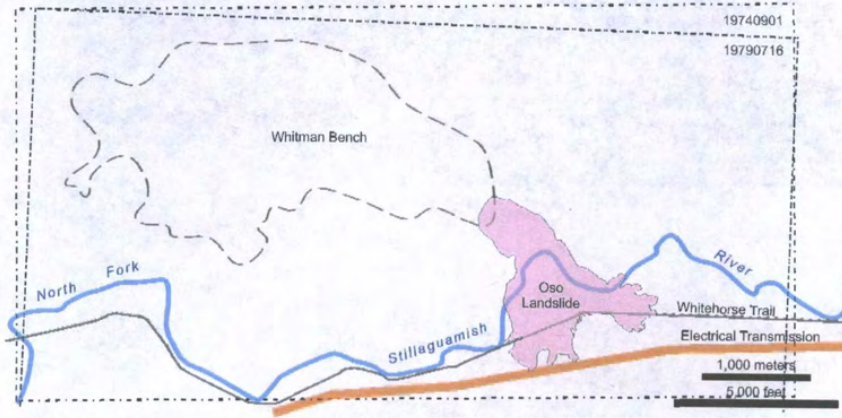
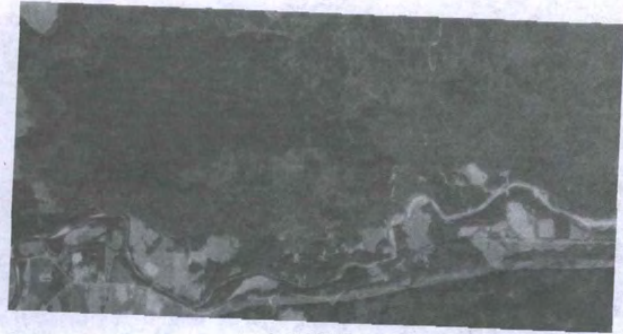


Figure 2.4.2C. Images showing features indicating forest harvest (1974, 1979)

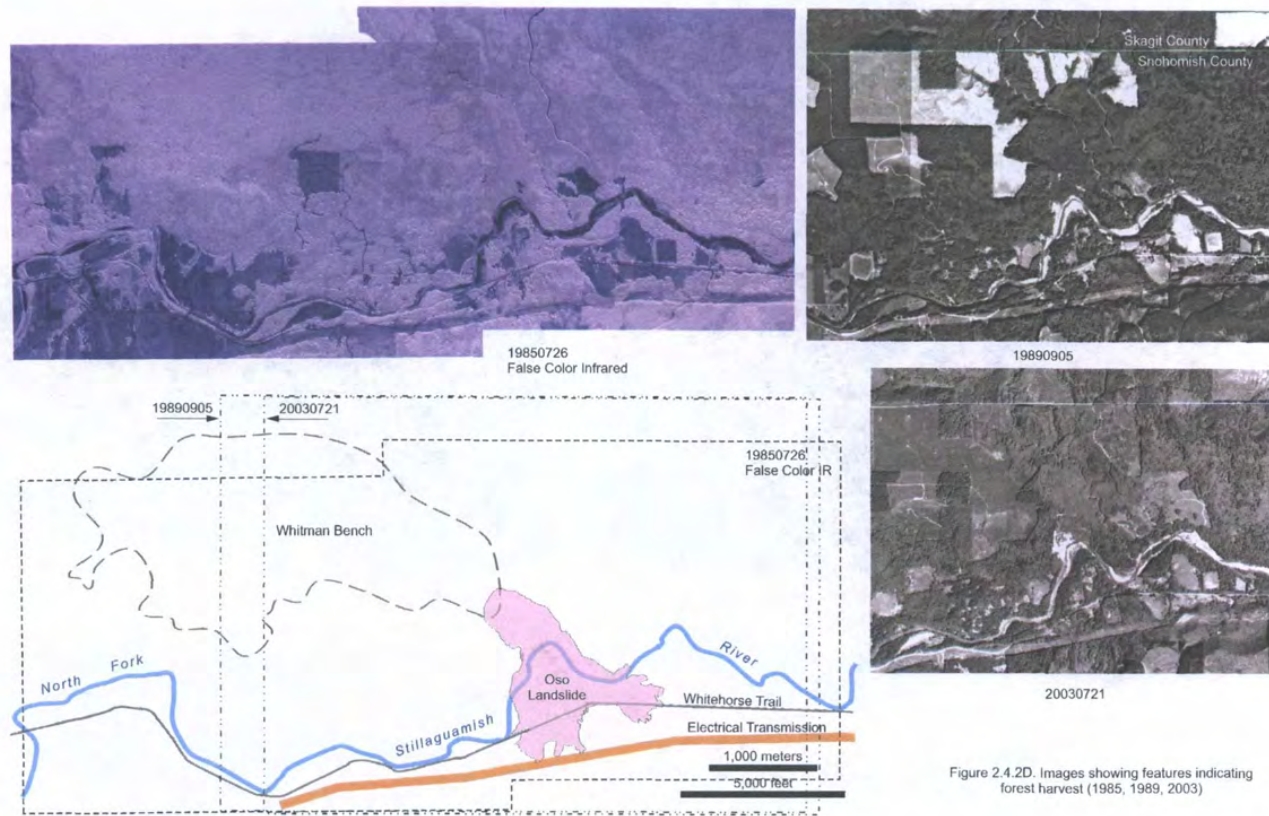


Figure 2.4.2D. Images showing features indicating forest harvest (1985, 1989, 2003)

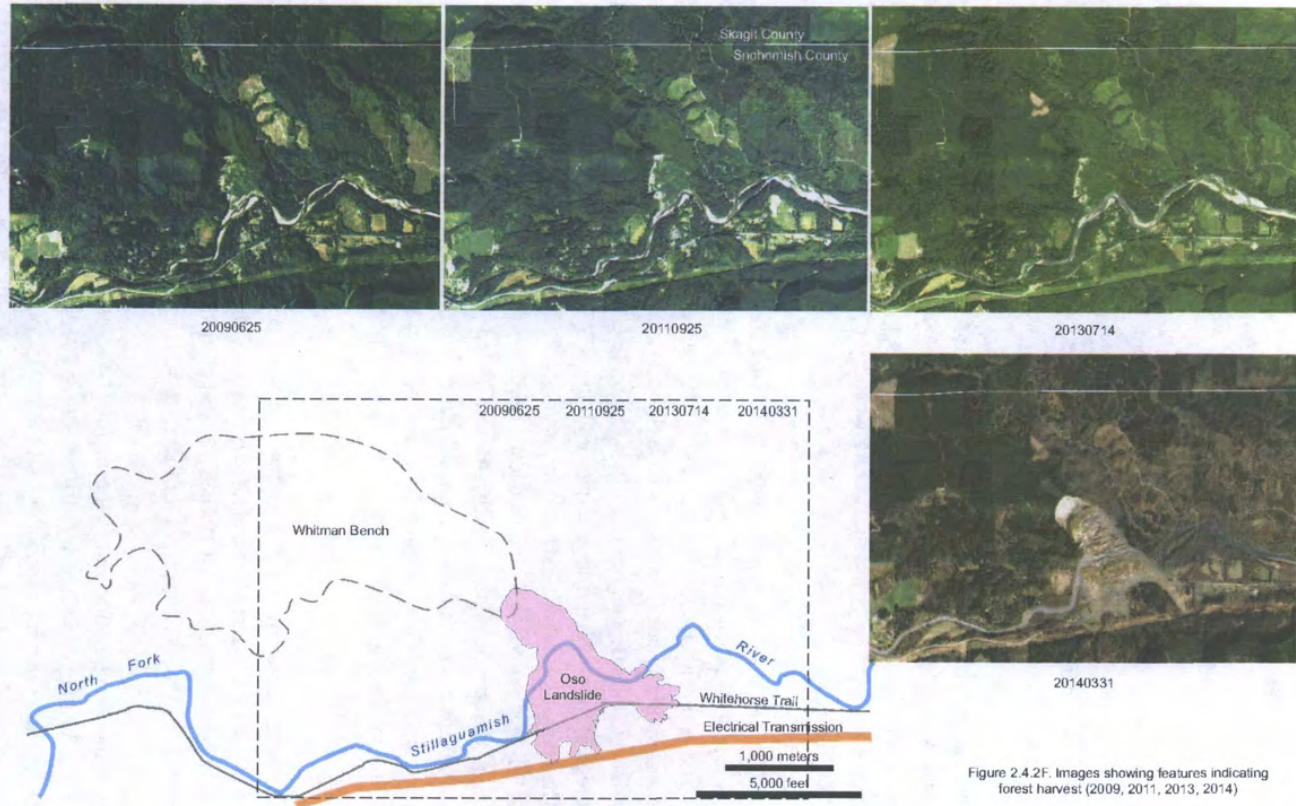


Figure 2.4.2F. Images showing features indicating forest harvest (2009, 2011, 2013, 2014)

3. CLIMATE AND PRECIPITATION

3.1 Climate and Average Precipitation

The Köppen-Geiger climate classification for the Snohomish County area is Cfb (Kottek et al. 2006), which denotes warm temperate climate, fully humid precipitation, and warm summer temperature. The nearby higher mountains in the Cascade Range are classified as Dsb, which denotes snow climate, summer dry precipitation, and warm summer temperature.

A regional meteorological phenomenon that affects the southern part of Snohomish County south to the north part of Seattle is called the Puget Sound Convergence Zone. It is a westerly air-flow pattern that is split by the Olympic Mountains and converges over Puget Sound. This air-flow convergence zone generally produces narrow bands of precipitation caused by updrafts and convection.

A considerable amount of precipitation data is available for the Oso Landslide region. Locations of four National Weather Service (NWS) cooperative weather stations coordinated by National Oceanic and Atmospheric Administration (NOAA) are shown in Figure 3.1.1, along with three Remote Automatic Weather Stations (RAWS) operated by the US Forest Service (USFS) in cooperation with the Bureau of Land Management (BLM) and one stream gauge operated by the US Geological Survey that is reported through the NWS. Location information is listed in Table 3.1.1. The NOAA cooperative stations are used to calculate average precipitation on a monthly basis for 30-year periods ending on a decade (e.g., 1981 to 2010). The base map in Figure 3.1.1 is the average March precipitation for the 30-year period 1981 to 2010.

(<http://datagateway.nrcs.usda.gov/>). It can be seen that the average March precipitation varies with elevation. At the Oso Landslide, the average March precipitation is 150 mm (6 inches), whereas the nearby higher elevation areas receive between 280 and 510 mm (11 and 20 inches) in an average March.

Monthly average precipitation data for the four NWS cooperative stations were obtained from the Western Regional Climate Center at <http://www.wrcc.dri.edu/summary/Climsmwa.html> for two 30-year periods (1971-2000 and 1981-2010) and plotted in Figure 3.1.2. Three of the four stations also have monthly statistical values for the 25th, 50th, and 75th percentile precipitation.

Monthly actual precipitation values for the four NWS cooperative stations also are plotted in Figure 3.1.2 for the period January 2012 to March 2014. Highlighted with yellow in Figure 3.1.2 are actual monthly precipitation values for the fall (September to December) 2013 and the winter (January to March) 2014. It can be seen that September 2013 was wetter than the 1981 to 2010 monthly normal precipitation, whereas October, November, and December 2013 were dryer than normal. January and February 2014 precipitation was approximately normal for the four gauges. March 2014 precipitation was normal for the Everett gauge, and above normal for the other three gauges. Precipitation at the Concrete Fish Station gauge was slightly higher in March 2014 than it

was in March 2012 and considerably higher than it was in March 2013. Precipitation at the Darrington Ranger Station gauge was higher in March 2014 than it has been in any other month during the period of record for that gauge. Note that the Darrington Ranger Station gauge is read manually each day at 8:00 AM and recorded on a paper form for each month. The monthly total precipitation data through February 2014 were available online; the handwritten daily precipitation values for January through March 2014 were provided to the GEER team by the Ranger Station following our request for a copy of the data.

Table 3.1.1 Location information for weather stations and stream gauge shown in Figure 3.1.1.

No.	Name (NWS ID)	North Latitude	West Longitude	Elevation (ft/m)
1	Everett (C00452675)	47.9752	-122.1950	18 / 5
2	Arlington (C00450257)	48.2005	-122.1280	30 / 9
3	Concrete PPL Fish Station (C00451679)	48.5397	-121.7422	59 / 18
4	Darrington Ranger Station (C00451992)	48.2600	-121.6036	168 / 51
5	NF Stillaguamish River (USGS. 12167000)	48.262	-122.046	89 / 27
6	Marblemount (451504)	48.539	-121.446	357 / 109
7	Finney Creek (451509)	48.403	-121.790	1900 / 579
8	Gold Hill (451613)	48.200	-121.500	3400 / 1036

Monthly actual precipitation values for three RAWS gauges are plotted in Figure 3.1.3 for the period January 2012 to March 2014. Several months in Figure 3.1.3 have “Missing data” notations to indicate that the plotted values probably under represent the actual precipitation depth summed for the month; the color of the notation indicates the year in which the data are missing. Highlighted with yellow in Figure 3.1.3 are monthly precipitation values for the fall (September to December) 2013 and the winter (January to March) 2014. September and November 2013 were wetter than October and December 2013 for all three gauges. Marblemount and Gold Hill gauges show January and February 2014 to be comparable to prior years; March 2014 is high for all gauges.

Daily precipitation and cumulative annual precipitation for the period from January 2012 through March 2014 at the same three gauges shown in Figure 3.1.3 are compared in Figure 3.1.4. Months with missing daily precipitation values are noted in Figure 3.1.4 in the same way as used in Figure 3.1.3. The date that the Oso Landslide occurred is noted with a red arrow and date; a horizontal dashed red line was positioned to intersect the cumulative precipitation curve on 22 March 2014. The cumulative precipitation at the Gold Hill gauge in 2012 reached the 22 March 2014, depth (771 mm, 30.36 in) on 20 April; whereas in 2013, the 22 March 2014, depth was

reached on 17 May; missing data intervals in the Gold Hill record do not affect the comparative dates.

The cumulative precipitation at the Finney Creek gauge in 2012 reached the March 22, 2014, depth (46.68 in, 1186 mm) on June 22, whereas in 2013, the March 22, 2014, depth was reached on September 17. Missing data in the Finney Creek record in January 2012 and January 2013 suggests that the March 22, 2014, depth might have been reached in late May 2012 and possibly as early as in June 2013. The Marblemount gauge in 2012 reaches the March 22, 2014, depth (37.42 in, 950 mm) on June 7, whereas in 2013, it reaches the same depth on May 21. Missing data in March 2012 suggests that the March 22, 2014, depth might have been reached at the Marblemount gauge in mid-May 2012.

Comparison of precipitation depths recorded in 2012 and 2013 to the first three months of 2014 in Figures 3.1.2, 3.1.3, and 3.1.4 indicates consistently that March 2014 was wetter than the same month in previous years. The precipitation depths suggest that the months earlier than March 2014 were approximately normal.

3.2 March 2014 Precipitation

Although it was not raining in Oso or in Seattle on 22 March, the day of the landslide, the spring of 2014 has been reported to be the wettest on record in Seattle. For example, a Washington Times article on April 24 reported that 487.9 mm (19.21 inches) of rain had fallen at Sea-Tac Airport since the beginning of February (<http://www.washingtontimes.com/news/2014/apr/24/record-wet-spring-for-seattle-19-inches-of-rain/#ixzz34YZIDHwZ>). It can be seen in general in the monthly actual precipitation for January, February, and March 2014 in Figures 3.1.2 and 3.1.3 that precipitation in January and February was approximately normal, whereas in most cases precipitation in March was far higher than average. March 2014 precipitation at the Everett gauge was normal, whereas it was very high at the Darrington gauge (Figure 3.1.2) and at the Marblemount, Finney Creek, and Gold Hill gauges (Figure 3.1.3).

Researchers in the Civil and Environmental Engineering Department at the University of Washington (Cao et al., 2014) analyzed the return periods of precipitation accumulation preceding March 22, 2014, based on the gauge at the Darrington Ranger Station. Precipitation accumulation periods used in their evaluation were 3, 7, 10, 14, 21, 30, 45, 60, 90, 180, and 365 days. Each evaluation period began on a different day, but ended on March 22. Cao et al. (2014) used the Generalized Extreme Value distribution to evaluate the return periods using 49 to 68 years of the Darrington record for each evaluation period. They used the gauge at Sedro-Woolley (NWS 451507, 48.52194 N. Latitude, -122.22361 W. Longitude, 66 m (217 ft) elevation) located about 50 km (30 mi) northwest of the landslide and about 64 km (40 mi) northwest of the Darrington gauge to fill in missing days in the Darrington record if the Darrington record had less than 20% of the days in the evaluation period missing from its record. If 20% or more of the days

in the evaluation period were missing from a year in the Darrington record, that year was excluded from the analysis. The results of their analysis are plotted in Figure 3.2.1.

The prominent spike in the return period curve in Figure 3.2.1 for cumulative precipitation 21 days prior to March 22, 2014, corresponds to a return period of 96.6 years, making the first three weeks of March in 2014 the wettest early to mid-March on record at the Darrington gauge. The return periods were 28.7 and 38.9 years at the Darrington gauge for 30- and 45-day periods, respectively, ending on March 22, 2014.

Daily and cumulative monthly precipitation recorded at Darrington and the three RAWS gauges during the first three months of 2014 are summarized in Figure 3.2.2. The precipitation in January and February in Figure 3.2.2 provides context for the March precipitation. Cumulative March precipitation at these gauges up to March 22 is summarized in Table 3.2.1.

Some of the variability in precipitation recorded at the gauges shown in Figure 3.2.2 and listed in Table 3.2.1 is related to elevation. Other variability probably is related to topography and the Puget Sound Convergence Zone. Precipitation in the Oso Landslide region since 1995 has been recorded by the Weather Surveillance Radar station located north of Everett in Island County, Washington, which is operated by the National Weather Service. This station is part of the NEXRAD-WSR-88D program; its NEXRAD identifier is KATX, it is located at 48.19472 N Latitude, -122.49444 W Longitude, elevation 150 m asl (<http://roc.noaa.gov/WSR88D>).

Table 3.2.1 Cumulative rainfall for March 1 to 22, 2014

Gauge Name	Darrington	Finney Creek	Gold Hill	Marblemount
Cumulative Precipitation March 1–22, 2014 (in/mm)	15.8 / 403	19.6 / 498	16.4 / 417	15.4 / 391

Descriptive information available from the National Climatic Data Center (NCDC) of the National Oceanic and Atmospheric Administration (NOAA; <http://www.ncdc.noaa.gov/>) describes radar (acronym for radio detection and ranging) as an object-detection system that uses radio waves to determine range, altitude, direction of movement, and speed of objects. The radar antenna transmits pulses of radio waves or microwaves, which bounce off objects in their path, returning a small part amount of the wave's energy (radar echo) to a receiving antenna.

The National Weather Service has operated Weather Surveillance Radar since 1957; the system since 1991 has used Doppler (WSR-88D) or NEXRAD (Next Generation Radar) technology. NEXRAD currently comprises 159 sites throughout the United States and select overseas locations, one of which (KATX – Seattle, WA) is located on Camano Island in Island County, WA, approximately 50 km (30 mi) west-southwest of the Oso Landslide. The KATX NEXRAD station began operating on February 10, 1995.

NEXRAD data consists of three meteorological base data quantities: reflectivity, mean radial velocity, and spectrum width known as Level II data; additional quantities measured include the dual-polarization base data of differential reflectivity, correlation coefficient, and differential phase. From Level II quantities, computer processing generates numerous meteorological analysis products known as Level III data, which are archived and made available for online retrieval.

NEXRAD data useful in estimating precipitation intensity and amount is radar reflectance reported in a scale specific to meteorology (decibels in the Z scale, dBZ). Reflectance is a measure of the amount of radar signal returned by moisture (raindrops or hail) in a cubic meter of atmosphere normalized to the radar signal returned by a single 1-mm-diameter raindrop in 1 cubic meter of atmosphere. To adequately sample the atmosphere, the WSR-88D employs a volume coverage pattern consisting of a series of 360 degree sweeps of the antenna at pre-determined elevation angles completed in a specified period of time. In Clear-Air Mode, the WSR-88D completes 7 azimuthal scans comprising 5 elevation angles in a period of 10 minutes. In Precipitation Mode, the WSR-88D completes 16 azimuthal scans comprising 14 elevation angles in 5 minutes.

The NEXRAD data products of value for documenting precipitation intensity are base reflectivity and composite reflectivity. Base reflectivity is a display of radar echo intensity measured in dBZ which is used to detect precipitation, evaluate storm structure, locate atmospheric boundaries, and determine hail potential. Composite reflectivity is a display of maximum reflectivity for the total volume within the elevation range of the radar. This product is used to reveal the highest reflectivities in all echoes, examine storm structure features, and determine intensity of storms. The KATX station data for the period of interest consists of four short-range base reflectivity products at elevation angles of about 0.5°, 1.5°, 2.4°, and 3.4° and one short-range composite reflectivity product. Short-range products provide data up to 124 nautical miles (230 km, 143 mi) from the antenna. The short-range composite reflectivity product was used to analyze precipitation for the GEER response to the Oso Landslide.

The Oso Landslide occurred on March 22, 2014; daily precipitation values displayed in Figure 3.2.2 show that about 4.4 inches (110 mm) of precipitation was recorded at the Darrington gauge between March 14 and 21; the values also show that about 150 mm (6 inches) of rainfall was recorded at the Finney Creek gauge during this same interval. A little over 75 mm (3 inches) of precipitation was recorded at the Gold Hill gauge, whereas a little over 100 mm (4 inches) was recorded at the Marblemount gauge.

Approximately 1800 radar scenes from the KATX station for the seven-day period from 14 to 21 March were downloaded and evaluated using GIS technology. NEXRAD Level III, short range, composite reflectivity data were selected for this analysis. A NOAA Weather and Climate Toolkit utility allows radar scenes to be combined in an animation; scenes from 14 to 17 March were

combined into an Audio Video Interleave (NEXRAD_composite2_14to17mar14_.avi) animation file.

The average precipitation intensity (rainrate) suggested by the NEXRAD guidance was used to develop an exponential regression of rainrate in inches/hr as a function of NEXRAD composite reflectivity in dBZ shown in Figure 3.2.3. An example of 14 NEXRAD radar scenes centered on the Oso Landslide from 19 March 2014, from 12:29 to 13:42 local time is shown in Figure 3.2.4. The 14 radar scenes represent a 73-minute time interval with an average of 5.2 minutes between scenes. The prediction of precipitation represented by the 14 radar scenes is 11.6 mm for an average rainfall intensity of 9.55 mm/hr (0.376 in/hr) for this particular 73-minute period. The precipitation intensity associated with the maximum radar reflectivity in any of the 14 radar scenes is 45 dBZ which corresponds to a rainrate of 24.4 mm/hr (0.96 in/hr); guidance on the radar information page of the NOAA website indicates that hail can produce higher reflectivity values than rainfall without hail. However, the handwritten notes recorded for the Darrington Ranger Station gauge indicate two days in March 2014 had rain/snow mix conditions: March 2 and March 20. Rain was recorded for March 19, with a temperature range of 40 to 48 degrees F (4.4 to 8.9 degrees C). Hail cannot be ruled out, but it appears to be unlikely for March 19.

An example of precipitation variability in the Oso Landslide area is presented in Figure 3.2.5. A storm cell on March 20, 2014, 5:06 PM local time, with radar reflectivity of 45 dBZ is over the Oso Landslide location in the center of the scene. The radar reflectivity is 15 to 20 dBZ at the Darrington Ranger Station. However, the Gold Hill, Finney Creek, and Marblemount precipitation gauge locations in Figure 3.2.5 shows radar reflectivity <5 dBZ.

The storm during the week immediately preceding the Oso Landslide (14 to 20 March 2014, in Figure 3.2.2) for which the NEXRAD radar scenes were downloaded was evaluated by collecting the reflectivity values for each of the radar scenes at a location adjacent to the head of the Oso Landslide (48.29548 North Latitude, -121.85363 West Longitude), as well as at the coordinates for Darrington, Finney Creek, Gold Hill, and Marblemount gauges (see Table 3.2.1 for coordinates). The radar reflectivity values for each of these five locations are plotted against date and time in Figure 3.2.6, as are cumulative precipitation beginning on March 14 for both continuous radar rainfall (blue line) and daily gauge precipitation (red stair-step line).

Substantial similarities can be seen in the radar reflectivity in the panels in Figure 3.2-6, but differences also are visible. A dashed green line marks the 35 dBZ radar reflectivity level, which corresponds to a rainfall of 6.1 mm/hr (0.24 in/hr). It can be seen that the radar reflectivity exceed 35 dBZ during the first half of Friday, March 14, Saturday evening, the early hours of Sunday, about midnight on Monday, from morning until mid-afternoon on Wednesday, and a brief period in the late afternoon on Thursday, March 20. The late afternoon period on Thursday, March 20, is the radar scene displayed in Figure 3.2.5. Its position on the timeline is marked with red-rimmed double-headed arrows in Figure 3.2.6.

The cumulative radar rainfall in Figure 3.2.6 is calculated from the regression of rainrate as a function of reflectivity (Figure 3.2.3) and the time between radar scenes. The gauge readings are taken as accurate; no days during this 7-day period are indicated as “missing data”. In all cases, the cumulative precipitation based on gauge data exceeds the cumulative radar rainfall. In the case of the Darrington gauge, the cumulative radar rainfall is less by 0.47 in (12 mm), whereas the cumulative radar rainfall is 80 mm (3.18 in) below the Marblemount gauge for the 7-day period.

The precipitation at the head of the Oso Landslide based on the radar rainfall is about 229 mm (9 inches) for the 7-day period from March 14 through March 20. It stands to reason that the actual precipitation is likely to exceed the calculated 229 mm (9 in) of radar rainfall. The cumulative daily precipitation plotted in Figure 3.2.6 for the period 14 to 20 March is summarized in Table 3.2.2, along with the difference between the 7-day cumulative precipitation and the 22-day cumulative precipitation (March 1 to 22). An analysis of the NEXRAD radar data for the period March 1 through March 13 was not evaluated by the GEER team; however, if the 229 mm + (9 in) of precipitation based on the radar reflectivity at the head of Oso Landslide is indicative of the precipitation amount earlier in March, then the 22-day cumulative precipitation at the Oso Landslide might have been as much as 760 mm (30 in).

Table 3.2.2. Cumulative precipitation for periods in March 2014 at nearby gauges and at the Oso Landslide. The queries (?) for cumulative precipitation at the Oso Landslide based on radar indicate an estimate that was projected from the March 14-20 radar in Figure 3.2.6 and the total for the Darrington gauge.

Gauge / Location Name	Darrington Gauge	Finney Creek Gauge	Gold Hill Gauge	Marblemount Gauge	Oso Landslide ^(a)
Cumulative Precipitation March 14-20, 2014 (in/mm)	4.62 / 117.3	6.79 / 172.5	3.66 / 93.0	5.45 / 138.4	9+ / 229+ ^(b)
Cumulative Precipitation March 1-13 & 21, 2014 (in/mm)	11.16 / 283.5	12.81 / 325.4	12.75 / 323.9	9.93 / 252.2	21+ / 533+ ^(c)
Cumulative Precipitation March 1-21, 2014 (in/mm)	15.78 / 400.8	19.60 / 497.9	16.41 / 416.9	15.38 / 390.6	~30+ / ~760+ ^(d)

^(a) The values for Oso Landslide are based on NEXRAD radar data plotted in Figure 3.2.6.

^(b) The “+” symbol indicates that the cumulative precipitation based on weather radar probably underestimates the comparable precipitation gauge value; for each of the four gauge locations, the cumulative radar estimate is less than the actual gauge value.

^(c) The values reported here are calculated from the cumulative precipitation for March 14-20 times the average ratio of the difference between gauge value and the NEXRAD value at the gauges extrapolated from the March 14-20 period.

^(d) The values reported here are the sum of the values for March 14-20 plus the calculated values for March 1-13 and March 21 in the cell above.

3.3 Flow in North Fork Stillaguamish River

The USGS has maintained a stream gauge (number 12167000) on the North Fork Stillaguamish River near Arlington for since 1928. The discharge and stage values for this station for the period after 1 October 2007 are available from the USGS website (http://waterdata.usgs.gov/wa/nwis/uv/?site_no=12167000). Online data available for Gauge 12167000 begins on 1 October 2007. The daily mean discharge in cubic feet per second (cfs) from January 2012 to late March 2014 is plotted in Figure 3.3.1. A discharge level of ~284 cms (10,000 cfs) is marked with a dashed line to emphasize that one day of discharge greater than 10,000 cfs occurred in February 2012, one day of discharge greater than 10,000 cfs occurred in January 2013, one day of discharge greater than 10,000 cfs occurred in November 2013, two days of discharge greater than 10,000 cfs occurred in January 2014, and three days of discharge greater than 10,000 cfs occurred in March 2014. The drainage basin outline and stream gauge location are labeled in Figure 3.1.1; the drainage area is 679 km² (262 mi²) above the USGS gauge. No precipitation gauges are located within the North Fork Stillaguamish River drainage basin, but the discharge at the USGS gauge near Arlington, of course, is a direct reflection of precipitation in the basin.

The daily hydrograph of the North Fork Stillaguamish River for the first three months of 2014 is plotted in Figure 3.3.2. The 10,000 cfs discharge level is marked as it is in Figure 3.3.1. The 22 March date of the Oso Landslide is highlighted in red and the effects of the landslide dam are visible in the hydrograph on March 23.

The Oso Landslide dammed the North Fork Stillaguamish River immediately upon its occurrence; the time of initial slope collapse was recorded by nearby seismic stations at 10:37 Pacific Daylight Time on March 22, 2014. USGS stream gauge on the North Fork Stillaguamish River near Arlington is 20.92 km (13 river miles) downstream from the Oso Landslide based on measurements using utilities in Google Earth Pro. The hydrograph of river stage for the period 19 to 25 March 2014, is presented in Figure 3.3.3. The 2014 landslide occurred during a period of falling river water level.

The hydrograph response to the Oso Landslide dam can be seen as a sudden drop in stage at 1:30 PM, 137 minutes after the landslide occurred. The 13-mile river distance between the landslide dam and the USGS stream gauge implies that the flow velocity was 2.0 m/s (6.6 ft/s). A small rise in river stage is visible in the hydrograph and may represent the impulse wave generated by the landslide displacing water in the river. The drop in stage amounted to about 335 mm (1.1 ft) over a 4-hr period.

The detailed times associated with changes in river stage listed in Figure 3.3.3 show that a base flow condition returned albeit at a lower stage, at about 5:30 PM on 22 March and persisted for nearly 23 hours before an abrupt rise in river stage occurred. The abrupt rise in stage moderated at 6:00 PM on 23 March. Flow across the landslide appears to have been essentially recovered by

9:30 AM on 24 March. The USGS reported that the drop in river stage amounted to a reduction in discharge of about 34 cms (1200 cfs) (online report at http://www.usgs.gov/blogs/features/usgs_top_story/landslide-in-washington-state/). A stream gauge downstream from Arlington on the Stillaguamish River (USGS 12170300) in the range of tidal influence also recorded the effect of the Oso Landslide dam (Figure 3.3.4).

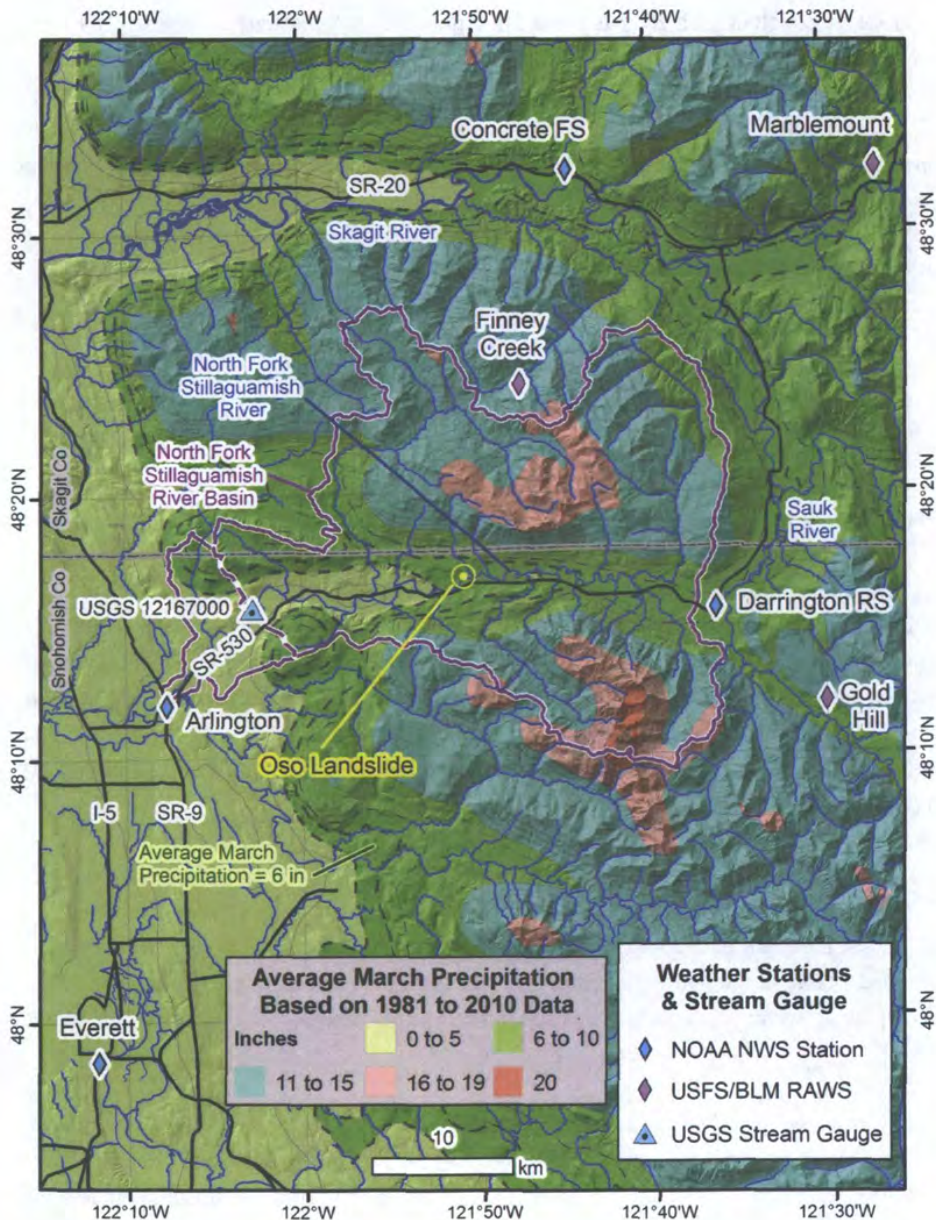


Figure 3.1.1 Map of the Oso Landslide region showing locations of selected weather stations and a stream gauge. Seven weather stations and a stream gauge with the drainage basin outline of North Fork Stillaguamish River; Base map is NWS GIS data of average March precipitation based on the 30-year interval between 1981 and 2010 (GIS file for State of Washington obtained from <http://datagateway.nrcs.usda.gov/>).

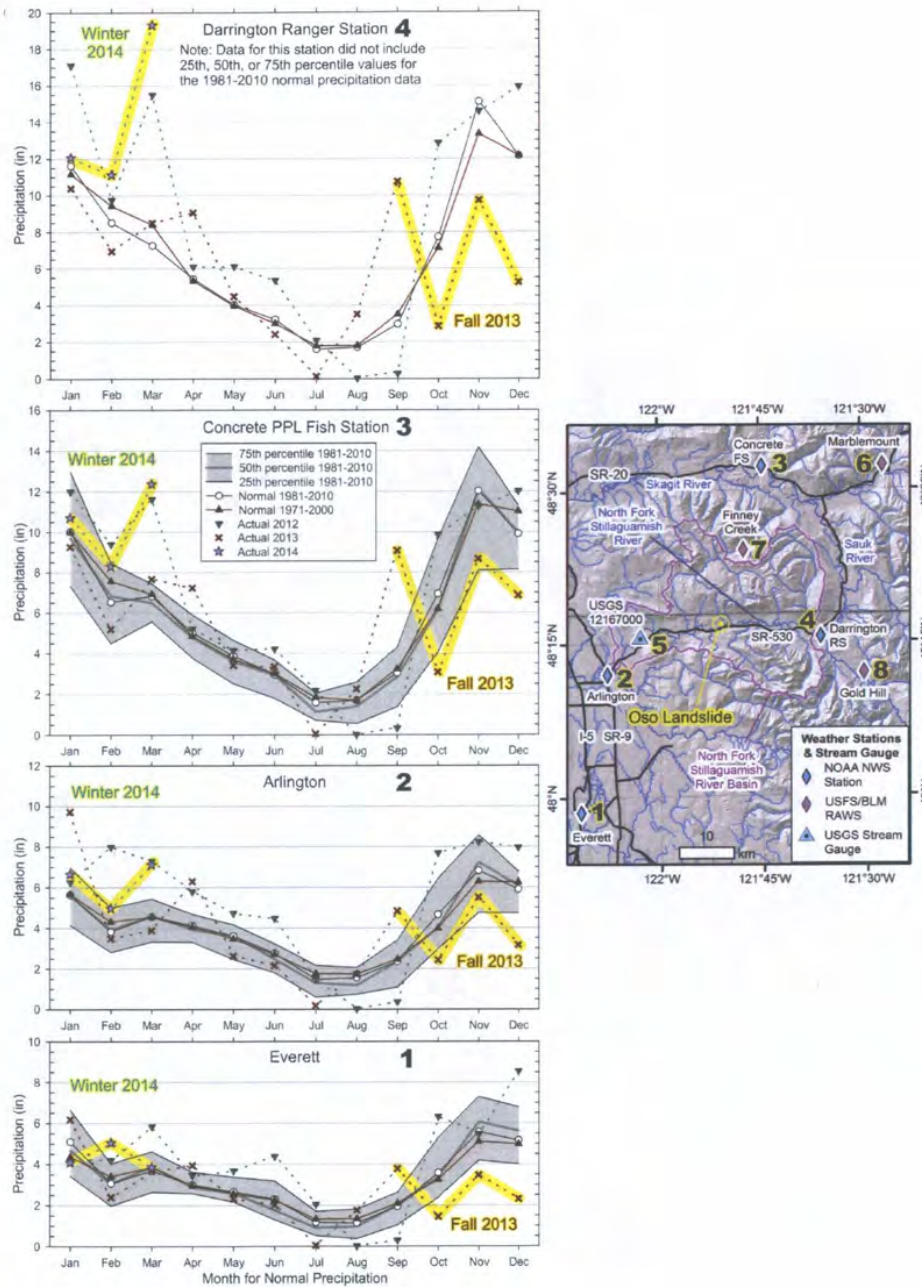


Figure 3.1.2 Monthly average precipitation data for four NWS cooperative weather stations and monthly precipitation values for January 2012 to March 2014. Data obtained from the Western Regional Climate Center at <http://www.wrcc.dri.edu/summary/Climsmwa.html>.

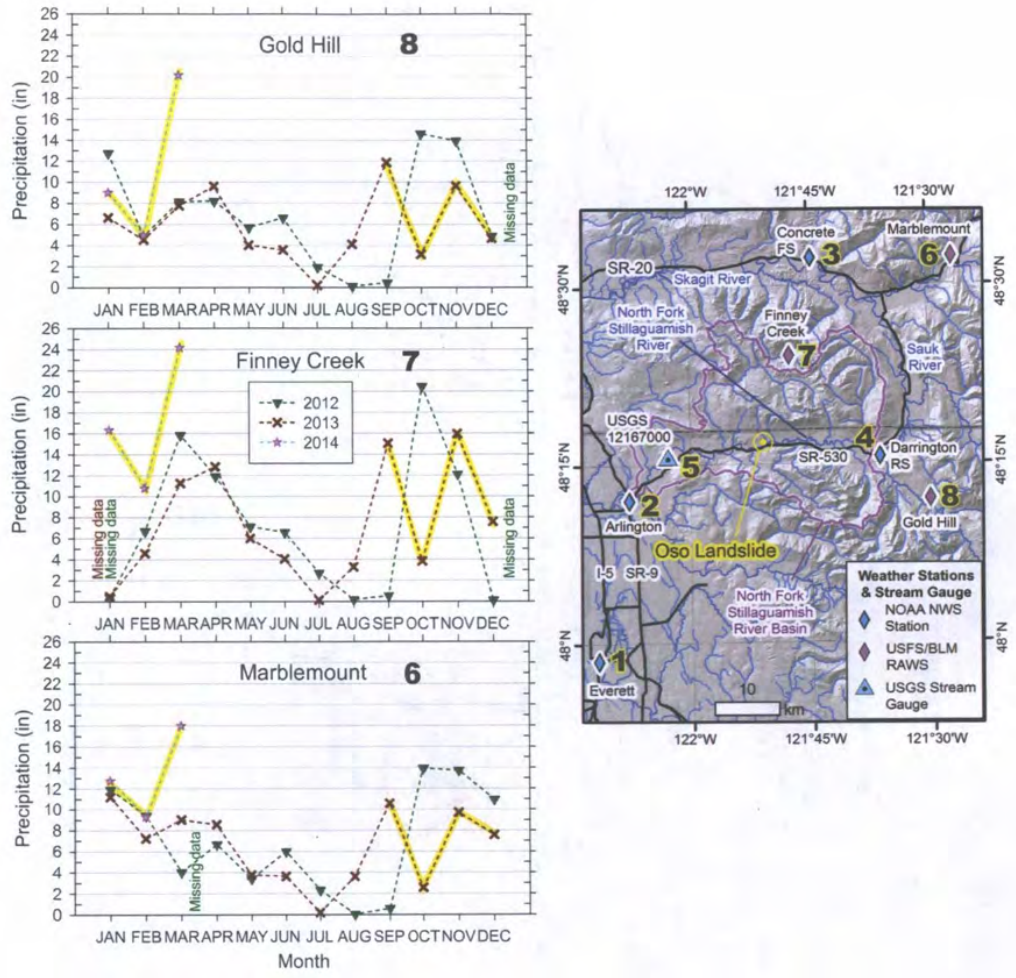


Figure 3.1.3 Monthly precipitation values for three RAWS gauges for January 2012 to March 2014. Data obtained from the Western Regional Climate Center at <http://www.raws.dri.edu/wraws/waF.html>.

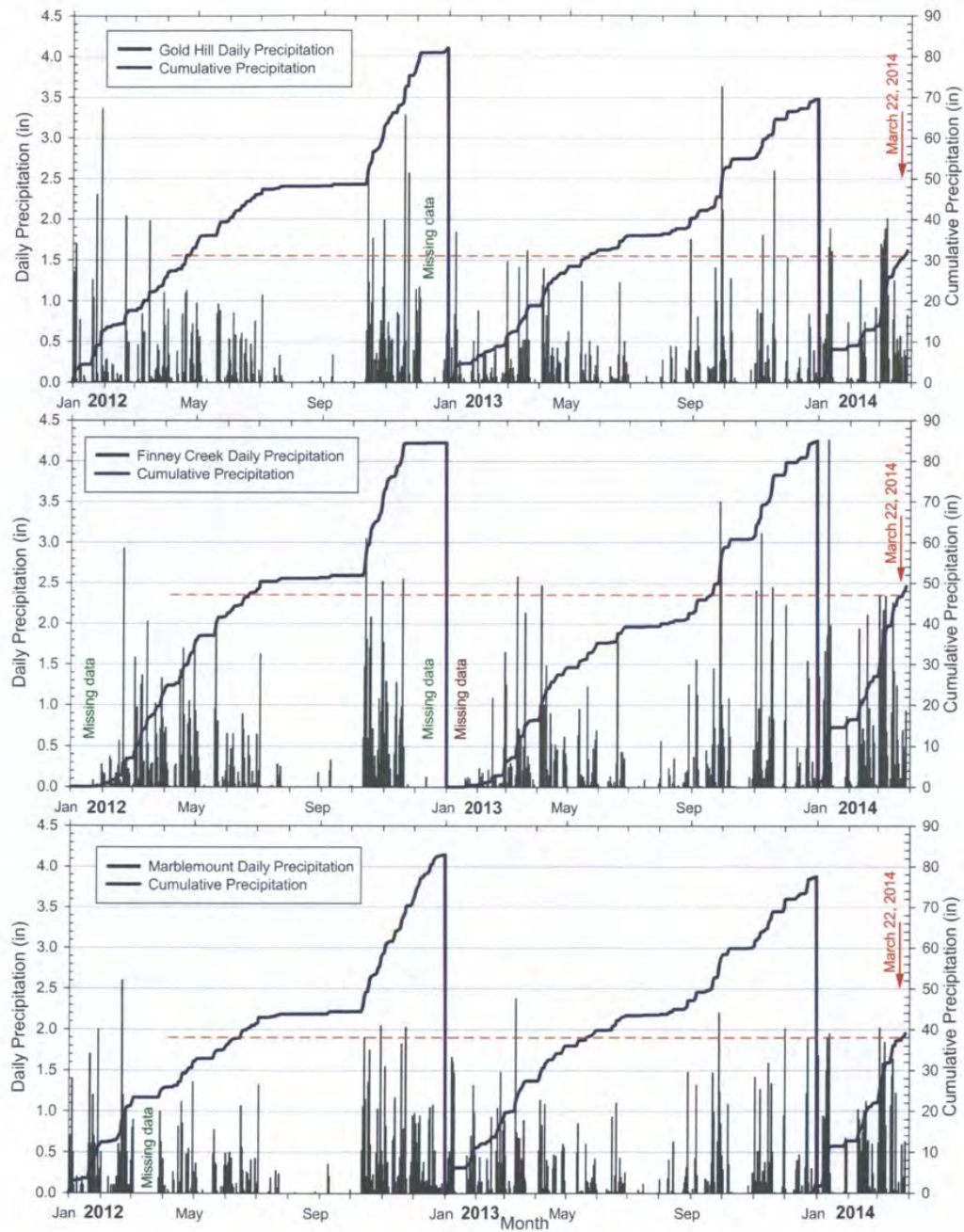


Figure 3.1.4 Daily and cumulative annual precipitation at three RAWS gauges in the vicinity of the Oso Landslide for 2012, 2013, and the winter months of 2014.

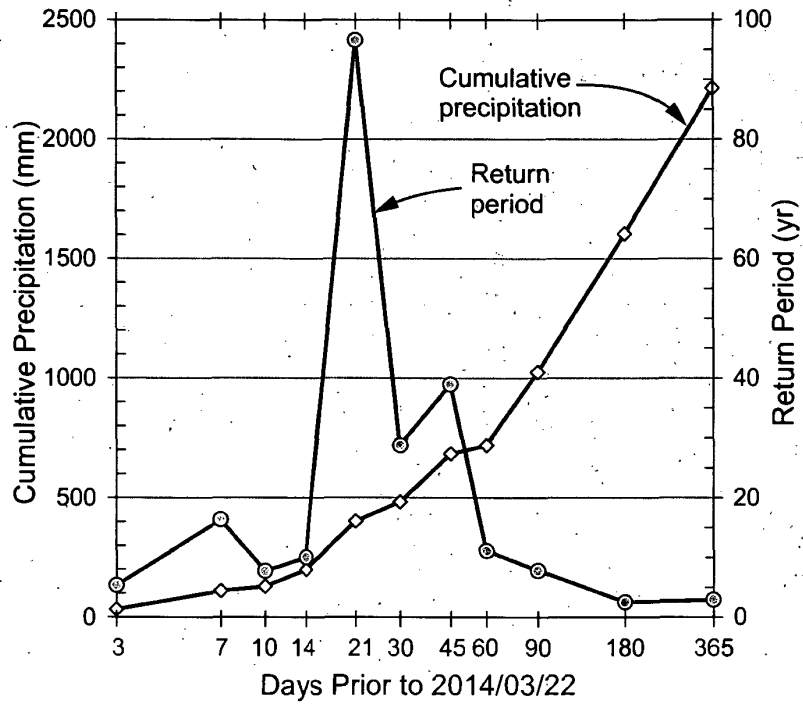


Figure 3.2.1 Cumulative precipitation preceding March 22, 2014, and associated return period at the Darrington Ranger Station gauge. Plotted from values presented in Cao et al. (2014).

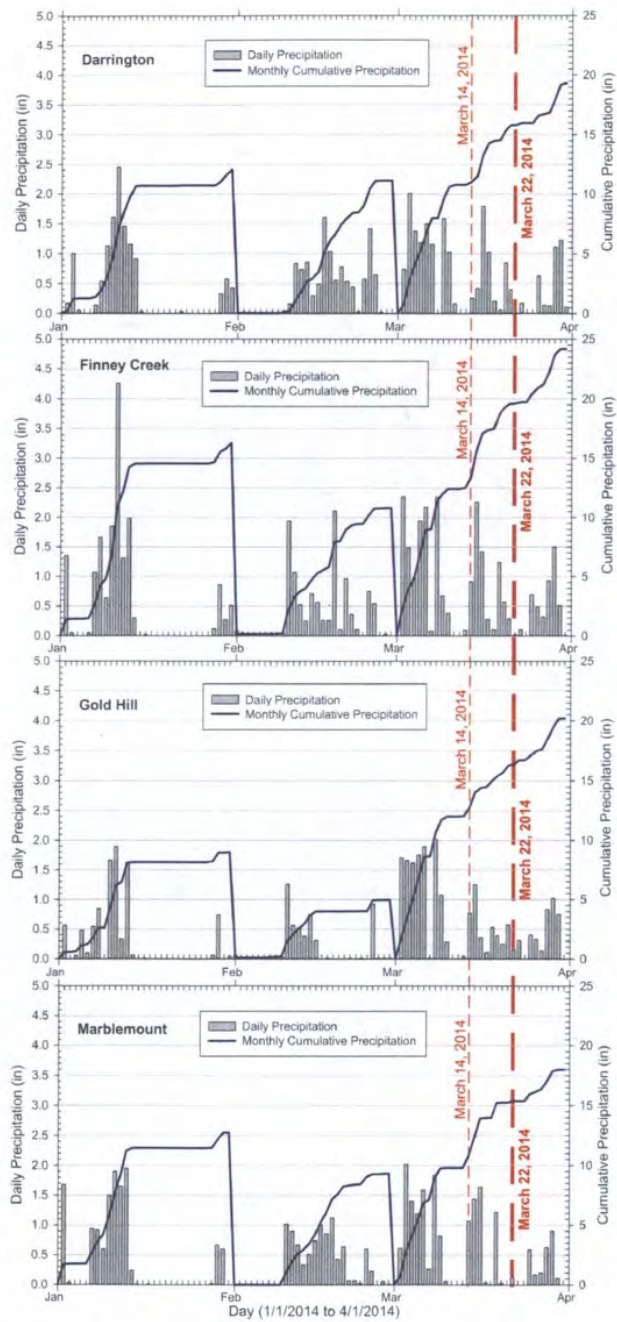


Figure 3.2.2 Daily and cumulative monthly precipitation recorded at Darrington and the three RAWS gauges during the first three months of 2014.

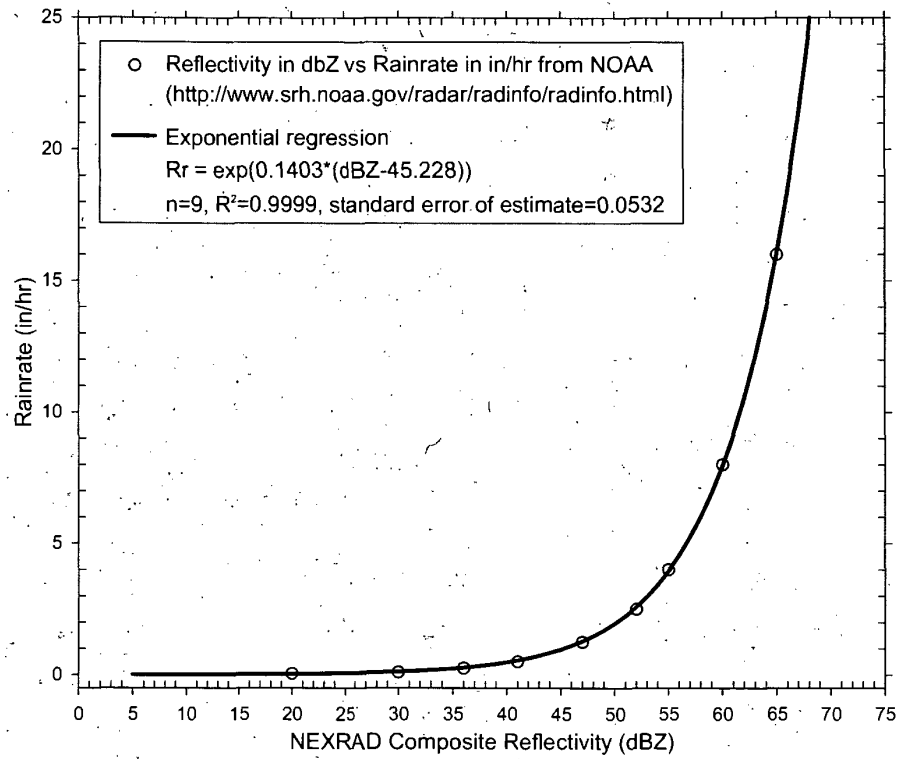


Figure 3.2.3 Exponential regression predicting rainrate (Rr) as a function of composite Doppler radar reflectivity (dBZ).

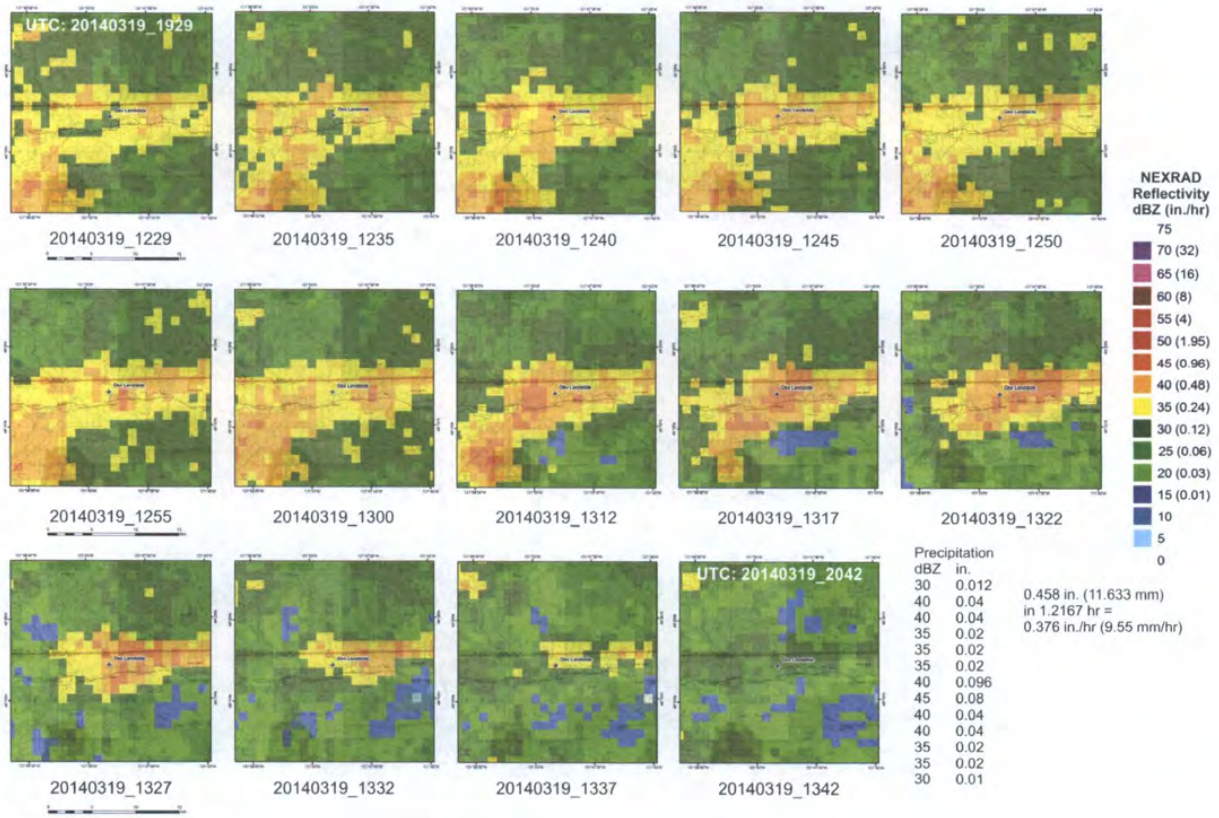


Figure 3.2.4 NEXRAD Reflectivity at the Oso Landslide on 19 March 2014 from 12:29 to 13:42 PDT. Reflectivity is related to precipitation intensity; therefore, the images represent a series of precipitation intensity maps correlated to reflectivity in dBZ.

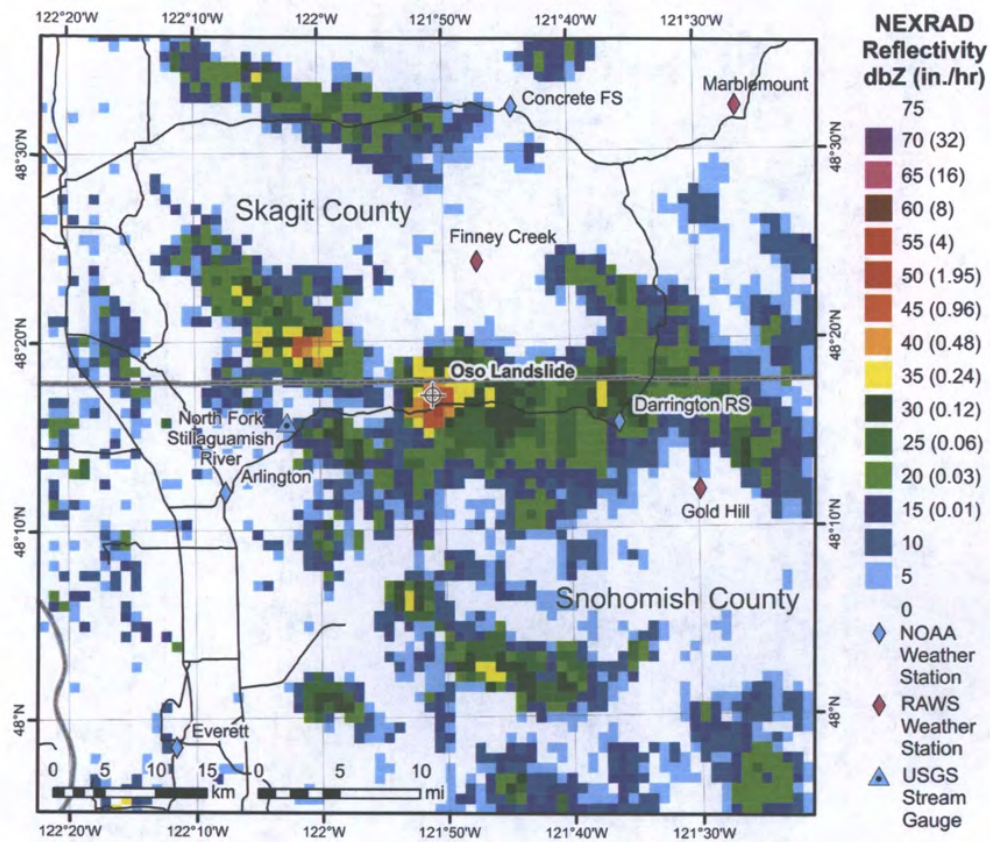


Figure 3.2.5 Example of NEXRAD composite reflectivity showing highly variable conditions. Scene is 20140321_0006 UTC = March 20, 2014 5:06 PM Pacific Daylight Time.

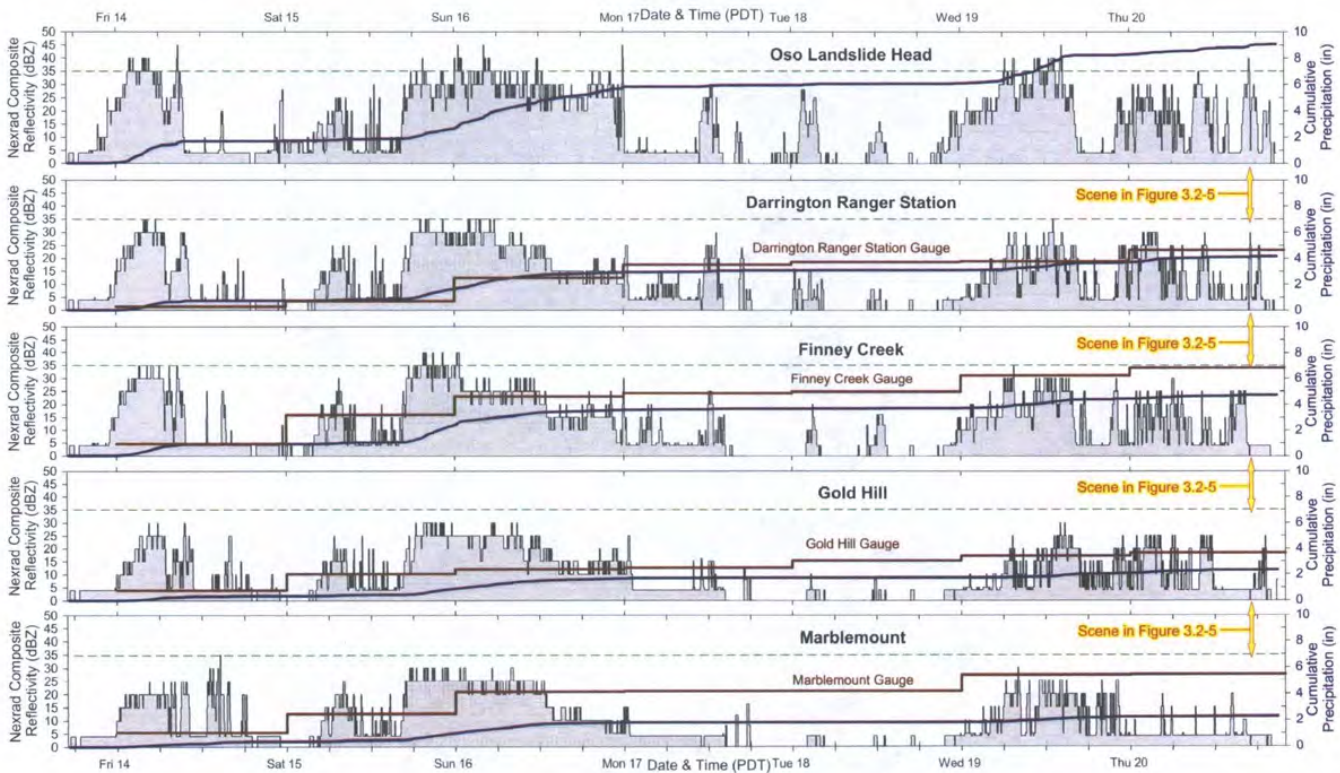


Figure 3.2.6 Composite precipitation diagram showing radar rainfall and gauge precipitation for the Oso Landslide and four gauge locations

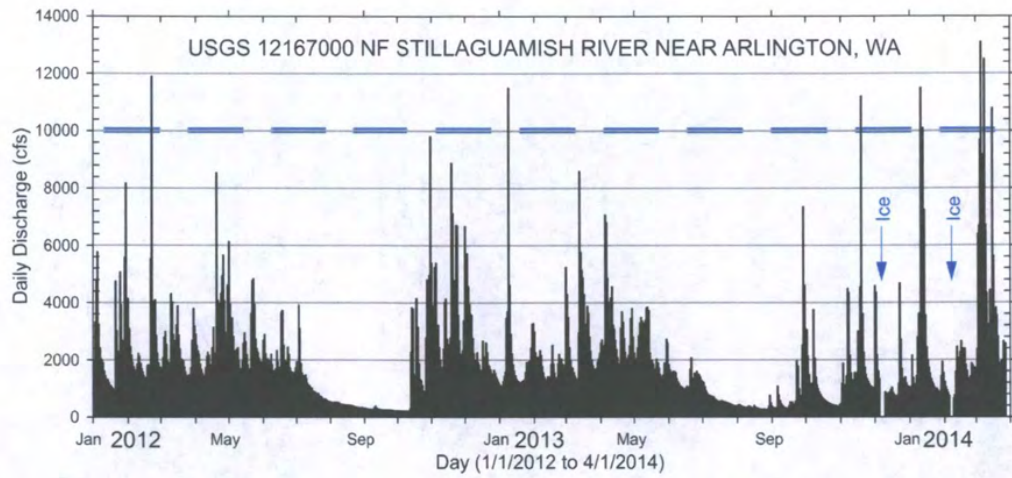


Figure 3.3.1 Discharge hydrograph of North Fork Stillaguamish River near Arlington, WA, January 2012 through March 2014

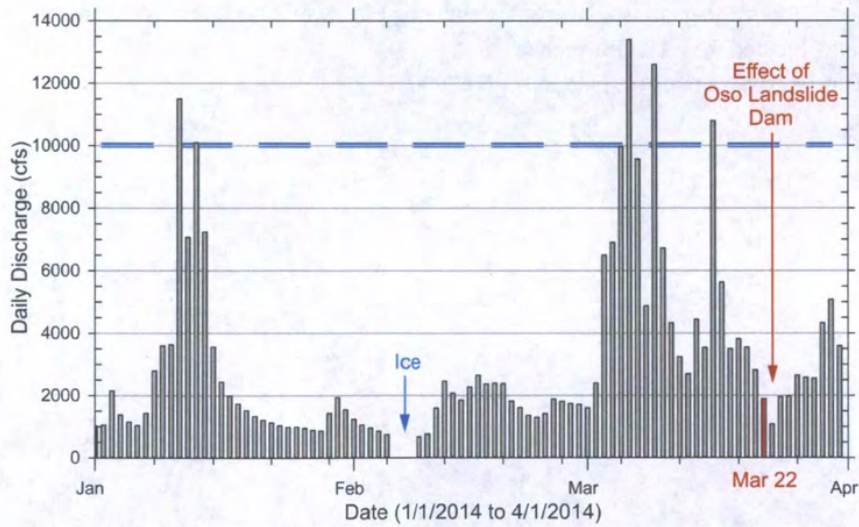


Figure 3.3.2 Hydrograph of North Fork Stillaguamish River, January through March 2014.

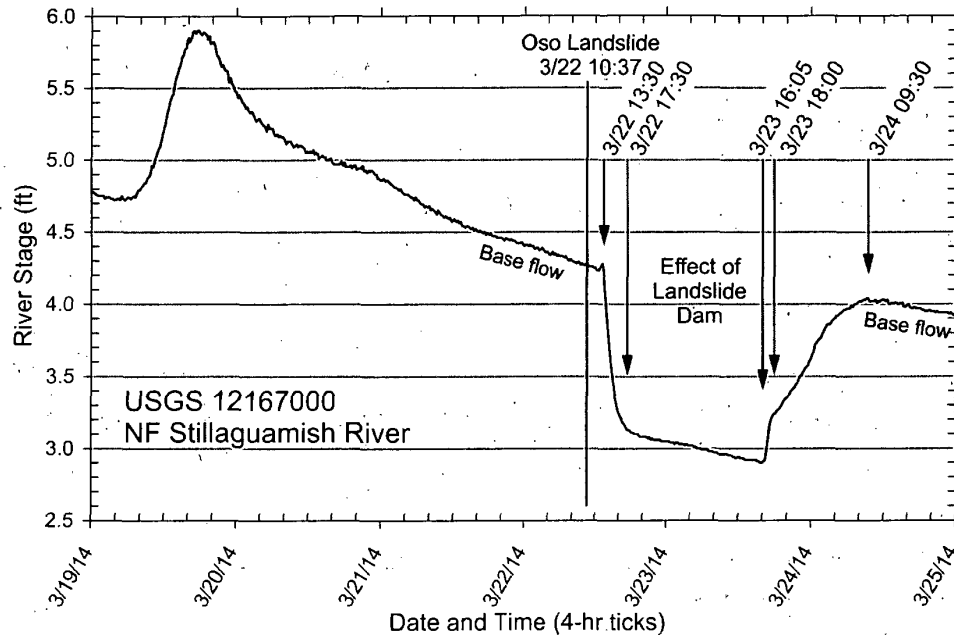


Figure 3.3.3 North Fork Stillaguamish River stage showing effects of Oso Landslide dam.
 Plotted from data obtained from USGS website
http://waterdata.usgs.gov/wa/nwis/uv/?site_no=12167000

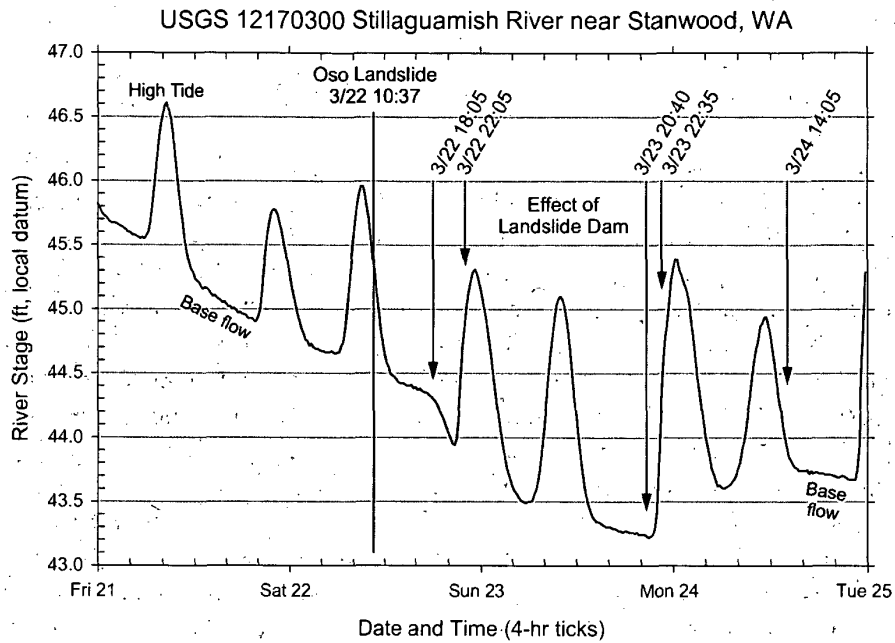


Figure 3.3.4 Stillaguamish River stage showing effects of Oso Landslide dam and tidal influence from Puget Sound. Plotted from data obtained from USGS website http://waterdata.usgs.gov/wa/nwis/uv/?site_no=12170300.

4. OSO LANDSLIDE BACKGROUND

4.1 History of Landsliding along the North Fork Stillaguamish River Valley

Lidar-derived shaded relief images of the North Fork Stillaguamish River valley (Figure 4.1.1 from data acquired in 2003) show striking evidence of multiple generations of large landslides in the vicinity of the 2014 Oso Landslide. Haugerud (2014) used the 2013 lidar data to map a total of at least 15 large landslides in four relative age classes in the immediate vicinity of the Oso Landslide (Figure 4.1.2), all readily apparent in the scalloped margin of the Whitman Bench and the opposite valley wall (i.e., on the southern side of the valley). The four relative age classes of landslides that Haugerud identified post-date deposition of the recessional outwash to form the Whitman Bench circa 14,000-16,000 years ago. His mapping includes a large slide immediately to the west of the Oso Landslide that ran out across most of if not the entire valley bottom, leaving an appearance much like the 2014 Oso Landslide (Figure 4.1.2). It should be noted that this large landslide was mapped by Dragovitch et al. (2003) (Figure 2.2.1); however, their focus was broader than landslide deposits and their base map was a simple topographic contour map. Furthermore, the Dragovitch et al. map was published in 2003, which was the year of the first lidar survey of the valley. Haugerud (2014) classified the large slide as age class B; only currently active slides (class A in Figure 4.1.2) are younger. Indeed, virtually the whole valley bottom in the vicinity of the Oso Landslide is either old landslide deposits or areas where such deposits would have been reworked in the Holocene by active channel migration and floodplain-forming alluvium deposition. Rough recurrence frequencies of 1,000 and 3,750 years for large landslides in this portion of the valley can be estimated, respectively, from at least 15 large landslides in about 15,000 years or the 4 generations of large landslides in the same time frame. It is not known how many prior landslides that occurred during valley incision and widening are no longer preserved in the topography; a history of additional landslides in this portion of the valley would reduce the recurrence interval to the order of hundreds of years.

While most of the ancient landslides mapped by Haugerud (2014) have rounded, subdued morphology suggestive of inactivity and recent stability, Thorsen (1989) noted the high potential for reactivation of old landslides and the initiation of new slope failures in glacial material in western Washington. Thorsen (1989, p. 76) noted how most such slides begin as slumps due to elevated groundwater levels and pointed out how the *"collapsing walls of headward sapping... Pleistocene terraces is largely removed as repeated mudflows."* He pointed to an example of one such failure (in Deer Creek near the town of Oso) that introduced more than one million cubic yards (>765,000 cubic meters) of silt and sand into the Stillaguamish River system (Thorsen, 1989).

The 2003 lidar topography (Figure 4.1.3) for the margin of the Whitman bench shows the steep headscarp of an ancient landslide defining the southeast margin of the Whitman Bench, upslope of the then active (2003) headscarp position of the Oso (Hazel) landslide. Likewise, the modern topography of the Headache Creek basin to the immediate northeast of the Oso Landslide reflects

a large ancient slump to the east, towards Rollins Creek. Both are mapped by Haugergud (2014) as age class D, his oldest age class. The active headscarp of the Oso Landslide and disrupted terrain lower on the slope are also apparent on the 2003 lidar image, which shows the river eroding into the toe of the western edge of the slide mass.

The 2013 lidar topography (Figure 4.1.4) shows the river displaced several hundred feet to the southeast relative to its 2003 position (Figure 4.1.3), with a more pronounced headscarp and net deposition due to a 2006 reactivation of the Hazel Landslide. Differencing the elevations for the 2003 and 2013 lidar data sets (Figure 4.1.5) shows a net decrease in elevation of up to 30 m (100 ft) below the headscarp and up to 17 m (56 ft) of deposition in the toe of the 2006 slide. Note in particular in Figure 4.1.5 the decrease in elevation along the western margin of the 2006 slide which removed support from the upper half of the ancient slide mass between the 2006 landslide and the Whitman Bench (apparent in the darker red colors in Figure 4.1.5). In addition, note the lowering of the eastern margin of the active landslide relative to the elevation of the neighboring drainage basin of Headache Creek to the northeast of the 2006 Hazel Landslide.

The 2014 lidar data set shows the morphology of the most recent slide (Figure 4.1.6). Differencing the elevations for the 2013 and 2014 lidar data sets (Figure 4.1.7) reveals up to 88 m (288 ft) of elevation loss below the headscarp and up to 23 m (74 ft) of local elevation gain on depositional mounds on the valley bottom as a result of the 2014 Oso Landslide. Figure 4.1.8 is a cross-section illustrating the differences between the elevations for the 2003 and 2013 lidar data sets and the elevations for the 2013 and 2014 lidar data sets.

4.2 History of Slope Stability at the Oso (Hazel) Landslide Site

Episodes of prior movement of the Oso (Hazel) slide have been described in a number of studies dating back to the 1950s (Shannon and Associates, 1952; Thorsen, 1969; Benda et al., 1988; Miller and Sias, 1997; 1998). The observed historic activity appears to be episodic with the headscarp advancing headward between 1952 and 2006, but with the main slide mass constrained to approximately the same portion of the slope where the 2006 landslide failed (see Figure 4.2.1 for historic Oso/Hazel Landslide disturbances and scarps from 1952 to 2013).

Miller and Sias (1997; 1998) used aerial photographs and prior reports (Shannon and Associates, 1952; Thorsen, 1969; Benda et al, 1988) to investigate the history of prior sliding at the site. Miller and Sias (1997) reported that aerial photographs show that the Oso (Hazel) Landslide was active in 1937, and noted that Benda et al. (1988) estimated that the slide encompassed about 10 acres by 1942.

Shannon and Associates (1952) conducted the first direct study of the landslide in a report to the Washington Department of Game. In addition to subsurface borings and testing, the report by Shannon and Associates (1952) investigating the cause of a 1949 reactivation of the landslide, included an aerial oblique photograph (Figure 2.4.2B) depicting areas of significant timber

harvesting to the northeast as well as within the slide area. An area north of the slide is labeled as being logged between September and December 1951 as noted on one of the report figures (included in Figure 2.4.2A). South of the river in the 1949 aerial oblique photograph (Figure 2.4.2B) appears to be a floodplain with gravel bars along the river (white strips). It should be noted that during GEER reconnaissance we observed evidence of the gravel bars below the glacial lacustrine deposits along the Stillaguamish River. Shannon (1952) described the failed area, which corresponds to the same area that subsequently failed again in 2006 and 2014. The total length along the toe or river edge was estimated at 2,600 ft (790 m). The main scarp was located approximately 1,000 ft (305 m) from the river. The scarp height was estimated to be about 70 ft (21 m). The portion of the slide adjacent to the river is described as eroded clay without vegetation. Within the slide mass, Shannon and Associates (1952) reported "large masses or blocks of natural ground which have moved down the hill but still maintain their cover of hardwoods, brush and some conifers." They also noted that a mudflow from the slide partially blocked the river in December 1951. Shannon and Associates (1952) also described the presence and source of water at the site of the 1949 landslide. Two creeks are located within the slide mass and flow at about 25 gpm (95 Lpm). These creeks are in part fed by increased infiltration from exposed pervious soils north of the slide. Weathering of the exposed clay also creates fissures that provide paths for water to infiltrate deeper into the failed mass. Once wet, the medium to hard clay softened considerably and resulted in mudflows. In the Appendix of the Shannon and Associates (1952) report is an assessment from Professor Howard Coombs (Professor of Geology at the University of Washington) stating that the slide is due to "piecemeal slumping – one block at a time." He suggests that the slip planes are shallow and localized with each block. The Shannon report however depicts relatively shallow failure planes parallel to the slopes and all intersecting the river.

Aerial photographs from 1965 show substantial areas of bare earth indicative of recent activity within the slide (Miller and Sias, 1997; 1998). Department of Natural Resources geologist Gerald W. Thorsen (1969) described further landslide activity in January 1967 as having moved the river several hundred feet to the south, with the slide extending 456 m (1500 ft) from crown to toe, from near river level at about 76 m (250 ft) elevation to more than 122 m (400 ft) in elevation. Thorsen (1969) noted that aerial photographs from 1932 showed the river actively cutting into a clay bank at the toe of the slope, and attributed to Shannon and Associates (1952) the observation that river turbidity had increased greatly since the early 1930s. He described that increased siltation in the river had prompted calls from sportsmen's groups for the Washington Department of Fish and Game to "do something." Thorsen (1969) noted that a rock revetment and log cribbing constructed in 1962 along the right bank of the river (along the outside of the roughly right angle meander bend) was buried by the 1967 landslide.

Thorsen (1969) further reported that the 1967 landslide involved a failure plane (slip surface) above the river level, with movement involving both rotational slumps and mudflows. Thorsen described the bulk of the January 1967 landslide as a mudflow that carried intact blocks of the

overlying clayey sand. He concluded that *"this slide activity is mainly the result of large springs feeding into the head and upper slip plane area"* (Thorsen, 1969, p. 6).

In describing his visit to the landslide site in 1969, two years after the renewed sliding in 1967, Thorsen noted the quicksand-like nature of portions of the slide deposit.

"Travel across the slide surface is extremely treacherous because of hidden "pockets" of saturated material that will not support a man's weight" (Thorsen, 1969, p. 2).

Thorsen (1969) noted that the slope uphill of the 1967 headscarp appeared to be part of a series of larger, ancient slides. Based on examination of topographic maps and aerial photographs, Thorsen (1969) cautioned that the presence of large landslides on both sides of the valley carried high risk for downslope infrastructure.

"The scars of these ancient slide scarps still show as semicircular bites out of the 800-foot elevation terrace remnants left on both sides of the river valley. The debris lobes from these slides have been greatly modified or, in place[s], almost completely removed by stream erosion. ... Air photos indicate no activity among these ancient slides other than the partial reactivation of the one, the subject of this report. Nevertheless, this slide has shown that major construction below any of these old scarps should be done with extreme caution." (Thorsen, 1969, p. 5).

Miller and Sias (1997) note that the landslide was largely revegetated by 1978. Miller and Sias (1997, 1998) also described a riverside slump from the toe of the slope subsequently occurred on Thanksgiving Day in 1988, after the river had once again eroded into the toe of the landslide. Miller and Sias (1997) describe 1991 aerial photographs that show reactivated sliding of large blocks in 1988 pushed the river channel to the south. Miller and Sias (1997) also note field observations in 1995 indicating that a rock revetment constructed in 1962 had been almost completely exhumed by river erosion, and that further sliding over the winter of 1996 involved a series of "headward-eating slumps" (p. 1.7).

Miller and Sias (1998) summarized the history of landslide activity at the site as involving multiple blocks reflecting repeated failure.

"Headward growth typically occurs via a series of rotational and translational slumps that expose steep head scarps in the outwash sands and have slip surfaces extending into the underlying lacustrine deposits. These slumps typically evolve downslope into mud flows." (Miller and Sias, 1998, p. 925).

Georeferencing and compiling the various versions of mapped positions of the active headscarp into a single map reveals evidence of minor episodic headward growth (Figure 4.2.1), until the slide expanded greatly in 2006 and again, this time catastrophically, in 2014.

In summary, the GEER reconnaissance investigation has found several dates of renewed activity since the 1930s and, by implication, relatively little activity between then and the ancient failure of the slope. Actual dates, and the sizes and type of failures have not been compiled but they include slumps, transverse sliding of blocks where the forest largely remained intact, and debris flows. The size of the slide area enlarged relatively slowly until a large increase in 2006 and a catastrophic increase in 2014.

4.3 Prior Slope Stability Analyses

Miller and Sias (1998) used a 1:4800-scale topographic map (based on 1978 aerial photography) of the vicinity of the Oso (Hazel) Landslide with the USGS groundwater model MODFE, and Bishop's simplified method of slides (Bishop, 1955) to estimate potential effects of river incision and forestry practices on the stability of the Oso (Hazel) landslide. They used estimates of the hydraulic conductivity and specific yield of different geologic units in the slide, and the estimated elevation of stratigraphic contacts to generate predicted groundwater levels that were then input into the slope stability model.

Miller and Sias (1998) estimated that the forest evapotranspiration at the landslide site accounted for between 45 and 75% of annual rainfall. In an earlier report they estimated the time-averaged increase in groundwater recharge to the landslide from clearcut logging was between 17% and 51% of the mean annual precipitation, with the value likely near the upper end of this range (Miller and Sias, 1997). They also estimated that annual evapotranspiration accounted for just 20% of annual rainfall in recent clearcuts, due to a nearly complete shutdown of winter evapotranspiration (Miller and Sias, 1998). After estimating the annual interception loss to the forest at 305 to 550 mm (12 to 22 inches), they estimated a minimum change in recharge due to complete clearcutting (the maximum amount of clear cutting possible) of the groundwater recharge zone for the Oso (Hazel) Landslide as between 280 mm/yr and 890 mm/yr (11 in/yr and 35 in/yr) (Miller and Sias, 1998).

Miller and Sias (1998) reported that the predicted effect on slope stability (as expressed through the calculated factor of safety) was spatially quite variable, ranging from no response to up to a 30% decrease in stability for some locations in response to timber harvest in the upslope groundwater recharge zone. Bank erosion, such as that expected to occur along the outer bank of the river bend at the toe of the landslide, lowered the calculated factor of safety for locations near the toe by up to 75%. Miller and Sias (1998) also reported that their analysis found that the rainfall in the prior year significantly influenced the calculated factor of safety, as did the annual rainfall totals averaged over the previous four years.

4.4 Subsurface Characterization

The slide mass has been characterized by only one subsurface investigation that we are aware of, and that is the report by Shannon (1952). They advanced three borings just behind the 1949 slide scarp and within the ancient slide mass and one near the drainage divide with Headache Creek that is likely not part of the ancient slide mass that mobilized into the Oso Landslide, but probably was part of a ancient slide mass in the Headache Creek drainage basin. Logs of the borings from the Shannon (1952) report are presented in Figure 4.4.1. The boring near the divide (B-1) shows gray fine sand, silt and clay from 6 to 221 feet (1.8 to 67 m) depth, where the hole was terminated. This is consistent with the in-place section of glaciolacustrine deposit. The other three borings (B-2, B-3 and B-4) show variable stratigraphy despite being located quite close to each other. They identify strata of various grain sizes and characteristics, but a generally oxidized sandy material to a depth that varies from approximately 18 to 49 feet (5.5 to 15 m). This material is underlain by gray strata of silt and medium to hard clay with some sand and gravel. It also appears that a loose layer of oxidized brown sand was encountered beneath 74 feet (22.5 m) of medium to hard blue (gray) clay in boring B-4; the need for casing to control caving of this layer was the reason the hole was terminated at 221 ft (67 m) depth. The logs also indicate that drill water was lost at several depths ranging from 18 to 71 feet (5.5 to 22 m) in both sandy and clayey strata. Water loss is indicated in the boring logs with an asterisk symbol at the appropriate depth; note that no drill water was reported lost in the log of boring B-1 to a depth of 221 feet (67 m) [Figure 4.4.1].

Four samples of lacustrine clays taken from these borings had natural water contents ranging from 27% to 31%, plastic limits of 23% to 27%, liquid limits of 44% to 56%, and shear strength of about 1 to 2 tons per square foot (100 to 200 kPa) (Thorsen, 1969). Other than the surface expressions now visible, the report with boring logs and test results from 1952 are the best descriptions available of what mobilized as the flow slide on March 22, 2014.

At a Seattle location, Palladino and Peck (1972) reported large differences in peak and residual strength values for glacially over-consolidated clays similar to those at the Oso Landslide site, with peak strength characterized by a cohesion of 62 kPa (9 psi) and a friction angle of 35°, and residual strength characterized by a cohesion of zero and a friction angle of 14° to 18° for disturbed clays.

4.5 Land-Use and Risk

Risk is the possibility of suffering loss, and it is represented by the consequence and probability of a loss¹. This section summarizes available information about the consequences and

¹ Risk is mathematically defined as the expected value of a loss, which is the sum of the product of each possible consequence multiplied by the probability of the consequence. In terms of natural landslides, the probability of a particular landslide (i.e., landslide involving a given volume of material and runout) occurring is typically referred to as the hazard.

probabilities of landslides in this valley of the North Fork Stillaguamish River. It concludes with a discussion of means that were in place to manage landslide risk at the time of the March 2014 event.

People, Property, Resources and Infrastructure at Risk

The portion of the valley directly below the slope and affected by the 2014 event contained 108 lots zoned for Single Family Residences. Some form of structure was located on 49 of the lots; 25 were occupied year round and 10 were occupied part time as vacation homes. The Steelhead Haven Plat was recorded in 1960. About one-half of the homes were built after 1996. After the 2006 landslide, five new homes were built in Steelhead Haven and two were built outside of it but within the area affected by the 2014 landslide.

The closest home to the slope before the 2014 event was approximately 120 m (400 feet) from the toe of the slope; this home was nearly twice as far from the toe of the slope before the 2006 event moved the toe and shifted the river. This information is summarized on a map produced by the Snohomish County Planning and Development Division following the 2014 event (Figure 4.5.1). Additional occupied properties are located both upstream and downstream from the Oso Landslide area that could be impacted by flooding induced by a landslide dam.

The North Fork Stillaguamish River serves as habitat and spawning grounds for Chinook salmon, a species listed under the Endangered Species Act. The river below and downstream from the Oso Landslide slope is within the "Usual and Accustomed" fishing area for the Stillaguamish Tribe of Indians. The Tribe owns the right to take up to 50 percent of the harvestable fish resources, and they manage, protect and conserve this resource.

The valley wall up to the Whitman Bench (i.e., the slope) is mostly private property and was not developed. This land had previously been used for forestry up until the late 1980's. The valley contains a two-lane highway, State Route (SR) 530, which serves as the primary route for transportation between Arlington and Darrington. High-tension power lines operated by Seattle City Light run approximately parallel to SR 530 on the south side of the valley.

Probabilities of Landslides

We are not aware of any formal assessments for the probability of a landslide in this valley. However, multiple studies identified the potential for a "catastrophic" failure affecting human safety and property. A 2001 report by GeoEngineers, which made use of earlier geotechnical and geological studies by Shannon and Associates (1952) and Miller (1999), expressed the status quo conditions as follows (page 9):

- "Large, persistent, deep-seated landslides don't just go away
- Current slide activity has a detrimental effect on fisheries habitat and productivity

- Stillaguamish Summer/Fall Chinook have been listed under Endangered Species Act
- Catastrophic failure potential places human lives and properties at risk.”

The Miller (1999) study estimated the expected run-out distance to be less than 275 m (900 feet), based on the assumption of a landslide volume comparable to prior landslides at the site. The run-out distances from the three major landslides preceding the 2014 event were all 100 to 200 meters (325 to 650 feet). We are not aware of any predictions that the debris from a landslide in this valley could run-out thousands of feet across the valley floor like it did in the 2014 event.

Risk Management Means

Risk management involves balancing benefits of reducing risk against the costs required to reduce it. Risk can be reduced by reducing either the probability of an event occurring (say by buttressing or draining surface water and groundwater from the slope) or by reducing the severity of consequences given that an event occurs (say by removing people or property from harm's way).

Over the past 60 years, a variety of means were considered to manage the risk associated with this slope. A 2001 study by GeoEngineers for the Stillaguamish Tribe of Indians identified alternatives for remediating the landslide that ranged from stabilizing the river bank to minimize erosion to moving the river channel and removing development by buying out properties.

At the time of the 2014 event, the two means that had been employed to manage risk from a landslide were land-use restrictions implemented by Snohomish County and the Washington Department of Natural Resources and river bank stabilization implemented by the Stillaguamish Tribe of Indians.

Land-Use Restrictions

Snohomish County is responsible for managing development in this valley. If a property is within a “Landslide Hazard Area” as per the definition established in the Snohomish County Unified Development Code², then the following restrictions on land use apply:

² “Landslide Hazard Areas” are defined as areas “potentially subject to mass earth movement based on a combination of geologic, topographic, and hydrologic factors, with a vertical height of 10 feet or more. These include the following: (1) areas of historic landslides as evidenced by landslide deposits, avalanche tracks, and areas susceptible to basal undercutting by streams, river or waves; (2) areas with slopes steeper than 33% which intersect geologic contacts with a relatively permeable sediment overlying a relatively impermeable sediment or bedrock, and which contain springs or ground water seeps; (3) areas located in a canyon or an active alluvial fan, susceptible to inundation by debris flows or catastrophic flooding” (Chapter 30.91L.040). This setback distance is greater than that required by the International Building Code.

- Development activities are not permitted in landslide hazard areas or their required setbacks (unless there is no alternate location on the subject property).
- Structures shall be setback from landslide hazard areas, such that:
 - o The minimum setback at the top of the slope is the maximum of (i) the slope height divided by three and (ii) 50 feet³ (15 m).
 - o The minimum setback at the toe of the slope is the maximum of (i) the slope height divided by two and (ii) 50 feet³ (15 m).
 - o Exceptions can be made if there is no alternative placement for the structure on the property, or if a geotechnical study proves that the alternative setback provides protection equal to that provided by the standard setbacks.
- Vegetation must not be removed (unless recommended otherwise in a site-specific geotechnical study)
- The factor of safety for landslides must exceed 1.5 for static conditions or 1.1 for dynamic conditions.
- Tiered piles or piers should be used for structural foundations.
- Retaining walls that allow for the maintenance of natural slopes shall be used instead of artificial slopes.
- If there is no alternative, utilities can be placed in landslide hazard areas (provided the conditions listed in the county code are met).
- Point source discharge of storm water can be placed in landslide hazard areas (provided the conditions listed in the county code are met).
- It is the responsibility of the developers to verify the accuracy of mapped landslide hazard areas.

Landslide Hazard Areas mapped in the vicinity of the slope are shown in Figure 4.5.2. If the full 183-m (600-foot) height of the slope that failed in 2014 were used to calculate the required setback distance from the toe (as opposed to the 60-m (200-foot) high slope that had failed in 1951, 1967 and 2006), then the required setback is 90 m (300 feet). All of the structures affected by the March 2014 landslide were more than 90 m (300 feet) away from the toe of the slope and therefore not subject to land-use restrictions due to landslide hazard (Figure 4.5.1). Several of the building permits issued after the 2006 event did address flood hazards and wetland conservation.

³ This setback distance is greater than that required by the International Building Code.

The Washington Department of Natural Resources is responsible for regulating logging in this valley on non-federal lands. The area of the earlier (pre-2014) landslides was classified as a Mass Wasting Mapping Unit where logging was not permitted. In addition, to reduce the probability of a slope failure caused by groundwater recharge, the Washington Department of Natural Resources had instituted logging restrictions on this valley wall above the pre-2014 landslides and including a portion of the Whitman Bench identified as in the groundwater recharge zone of the landslide based on an assessment by Benda et al. (1988).

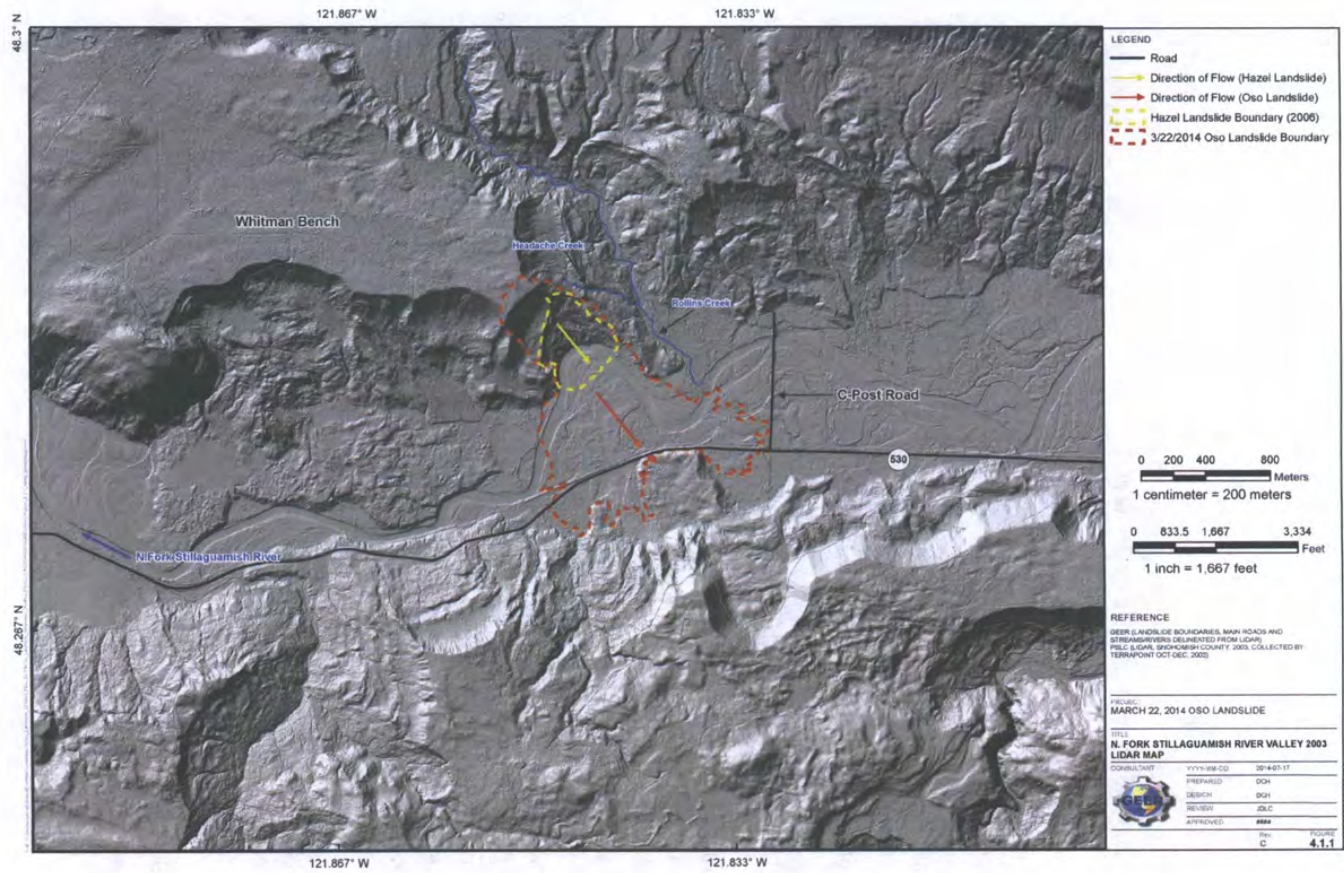
River Bank Stabilization

The Hazel landslide slope was a source area for sediment to the river to an extent believed to be adversely impacting the fish downstream since at least the 1930's. The sources of sediment were 1) erosion of the river bank as the river cut through the toe of landslide debris, and 2) sediment-rich run-off originating from the disturbed surface of the landslide. The fine sediment was accumulating in downstream areas of the river and degrading the fish habitat.

In order to reduce the impact of sediment on the fish resource, the Stillaguamish Tribe of Indians obtained a grant for \$1,000,000 in 2005 to move the river channel 150 m (500 feet) to the south and construct a log revetment. Before construction started, the river channel was relocated more than 150 m (500 feet) to the south due to the January 2006 landslide event. A modified revetment was constructed in August to September of 2006 to the north of the new river channel. The revetment wall was 430 m (1,400 feet) long and constructed with 5 layers of 18-m (60-foot) long, 0.6-m (2-foot) to 0.9-m (3-foot) diameter logs lashed together with steel cables and anchored with concrete blocks every 18 m (60 feet). The cables were kept slack to provide flexibility for the revetment to conform to settlement and lateral movement. The revetment wall reduced sediment loads enough after 2006 to promote a measurable increase in spawning of Chinook salmon downstream from the landslide. Two similar walls had been built in the recent past: one was a berm made of river bank material in 1960 that lasted less than one year, and the other was made of rock in 1962 that was overrun by the 1967 landslide.

Between 2006 and 2014, sections of the log revetment had settled about one-half meter (1.5 feet) and required one major repair following settlement that allowed the river to erode 3 m (10 feet) back toward the slope. This erosion likely resulted from undercutting due to the river excavating a pool in the channel along the outer edge of the river meander bend. A tribal representative observed the log revetment two days before the 2014 Oso Landslide event and reported that further erosion or new activity in its vicinity was not noticed.

Figure 4.1.1 North Fork Stillaguamish River Valley (2003 lidar map).



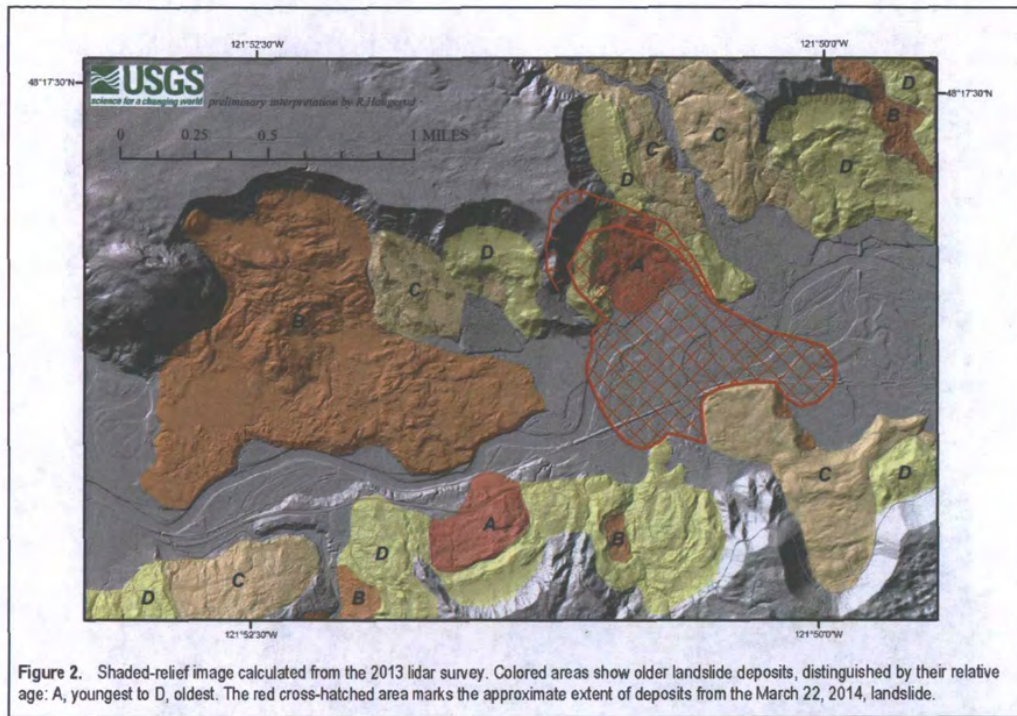


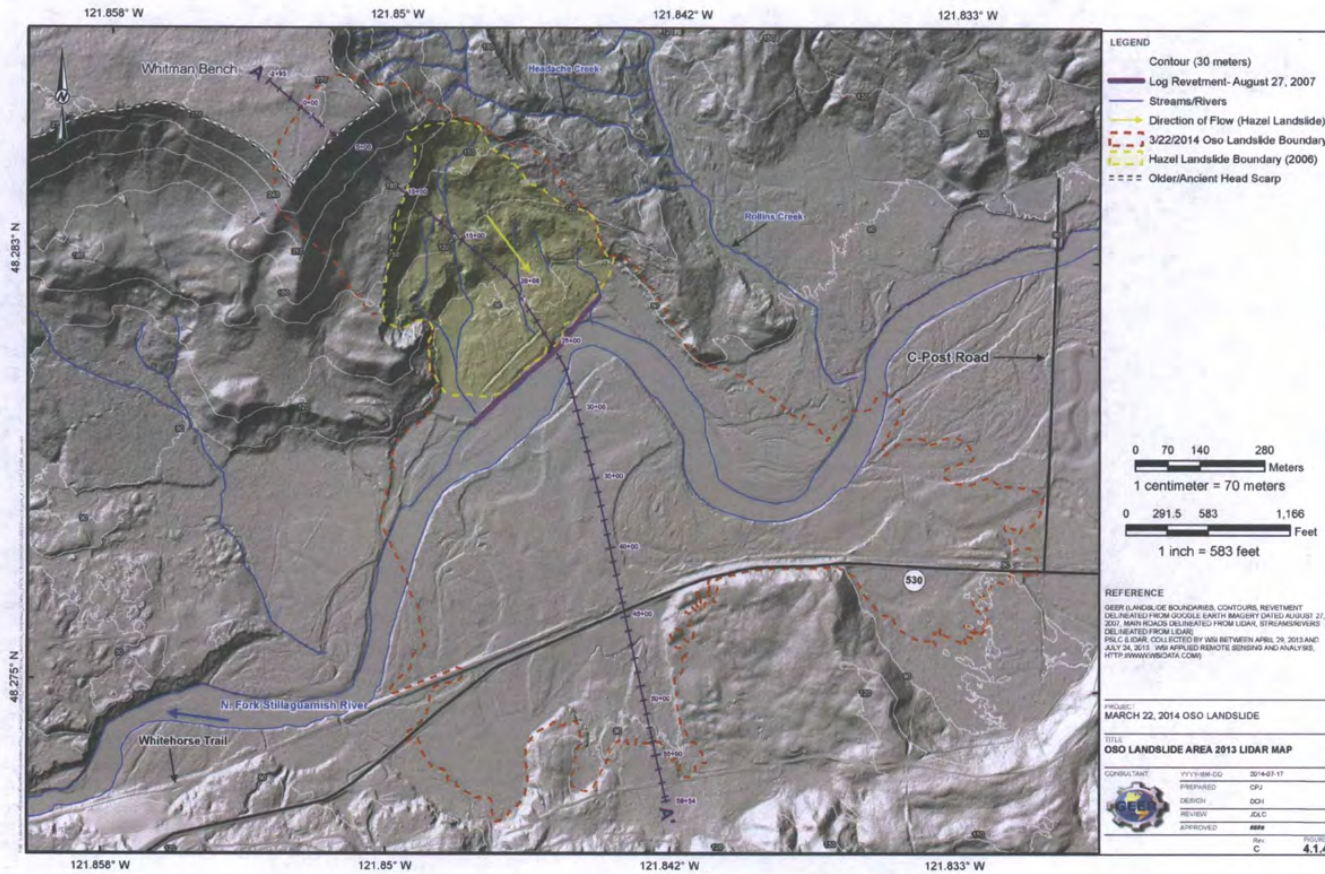
Figure 2. Shaded-relief image calculated from the 2013 lidar survey. Colored areas show older landslide deposits, distinguished by their relative age: A, youngest to D, oldest. The red cross-hatched area marks the approximate extent of deposits from the March 22, 2014, landslide.

Figure 4.1.2: Relative age classes of pre-2014 landslides in the immediate vicinity of the 2014 Oso Landslide (from Haugerud, 2014).



Figure 4.1.3: Oso Landslide area 2003 lidar map.

Figure 4.1.4: Oso Landslide area 2013 lidar map.



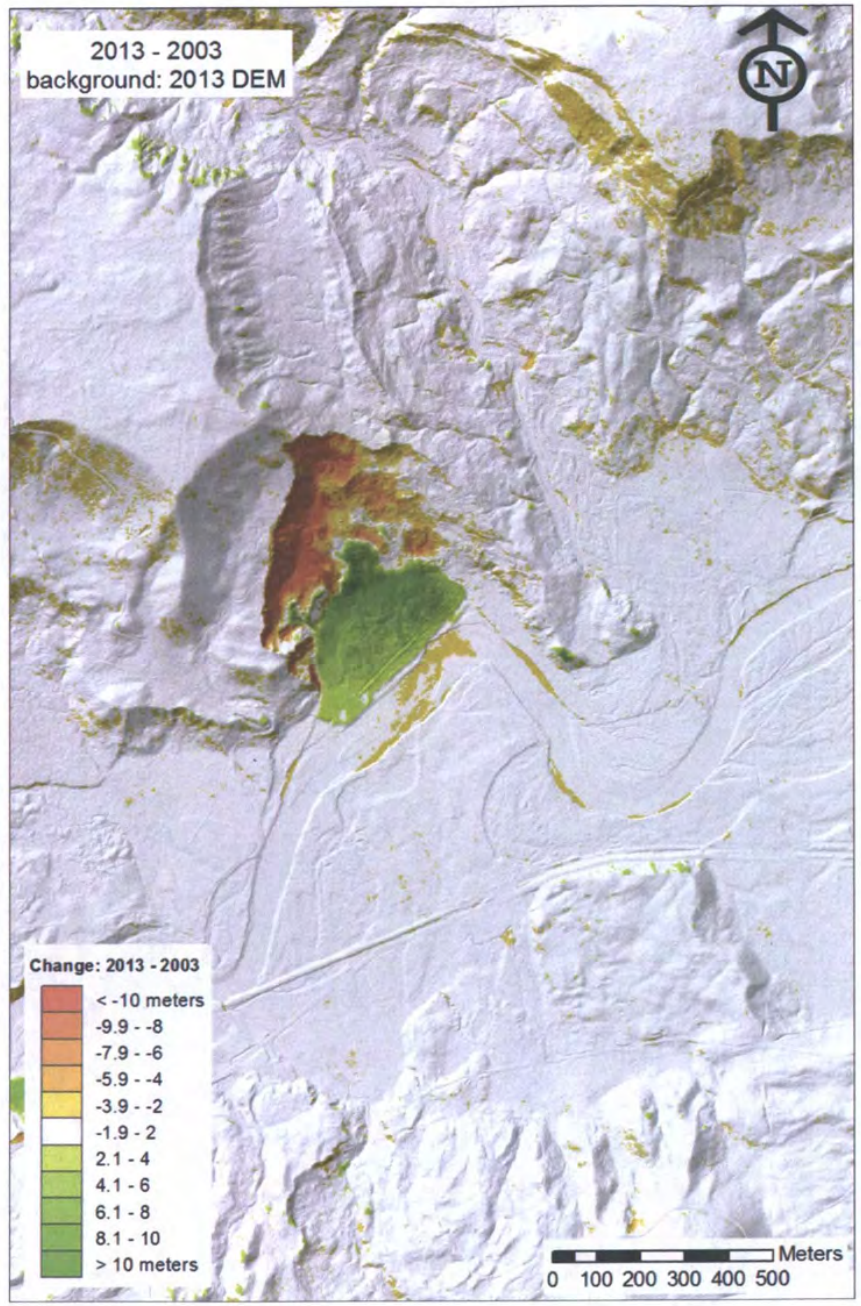
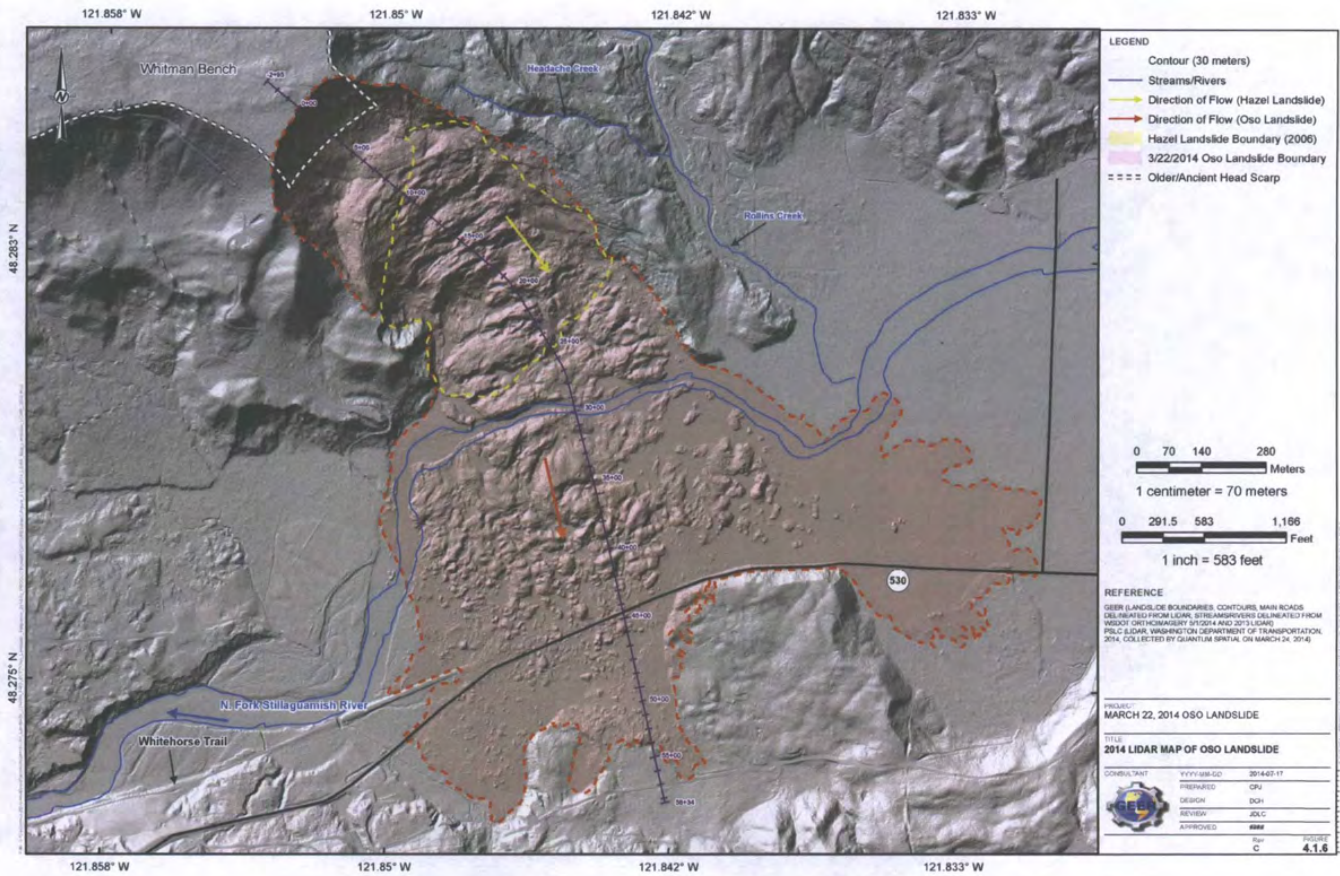


Figure 4.1.5: Elevation differences between 2013 and 2003 lidar data sets. Color keyed to vertical change, with red hues representing decrease in elevation (net erosion), and green hues representing increase in elevation (net deposition).

Figure 4.1.6: Oso Landslide area 2014 lidar map.



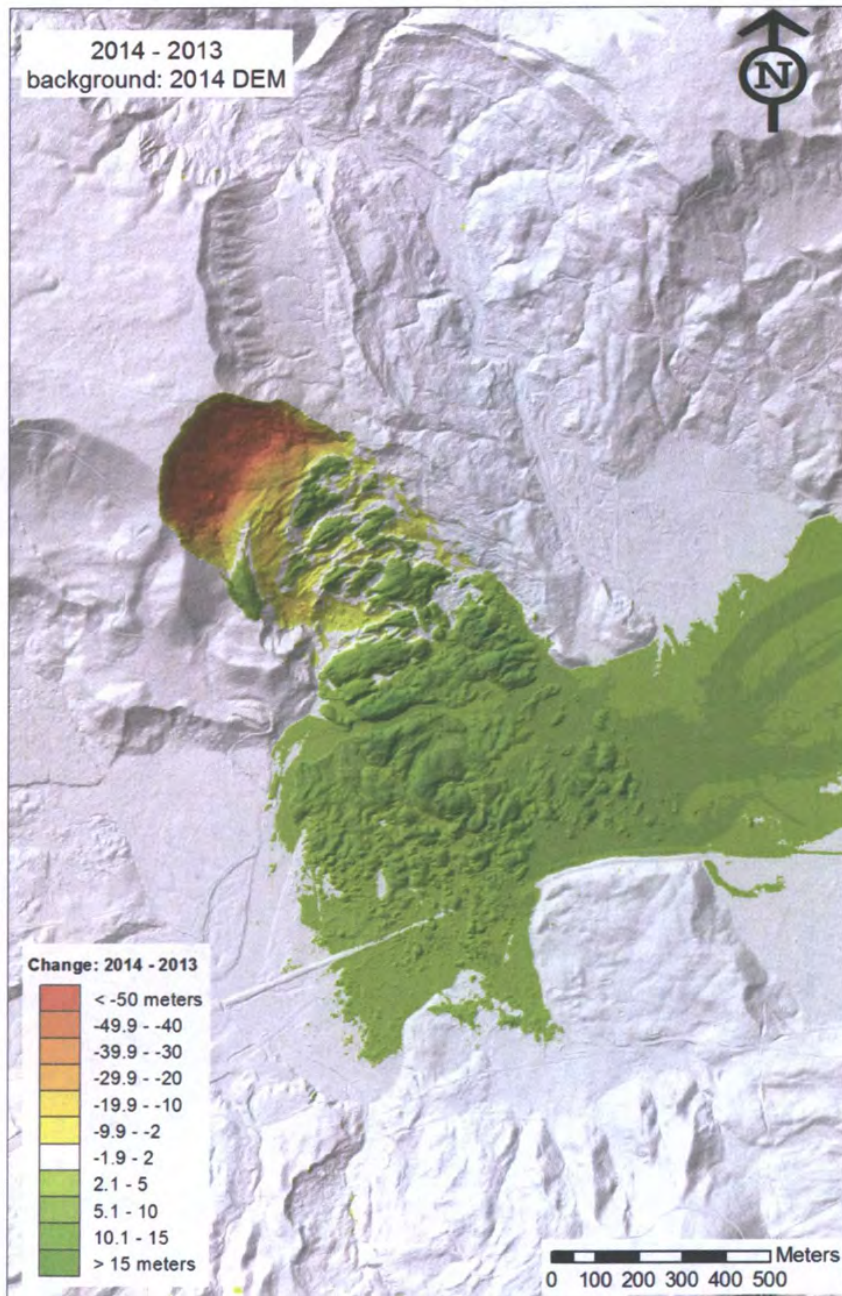


Figure 4.1.7: Elevation differences between 2014 and 2013 lidar data sets. Color keyed to vertical change, with red hues representing decrease in elevation (net erosion), and green hues representing increase in elevation (net deposition).

Figure 4.1.8: Topographic Profile Section A-A'

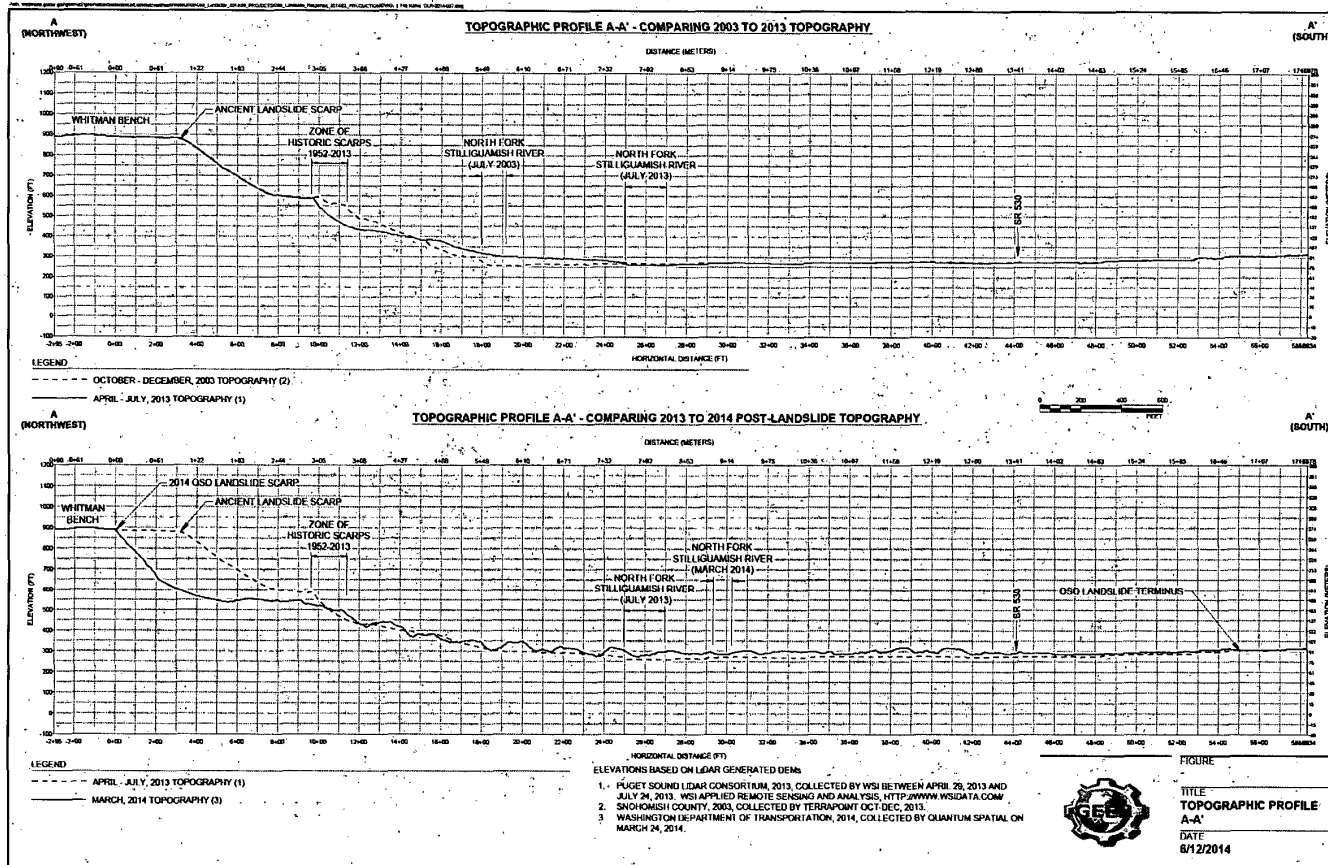


Figure 4.2.1 Historic Oso/Hazel Landslide disturbances and scarps from 1958 to 2013.

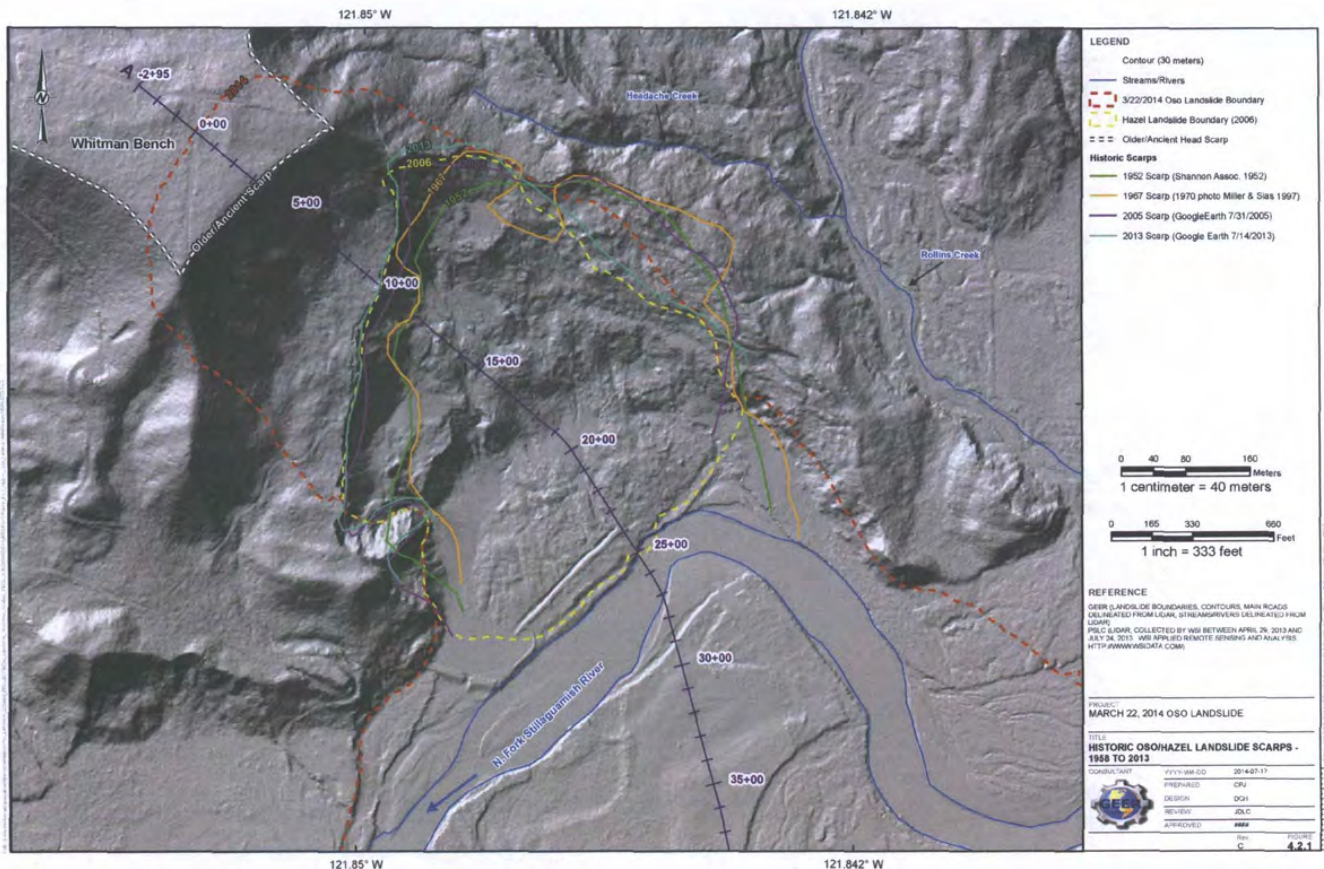


Figure 4.5.2: Land classified as geologically hazardous areas in vicinity of the slide (Snohomish County Map dated 2007)

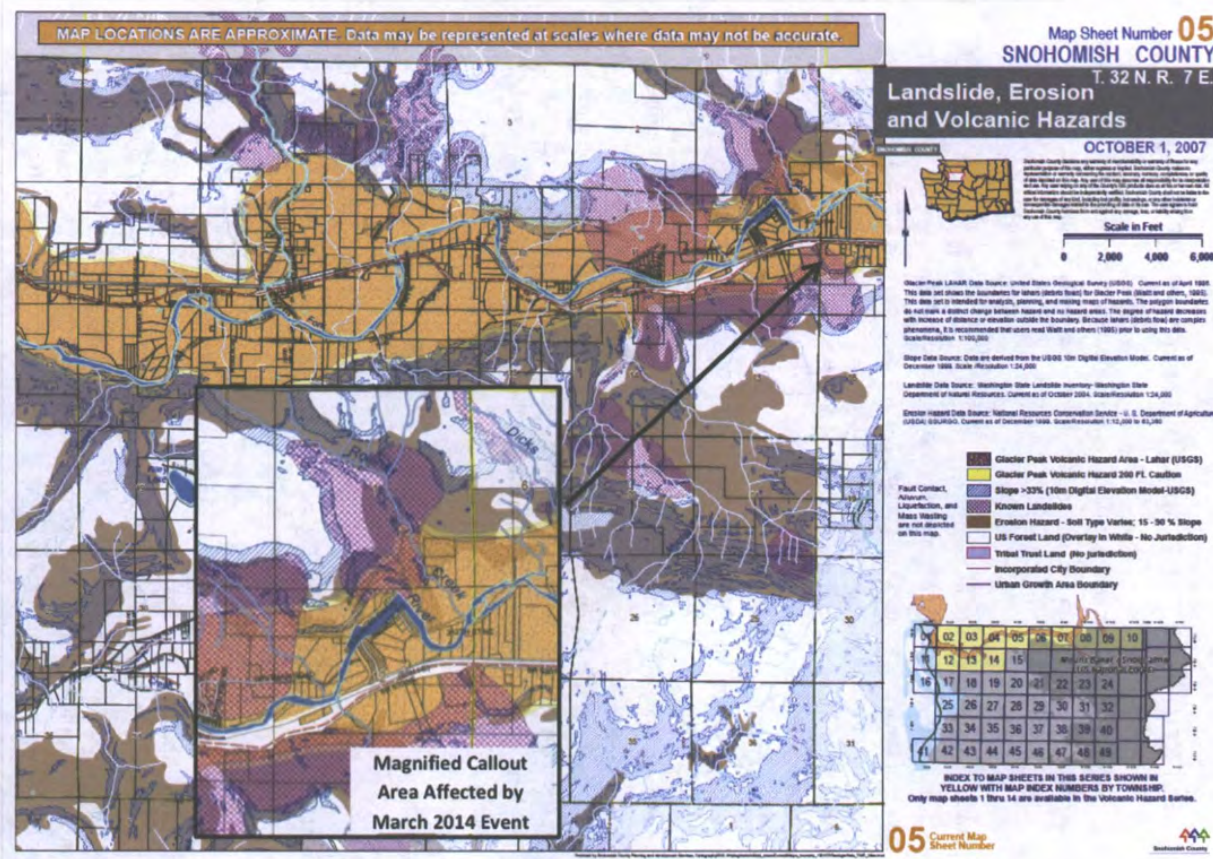


Figure 4.5.2: Land Classified as Geologically Hazardous Areas in Vicinity of the Slide (Snohomish County Map dated 2007)

5. DATA COLLECTION FOR THE 22 MARCH 2014 LANDSLIDE

The GEER team spent four field-reconnaissance days collecting data and making observations on the landslide (see Appendix A). The data and observations were generally related to one or more of the following:

- vegetation on and near the landslide,
- geologic strata within the landslide and exposed in the scarps,
- morphology of the landslide mass and deposits,
- characterization of stratigraphy and material properties within the landslide
- sources of surface water and groundwater in and near the landslide,
- the mechanism of movement,
- the direction of movement, and
- the impact on structures and infrastructure.

The GEER team also collected data on the event from other sources, such as seismic stations, weather stations, stream gages, and accounts from eyewitnesses and first responders. Laboratory testing and radiocarbon dating was also performed on a limited number of samples collected by members of the GEER team while in the field. With exception of the precipitation and stream gage data, which are presented in Section 3 along with the climate description, the collected data and observations are summarized in this section.

5.1 Site stratigraphy

The stratigraphy of the slope at the Oso Landslide site is disrupted below the elevation of ancient headscarp apparent on the 2003 lidar image (Figure 4.1.3). Reconnaissance descriptions of the site stratigraphy follows; note that the unit thicknesses and elevation ranges reported here are gross estimates based on limited field mapping and are complicated by the long history of sliding downslope of the ancient slide scarp apparent on the 2003 lidar image. The undisturbed section now exposed in the 2014 headscarp of the Oso Landslide, together with exposures on the landslide lateral margins, indicates that the site is underlain by deposits that roughly parallel the typical sequence of Puget Lowland deposits. The lowest, and oldest material exposed at the landslide site consists of limited exposures of oxidized fluvial sands near river level on the western margin of the slide that we interpret to be pre-glacial floodplain sediments (Qoly) of Olympia Age (last inter-glacial) that correspond to the radiocarbon-dated exposure reported by Dragovich et al. (2003) on the eastern margin of the landslide (Figure 2.2.1). These deposits are overlain by glacial lacustrine deposits (Ql) associated with the most recent (Vashon) glacial advance. The glacial lacustrine deposits grade vertically upward into silty to sandy advance outwash deposits (Qa) that are, in turn, overlain by Vashon-age glacial till (Qt). Above the till lie the uppermost exposures, consisting of recessional outwash deposits (Qo) that form the topographic surface of the Whitman Bench at an elevation of approximately 274 m (~900 ft) near the landslide headscarp. Prior to the 2014 Oso Landslide, the material on the face of the ancient

slide scarp and on the bench upslope of the 2006 landslide and ahead of the 2014 headscarp, was likely composed of failed blocks of recessional outwash, till, and colluvium derived from reworking of these materials from the ancient slide scarp. Material located downslope within the 2006 landslide was likely a mix of these units underlain by lacustrine material at depth. The site deposits are listed below from stratigraphically highest (youngest) to stratigraphically lowest (oldest).

Qls — ***Holocene landslide deposits***: colluvial material derived from prior (pre-2014) failures involving the units described below, and where observed intact in the 2014 landslide deposit involve variable thicknesses of oxidized material derived from outwash, till, and sheared lacustrine deposits.

Qo — ***Recessional outwash***: unconsolidated, cohesionless, well-sorted fluvial (clast-supported) sand and gravel with cross-bedding indicative of flow up valley (i.e., to the east); extensively oxidized and highly permeable. Rapidly spalling and sloughing where exposed on the steep 2014 landslide headscarp. Recessional outwash composes approximately 40 m (130 ft) of the in-place section, from about 228 m to 268 m (750 ft to 880 ft) in elevation.

Qt — ***Glacial till***: gray consolidated diamicton consisting of sand to boulders of widely varying lithology set in a matrix of dense gray silt and clay; impermeable and cohesive with seeps visible on the upper contact and in outcrops on adjacent ridges; holds cliffs supporting landslide headscarp, but fractured into blocks where transported. Lower contact of the glacial till was covered with talus and not clearly exposed at the 2014 headscarp. Composes an estimated 18 m (60 ft) of the in-place section, from about 207 m to 228 m (680 ft to 750 ft) in elevation.

Qa — ***Advance outwash***: gradational lower contact, coarsens upward, non-cohesive to poorly consolidated medium sand to very fine silty sand. Weak and flows readily where saturated. Composes an estimated 30 m (100 ft) of the in-place section, from about 176 m to 207 m (580 ft to 680 ft) in elevation.

Ql — ***Glacial lacustrine***: gray overconsolidated, interbedded layers of fine sand, non-plastic silt, and clay to clayey silt; layered (varved) to massive, with seeps and springs associated with the top of exposure on east lateral margin of slide, and from exposures on west margin of slide. Silt and clay content of lacustrine material varies greatly and some outcrops exhibit flow structures and rafting of blocks of varved material in less competent material that has flowed away from the outcrop. Composes approximately 100 m (330 ft) of the in-place section, from < 76 m to 176 m (< 250 ft to 580 ft) in elevation (i.e., down to river level).

Qoly — ***Olympia Age fluvial (floodplain) deposits***: flat lying, oxidized beds of fine to medium grained sand exposed near base of slope on western margin of landslide.

5.2 Field Observations

Some key observations of the GEER team are spatially located on Figure 5.2.1. These include the locations of samples for radiocarbon dating and soil testing, hand auger borings, soil descriptions, sand boils, and tree descriptions. These observations, and others, are described below and accompanied by photographs to help illustrate particular findings and their apparent significance.

With respect to vegetation, the GEER team found significance in observations of the locations of deciduous and conifer logs in relation to forest stand patterns apparent in earlier photography and from comparison with the size of standing trees outside the landslide margins. Within the conifer forest, observations were made on the size of trees and their density, and this was compared to the size and density observed on parts of the landslide. Observations were made on the condition and orientation of fallen trees, and where trees had not fallen. Parts of the landslide still have an upright forest duff-topsoil profile, with still-living vegetation (e.g., ferns), whereas other parts of the landslide have no preservation of the original ground surface.

Observations on the morphology of the landslide include how the existing landforms provide evidence of rotation, extension, localized compression, discrete headscarp failures, post-failure talus formations, superposition, debris flow, and liquefaction. Evidence of all of these processes were observed in parts of the landslide and recognized by their morphology, structure, and deposits. Understanding of the stratification of the landslide deposit was augmented by 16 hand auger probe holes. Aerial imagery shows quite well where brown, oxidized material (recessional outwash and colluvium) is on the surface. We used the hand auger primarily to probe the thickness of this cover and to determine if this material could be found underneath a cover of the gray lacustrine deposits mobilized by the landslide. The locations of these probe holes are shown in Figure 5.2.1 (labeled HA-1 to HA-16).

Soil samples were collected at select hand auger holes and from other surface locations. These samples were tested in the laboratory for moisture content, gradation and plasticity to help understand the range of strength and permeability parameters that could have existed prior to the failure. Sample locations are shown in Figure 5.2.1 and the results are presented below. Additional characterization of the deposits was done visually based on exposures on the landslide surface and in scarps, observations indicating the fluidity of the material comprising the deposit in comparison with source materials, and any apparent superposition or sequence of emplacement reconstructed from field relations.

The GEER team walked part of the Headache Creek drainage adjacent to the Oso Landslide noting springs and seeps in that area, and the proximity of the creek to the margin of the landslide, but recorded observations on groundwater flow were made from within the landslide and along its margins. Some seepage was emanating from the headscarp at the contact with the till, but did not appear to be a large amount and was not notably influencing scarp retreat where it was observed. It is understood from discussions with Snohomish County geotechnical

professionals that seepage volumes visible at the headscarp were small even immediately after the Oso Landslide occurred. However, many seeps and areas of soil sapping or piping tunnels were observed in the exposure of the lacustrine materials along the east margin of the landslide, as well as locally on the western margin as shown in Figure 5.2.2.

The direction of landslide and debris flow movement was interpreted based on interpretation of the landslide morphology, differential scour on trees, trajectories of objects, and emplacement of debris and the impact on infrastructure, most notably pavement and guardrail from SR 530. Tree distribution on the landslide mass in terms of density, size and orientation was found to be a useful characteristic that could be quantified. The analysis is discussed in Section 5.3.

Landslide Zones

Several types of key observations were made in the field and through the analyses, and these tended to be spatially distributed. Based on this, we identified six distinctive zones (Zone A in the north through Zone F in the south) and several subzones of the Oso Landslide mass that are characterized by different styles of deformation, geologic materials, vegetation, and geomorphic expression (Figure 5.2.3). In the following subsections, we describe briefly each zone and pertinent observations within it supporting our interpretation of the landslide behavior.

Zone A — Headscarp and back-rotated block

We subdivided Zone A into four sub-zones, A1 through A4.

Zone A1 consists of the landslide headscarp with in-place exposures of oxidized tan to brown recessional outwash and unoxidized gray glacial till (Figure 5.2.4). Active seepage was observed at the sharp contact between these two units. The overlying recessional outwash was composed of unconsolidated clast-supported (fluvial) sands and gravel with cross bedding indicative of flow up valley (i.e., to the east). The headscarp face composed of this non-cohesive material was constantly raveling during our fieldwork, with occasional debris avalanches cascading down the face of the headscarp and accumulating as talus at the base. At the time of our field reconnaissance, the scarp remained highly unstable, with net scarp retreat estimated to be roughly 3 to 6 m (10 to 20 feet) in the two months that had elapsed since the Oso Landslide occurred. The underlying till supports a near vertical cliff, with sandy talus accumulating at and burying the base of the headscarp and obscuring the contact with the advance outwash below the till.

Zone A2 consists of a large, down-dropped and back-rotated block with mature, second-growth trees that have been nearly uniformly back-rotated and felled, such that their crowns point upslope (Figure 5.2.5 a and b). The surface of this block is recessional outwash and represents the original ground surface of the Whitman Bench, and patches of the original forest floor are preserved relatively intact on the surface of the down-dropped block. The trees were analyzed as

Areas 1 and 2 in Section 5.3 and they were found to be among the largest on the landslide and to have the greatest density and uniformity of orientation.

Zone A3 consists of till fragments that came down along with and buttressed the downslope side of Zone A2. On the eastern margin of Zone A3, the till travelled farther downslope than other parts of Zone A3, creating a blocky debris field with relatively intact blocks of till, some up to >3 m (10 ft) high. Distal portions of this material overlap the material comprising Zone B.

Zone A4 consists of a scarp-face failure in which till fragments and overlying recessional outwash material collapsed onto and over-rode a portion of the slump block that forms Zone A2 (Figure 5.2.6). Other failures off the headscarp have started to infill the closed depression (moat or graben) on the upslope side of Zone A2 at the base of Zone A1 with loose debris eroded from the over-steepened scarp face, rapidly smoothing the sharp, angular features of the headscarp as the moat fills with talus.

Exposures on the lateral margins of the landslide in Zone A reveal down-dropped material from along the ancient slide scarps to the east and west along the physiographic margin of the Whitman Bench. The exposure on the eastern margin of the landslide reveals finely layered deposits filling depressions in the space between the ancient slide scarps and down-dropped blocks (Figure 5.2.7), and which appear to consist of talus material similar to that presently filling the depression between Zones A1 and A2. This ancient talus buries downed trees, one of which was sampled for radiocarbon dating (sample Oso3 in Table 5.3.5).

Zone B — Rotational Block Field

The topography of Zone B is characterized by a series of transverse ridges and depressions that form an extensional field of back-rotated blocks as shown in Figure 5.2.8. Field mapping across a number of these blocks shows a downslope pattern of repeating elements of the stratigraphic section in a manner indicating back rotation and extension—deeper units are exposed on the downslope side of blocks, with the tops and uphill sides of high-standing blocks preserving oxidized recessional outwash and patches of forest floor, and the downhill side of blocks being buttressed by till or defined by arcuate scarps in lacustrine material, some of which preserve failure surfaces with steeply inclined slickensides (Figure 5.2.9). The pattern of rotational blocks repeating the stratigraphic section is consistent with extensional movement along a décollement or slide plane at depth. Scarp surfaces and the floors of depressions expose gray lacustrine deposits; standing water was filling the floors of several of the depressions at the time the GEER team was in the field. Portions of the floors of depressions were semi-liquid and demonstrably could not support a person's weight.

The appearance of extension is recognized in the aerial photography by a decreasing density of trees lower on the slope and a decrease in the extent of the mass covered by the brown, oxidized recessional outwash. All but one of the hand auger holes in this area encountered gray

glaciolacustrine deposits under 1 to 12 feet (0.3 to 3.7 m) of overlying recessional outwash, even when augers were located near the tops of hummocks. The only exception was HA-1, which was terminated on large gravel at 3.5 feet (1.1 m) depth. The in-place stratigraphic section at the main scarp reveals about 130 feet (40 m) of outwash and till overlying the glaciolacustrine sediments, so this profile has apparently been thinned considerably by the extension during the sliding. The extension is clearly shown by the dragging of two trees (≈ 0.6 m in diameter) and the skid marks they left on a recessional outwash hummock, shown in aerial view and from the east in the photographs on Figure 5.2.10a and 10b. At another nearby log, track-like impressions in the loose surficial sand indicate it impacted violently and bounced before coming to rest (Figure 5.2.10c).

On the western lateral margin of Zone B intact, gray to blackish laminated (varved) flat-lying glaciolacustrine clay, silt, and fine sands can be traced laterally for 60 to 80 feet (18 to 25 m) along the banks of a ravine. These beds appear to be in-place glaciolacustrine deposits that help define the lateral boundary of the landslide. Flow emanating from silty and sandy layers in these beds readily fluidized and entrained this material once the free face was formed (Figure 5.2.11). This suggests the potential to liquefy in-situ beds within the glacial lacustrine unit, Q1.

A pile of logging-road ballast (angular serpentinite clasts) located in the eastern portion of Zone B (at point 5/24-20 on Figure 5.2.1) shows that the material in this portion of Zone B originated at the top of the site, likely near the edge of the Whitman Bench. Trees in Zone B are represented mostly by Area 3 (Section 5.2); the trees are similar in size but less dense than those in Areas 1 and 2 (Table 5.2.1), distinguishing Zone B from Zone A2.

Table 5.2.1: Tree characteristics in areas 1 through 10 as defined in Figure 5.2.4 (note that area 4NW duplicates information already in area 4)

Area (map)	Number of Trees	Maximum Length (ft)	Minimum Length (ft)	Average Length (ft)	Average Compass (degrees)
1	297	187	32	100	125
2	245	184	21	97	135
3	92	187	45	100	136
4	182	175	36	96	103
4NW	74	175	46	106	104
5	113	195	40	96	126
6	56	150	16	58	74
7	264	81	9	32	86
8	127	138	15	48	86
9	285	81	7	25	85
10	107	89	12	41	91

Deposits that are herein called sand ejecta (Figure 5.2.12) were observed in Zone B (and in Zone E). Sand ejecta deposits may be another expression of the same phenomenon as a sand boil (see

Zones E and F) – confined elevated water pressure and liquefaction of susceptible soils at depth. The sand ejecta deposits were not observed in low spots, but rather in what appear to be compression ridges. They appear to represent ejection by water of sand from cracks as the mass was emplaced. Sand ejecta deposits are not typically associated with earthquake-induced liquefaction and their mechanism of origin on the Oso Landslide is not as confidently understood as the sand boils. The fact that they were generally observed on higher ridges suggests that they could be associated with the thrusting upward of the ridges. Sand ejecta deposits were observed near the Zone B-Zone C interface.

Zone C — Debris Flows Along Lateral Margin

Zone C extends along the left (eastern) lateral margin of the Oso Landslide from Zone A down to Zone E, past the North Fork Stillaguamish River channel. Much of Zone C consists of debris flows along the lateral margin of the slide that overlap deposits in Zone B. Back rotated and relatively flat-lying lacustrine deposits are exposed on the floor and in the lateral margin of Zone C. Exposures along this lateral margin include lacustrine sediments that flowed, and which have rafted blocks of more intact clay embedded in them (Figure 5.2.13A).

Locations where several actively flowing seeps were mapped along the eastern margin of the landslide correspond to the uppermost areas of Zone C (Figure 5.2.13B). Groundwater seeps identified in this area emanating from the eastern wall of the 2014 landslide had visually estimated flow rates of 5-10 gpm, 1-2 gpm, 3-5 gpm, 2-5 gpm, and 10 gpm (1 gpm = 3.79 Lpm). These crude estimates collectively amount to 21 to 32 gpm, or about 30,000 to 46,000 gallons per day. As the topographically-defined drainage divide between the Oso Landslide and the neighboring Headache Creek basin is virtually at the eastern margin of the Oso landslide, this flow is interpreted to be groundwater captured from the drainage basin of Headache Creek.

In the vicinity of the seepage, evidence also was observed of internal erosion (piping) in the Advance Outwash (sand) just above the contact with the Glacial Lacustrine deposits (silt and clay) [Figure 5.2.14]. "Piping from internal erosion was also observed at this interface in the older landslide scarp immediately to the east.

An exposure of relatively flat-lying gray lacustrine sediments, consisting of silty fine sand and a zone of ≈ 10 mm thick clay layers with silt partings (Point 5/24-23 on Figure 5.2.1), is similar to an exposure in ravine on west side of slide (Points 5/24-15&16 on Figure 5.2.1), suggesting that lacustrine deposits were originally continuous across the area that is now the landslide. Fallen, small deciduous trees were observed along the margin in Zone C but not to great enough extent to be mapped or analyzed as part of this effort.

Zone D — Sheared Lacustrine Sediments

Zone D consists dominantly of sheared gray to blackish lacustrine material exposed in a blocky debris field laying transverse to the slide and bisected by the present course of the river. Hand auger borings and trenches into the surface of the material in Zone D (Figure 5.2.15) revealed from 1 to 5.5 ft of outwash sand overlying glaciolacustrine deposits or, where glaciolacustrine deposits were at the surface, glaciolacustrine deposits to the depth of refusal (12.5 ft, 3.8 m). This supports the inference based on surface observations that the materials at and near the surface in this area are from the deepest part of the stratigraphic section exposed on the slope. It also appears that the material exposed at the surface in this zone extends beneath and underlies the blocky hummocks in the southernmost area of Zone B. The Zone D landslide deposits exposed in the walls of the newly incised North Fork Stillaguamish River channel are composed of disturbed lacustrine material that ranged from semi-intact blocks (10 centimeter to 3 meter diameter) of cohesive clayey-silt to silty clay in a disturbed matrix of nonplastic silt. Along the southern margin of Zone D, the gray lacustrine material ran up and onto the surface of blocks in Zone E and partially buried trees that had rafted down the slope in Zone E (Figure 5.2.16). The surface contact between these zones is distinct.

When the river breached the landslide mass, it did so through Zone D and it cut its channel within approximately one day. At the time of the GEER visit about two months after the landslide occurred, the channel was approximately at its pre-slide elevation but the channel was much narrower than its pre landslide configuration (WSDOT communication). The channel was actively widening at the time of the GEER visit, even without flood activity, and an abundance of tension cracks in the landslide deposits along the channel indicated the banks were unstable and that the channel would continue to widen (Figure 5.2.17). Essentially no displaced trees were observed in the landslide deposits in Zone D. The river cut exposure consists of lacustrine material.

Zone E — Block Field

Zone E consists of high standing blocks that diminish in size to the south. Oxidized sand and gravel, interpreted to represent colluvial material from the face of the ancient landslide scarp, cover most of the blocks in the northern portions of Zone E giving the blocks a rounded, mounded appearance. The mounds in the north end of Zone E block locally retain preserved patches of original forest floor with rooted, in-place ferns (Figure 5.2.18). The blocks in the southern portions of Zone E are predominately composed of lacustrine material without a veneer of colluvium or vegetation.

Trees on the surface of Zone E are both coniferous and deciduous. The coniferous trees are at the northern part of the zone and are dropped in various orientations, with some remaining subvertical (Figure 5.2.19). Large trees, with one observed to be >1.5 m in diameter, occur along the northern margin of the western portion of Zone E. Along this edge of Zone E (the northern

margin), many trees are partially over-run and buried by material from Zone D (i.e., along the contact between zones D and E). In one location along the western portion of the border with Zone D, large trees are inter-twined across a collision zone between two blocks (Figure 5.2.20).

Elsewhere on the landslide (other than at the distal deposition margin), the felled trees are nearly all parallel to the direction of movement, and with roots downslope, indicating that a rapid, downslope movement caused them to fall (Figures 5.2.6 and 5.2.5a, b). In the area shown in Figure 5.2.18, many of those trees appear to have been hit, flipped or broken by the impact. Another sign of impact in this area is a thin gray, gravelly, sandy veneer which is no more than two inches thick and generally less than one inch thick. A typical occurrence is shown in Figure 5.2.21. In some locations this veneer appears to define a certain elevation in a channel or basin (Figure 5.2.22) and in others it is splashed randomly on higher, sandy ground. Splashed veneer locations appear on both sides of the contact separating Zones D and E, whereas the high water mark veneers were observed only in Zone E.

Relatively small, deciduous trees are increasingly prevalent toward the middle and distal areas of Zone E where progressively smaller block sizes reflect disintegration of the original ground surface of the 2006 landslide. Most of the trees in this area are no longer vertical and appear to have been rafted into place, as shown in Figures 5.2.23 and 5.2.24 though at least some near the distal part of the zone appear in place, as shown in Figure 5.2.25 and on the report cover.

Sand ejecta were observed in Zone E (Figure 5.2.26). As in Zone B, the sand ejecta deposits were not observed in low spots, but rather in compression ridges where they appear to represent ejection by water of sand from cracks as the mass was emplaced. Sand ejecta were observed in the northern part of Zone E near the contact with Zone D. Sand boils (Figure 5.2.27) were also observed in the Zone E. Sand boils are a common observation when liquefaction has occurred from earthquakes. They indicate that at some depth below the ground surface the water pressure in the soil reached or exceeded the total overburden pressure, causing the soil to lose essentially all of its strength and flow like a liquid. Some of the flow then escapes to the ground surface, carrying the liquefied material with it, and creates the sand boils. The soil that forms the mound on the surface generally represents the soil that liquefied, but other material can also be entrained and deposited, or could have been washed away in the two months between the landslide and our observation of the boils. Without excavation it is not possible to tell from what depth the material has come, but sand boils from earthquakes most often indicate liquefaction in the upper 50 feet (15 m). Sand boils from earthquakes typically occur soon after the shaking has stopped and it is expected that these sand boils and ejecta formed soon (within seconds to minutes) after the slide came to rest.

Trees in Zone E are represented by those in Area 4 and the results of size and orientation analysis are shown in Table 5.2.1.

Zone F — Debris flow runout

Zone F consists of gray silty debris flow material, with isolated partially disintegrated blocks of other material (e.g., lacustrine clay and till) smaller in size than present in Zone E. Large areas of Zone F were thoroughly disturbed, reworked, excavated or hauled away during search and rescue and recovery operations. Portions of this zone were still soupy and semi-liquid with little to no bearing capacity during field reconnaissance. Even two months after the event, the surface deposits remain very soft, easily penetrated to at least 5 foot (1.5 m) depth by static pushing (without rotation) of a 3 inch (76 mm) hand auger (HA-11).

The distal debris flow deposit consists of logs, construction debris, silt, sand, and small blocks of till and clay. Construction debris and wood from the floodplain forest was concentrated at and piled up along the distal edge of the landslide deposit, which ran some distance uphill before coming to rest on the southern valley wall or flowing back downhill. Most of this debris had been cleared by the time of the GEER field reconnaissance; however, it appeared that the forest cover and buildings that had been present on the floodplain were entrained and deposited along the frontal portion of the debris flow, with the leading edge incorporating logs oriented orthogonal to flow.

Figure 5.2.28 shows a landslide-displaced recreational vehicle that appears to have been unmoved by the rescue and recovery efforts. This recreational vehicle is a few meters above the valley bottom and appears to have been pushed into place by water and woody debris, and the root-wad and log that caused the damage to its side is still present adjacent to the vehicle.

Evidence was also observed that the debris flow was fluid enough to have been redirected by the southern valley slopes or other topography. We observed indicators of flow trajectory that support some eyewitness accounts that the flow reversed in direction, such as markings on trees, cars that have been pushed into trees (Figure 5.2.29) and a veneer that appears to represent a high water mark in a basin that opens to the south (Figure 5.2.22).

Individual logs that must have been part of the log revetment that was built after the 2006 landslide along the north side of the North Fork Stillaguamish River were identified by the presence of attached steel cables, numbered metal identification tags, and drilled holes (Figures 5.2.30 and 5.2.31). These logs had been located along the right bank of the river at the time of the landslide and were found in locations distributed along the runout path in a manner consistent with laterally spreading and diverging flow lines within Zone F.

Excavations along highway 530 that were open during field reconnaissance revealed that the asphalt roadway surface was preserved beneath debris flow deposits in all but two locations where it was ripped up by the debris flow (Figure 5.2.1). Plucked and transported sections of the asphalt road surface, along with intact portions of its engineered base course, were found at

locations south of SR 530 (Figure 5.2.32). Drainage pipe and filter fabric (Figure 5.2.33) and pieces of guardrail and timber supports (Figure 5.2.34) also were found south of SR 530. Preserved sand deposits on some sections of ripped up asphalt road surface document that the first material that over-rode SR 530 was hyperconcentrated flow rather than debris flow (Figure 5.2.35).

Sand boils were observed in the Zone F deposits. Sand boils indicate that there was elevated water pressure and liquefaction at depth in the deposits of Zone F. Sand boils were also observed in Zone E. Sand boils are visible now in low lying areas that may have originally or subsequently been flooded.

The travel vectors (vector from point of origin to depositional location) of identifiable materials as recorded by FEMA on a map examined by members of our team also point to a similar pattern of diverging flow lines for material caught up in the flow that surged through Zone F (Figure 5.2.36). In one location where the original terminal margin of the debris flow was preserved the flow front was about 2 feet high.

Generalized movement trajectory information was provided to the GEER team by Snohomish County. This information is plotted in Figure 5.2.36 as black polygons and was based on rescue and recovery operations during the first two months after the Oso Landslide occurred. It indicates a pattern of movement that is basically intuitive. Additional observations made by the GEER team also are plotted in Figure 5.2.36 which gives a pattern that is more complicated in detail, but consistent with the generalized trajectory information. The log revetment (magenta line in Figure 5.2.36) that was constructed along the right bank of the North Fork Snohomish River is the likely source of cabled, rilled, and tagged logs (magenta circles) that were identified in two areas within Zone F (Figure 5.2.36). Other revetment logs probably were deposited in Zone F but were removed by rescue and recovery operations before the GEER team had an opportunity to perform its reconnaissance.

Pieces of asphalt roadway from SR 530 (black triangle symbols in Figure 5.2.36) provide additional trajectory details. These pieces probably were plucked from the eastern of two sections of missing asphalt because only the eastern section was elevated and had a guard rail. A section of guard rail and timber guard-rail support elements (gray rectangle symbols in Figure 5.2.36) were found at positions near the asphalt pieces but farther south. The movement trajectory indicated by the asphalt pieces and guard rail section is parallel to the margin of the Oso Landslide deposit.

Scuff marks on standing tree trunks (yellow arrow symbols in Figure 5.2.36) also provide useful trajectory information. The scour or scuff marks probably were made mostly by transported tree trunks and debris that were being transported by the debris flow, hyperconcentrated flow, or water flow during the initial phase of slope movement and runout. One standing tree in the southeast lobe of Zone F (blue arrow symbol in Figure 5.2.36) had a pickup truck effectively

wrapped around its base (Figure 5.2.29) as if it were pushed into the tree from the south or southwest.

5.3 Discussion of Observations

This discussion section provides context for some of our observations. The mission of the GEER reconnaissance is to observe conditions in the field rather than determine the causality of the event. However, the extent of our reconnaissance effort has allowed us to point to some of the factors that we believe pertinent to the landslide at Oso.

Tree Distribution Following Failure

Mapping of the trees at the landslide site was performed using a high resolution orthomosaic imagery file taken by the Washington Department of Transportation on March 24, 2014, two days following the event. Trees were digitized as vectors from top to base (crown represented with a red dot) and their lengths measured in feet as shown in Figure 5.3.1. The landslide was divided in nine separate areas, as shown in Figure 5.3.2. The maximum, minimum and average lengths of trees within each area are shown in Table 5.2.1. Each tree was mapped as shown in Figure 5.3.1. For the distal zones, entire trees and fraction of trees were measured whenever possible. A total of 1,764 were mapped with recorded lengths and azimuths. Figure 5.3.4 shows a map of tree density per acre. The Figure clearly shows areas of greater density and supports the hypothesis of two separate sliding stages, discussed in this report. The density of trees in areas 3, 4 and 5 are likely from the first stage, whereas areas 1 and 2 contain the trees from what appears to be a monolithic drop of the upper block following removal of buttress support from the first sliding stage 1. An unusual concentration of trees (partial and whole) has accumulated in areas 8 and 9, which is interpreted to be a zone of compression or collision of blocks within the landslide mass. For each area, attribute values for the output tree features included the azimuth which is measured clockwise from due North. Those values are listed in Table 5.2.1.

Figure 5.3.5 shows rose diagrams of tree orientations for each area as delineated in Figure 5.3.2. These polar diagrams show the distribution of tree orientations in 5 degree angle bins. The length of each bin represents the number of trees within that particular orientation. The orientations are from top of tree to root base. Each rose diagram has a different horizontal scale for the number of trees. The rose diagrams for areas 1, 2 and 3 show the trees located between the headscarp and the displaced river. Areas 1 and 2 have the greatest number of trees, about 30% of the total, and they are oriented in a fairly narrow band roughly in the southeast direction. Area 3 has a similar overall orientation although there is more scatter and several trees point to the north. More than 65% of the trees were found on the south side of the Stillaguamish river. Immediately across the river to the south, the orientation in areas 4 and 5 are similar to that of north of the river. Closer observation of the high resolution photo shows that the northwest portion of area 4 appears to be a collision zone where some of the trees are more scattered. That zone, comprised of 74 trees, is shown on the rose diagram Figure indicating trees are scattered in

all directions. Further to the south, areas 6 to 10 point to a general northeast direction. Dispersion is also greater in those areas especially in area 9 where the trees likely spread on one side or the other of the hill. Areas 7 and 9 at the distal end account for more than 30 % of the trees with most of them denuded of branches. The overall dispersion of the trees from north to south may indicate that in the more hummocky areas, the trees are pointing in the direction of the failure while in areas with more mobility, due to greater saturation, the direction is predominantly to the northeast direction indicating that the trees were floating or pushed perpendicular to the orientation of the debris flow motion.

Figure 5.3.6 shows the azimuth for each area represented by a single red arrow. The azimuths indicate that south of the river, the trees are generally aligned to the east which suggests that those trees were floating atop a fluidized mud flow. This interpretation is supported by aerial photographs of those areas taken two days after the Oso Landslide occurred where clearly the greatest depth of water was found. The arrows point in the direction from top of tree to base. The tree lengths also decrease significantly towards the distal end of the slide mass and runout zone, as indicated in Table 5.2.1.

Differences in the size and orientation of trees reflect differences in pre-failure forest conditions on different parts of the slope, and differences in the orientation (average compass bearing) reflect differences in the behavior of different landslide zones. The size of trees in areas 1 to 5 are substantially greater than those in areas 6 to 10, reflecting the smaller size and greater amount of deciduous trees on the lower portions of the slope (i.e., the 2006 landslide deposit), and more mature conifers on the ancient landslide deposit and scarp. Differences in the average orientation of fallen trees in areas 1 to 3, which correspond to landslide Zones A and B, from those in areas 4 and 5, which correspond to landslide Zone E, indicate a different sense of motion for those portions of the landslide (and thus for Phase 1 and Phase 2 as discussed in Section 6). The tree orientations in areas 6 to 10, which correspond to landslide Zone F, are oriented roughly orthogonal to the flow direction.

Laboratory Testing

A series of index property tests were conducted on samples collected at the Oso landslide from various hand auger holes or from the ground surface. The field locations of these various samples are shown in Figure 5.2.1. Tests were carried out in accordance to ASTM standards (D2216 for moisture content, D4318 for Atterberg limits and C136 for sieve analyses). Testing was conducted approximately 1-2 weeks after the specimens were collected in the field. Table 5.3.2 summarizes the moisture contents and Atterberg limits for all specimens.

The Atterberg limit tests were performed using material passing the No. 40 sieve. Atterberg Limit tests were attempted on HA-7 but due to the lack of plasticity, the plastic and liquid limits could not be performed successfully. Specimen 2B (HA-11) also exhibited similar non-plastic properties in the plastic limit test. A liquid limit test conducted on HA-11 yielded a liquid limit of

17; however, liquid limits below 16 are not regarded as reliable since the soil tends to slide on the cup instead of flowing or shearing. Thus, although the liquid limit of 17 is borderline unreliable it does give insight into identifying HA-11 as SC. Figure 5.3.7 shows a photograph of a specimen of varved clay obtained on the East flank of the Oso landslide. The specimen split very easily along the silt varves providing a clear plane of weakness.

Sieve Analysis

Sieve analyses were carried out on all coarse grained samples. The results are shown in Table 5.3.2. Note that a proper grain size distribution should be completed using at least a 300 gram sample. In many cases, the specimens were less than 300 grams. Grain size distributions of all specimens can be seen in Figure 5.3.8. Photographs of the sieved material are shown in Figure 5.3.9.

Using the information available, the soils were classified according to the Unified Soil Classification System (USCS). Table 5.3.4 summarizes those classifications.

Table 5.3.2: Summary of Atterberg Limit Testing

Atterberg Limits					
Sample ID	PL (%)	LL (%)	PI (%)	Natural Water Content (%)	Comments
1A	31	75	44	41	
1B	27	60	33	87	
2A	26	55	29	24	
2B (HA-11)	-			16	Non-plastic
3A	26	28	2	33	Non-plastic
HA-2 (4.5-5.0 ft)	20	38	18	21	
HA-3 (1-3 ft)	29	43	15	30	
HA-4 (6-7 ft)	25	46	21	27	
HA-5 (7-7.5 ft)	28	36	8	29	Non-plastic
HA-6 (9.5-10 ft)	19	25	6	20	Non-plastic
HA-6 (12-12.5 ft)	21	44	24	20	
HA-7 (1 ft)	-			20	
JW-2	27	58	31	53	
JW-3	19	21	2	21	Non-plastic
JW-4	26	62	36	21	Top of Lacustrine

Table 5.3.3: Tabulated summary of sieve analysis results.

Sieve Analysis								
Sieve Size	Sieve Opening Size (mm)	Percent Passing						
		S1/S2	S3 (G4)	JW-3	3A	2B (HA-11)	HA-6 (9.5-10')	HA-7
#4	4.75	100.0	100.0	91.8	100.0	94.0	98.1	100.0
#10	2.00	100.0	100.0	84.6	100.0	91.4	97.3	100.0
#20	0.85	99.8	100.0	77.2	100.0	87.6	96.2	99.2
#40	0.425	99.8	100.0	69.8	98.4	79.6	95.1	99.2
#60	0.25	76.4	99.1	59.5	94.5	72.2	91.8	97.3
#100	0.15	23.5	77.6	46.3	91.0	62.2	86.2	94.6
#140	0.106	8.4	43.2	35.5	88.2	50.9	74.9	82.8
#200	0.075	8.2	34.8	30.8	83.9	46.4	64.9	57.1

Table 5.3.4 USCS Soil Classification

Sample ID	USCS Classification ¹
1A	CH
1B	CH
2A	CH
2B (HA-11)	non-plastic (likely SC)
3A	ML
HA-2 (4.5-5.0 ft)	CL
HA-3 (1-3 ft)	ML
HA-4 (6-7 ft)	CL
HA-5 (7-7.5 ft)	ML
HA-6 (9.5-10 ft)	CL-ML
HA-6 (12-12.5 ft)	CL
HA-7 (1 ft)	non-plastic
JW-2 (near surface)	CH
JW-3 (near surface)	SC-SM
JW-4 (1 ft)	CH
G2	CH
S1/S2	SP
S3(G4)	likely SC-SM

1. CL – clay, low plasticity; CH = clay, high plasticity; ML = silt, low plasticity; SP = poorly graded sand; SC = clayey sand.

Carbon dating

Three radiocarbon dates were obtained on samples of bark collected off of buried logs exposed in the eastern margin of the 2014 landslide (Table 5.3.5). Sample Oso 1 and Oso 2 were collected from an exposure on the lateral scarp in zone C and sample Oso 3 was collected from the lateral scarp in zone A. Radiocarbon ages of 5371 ± 28 BP, 5138 ± 27 BP, and 5304 ± 28 BP correspond to calibrated calendar year ranges of BC 4328-4070, BC 4033-3808, and BC 4232-4047.

Considered together these three calendar age ranges suggest that the landslide that killed and buried these trees occurred just over 6000 years ago.

Table 5.3.5 Radiocarbon dates for material collected from exposures in the eastern lateral scarp of the 2014 Oso landslide.

Direct AMS/GEER code	$\delta(^{13}\text{C})$	Fraction of Modern (per mil)	Radio-carbon age BP	Calendar age Cal BP (2s)	Species ^{1,2}
D-AMS 006490/Oso1	21.5	51.24 ± 0.18	5371 ± 28	BC 4328-4070	spruce
D-AMS 006491/Oso2	32.0	52.75 ± 0.18	5138 ± 27	BC 4033-3808	hemlock or D. fir
D-AMS 006492/Oso3	21.9	51.67 ± 0.18	5304 ± 28	BC 4232-4047	hemlock or D. fir

¹ Probable identification (E. Leopold, Univ. of Wash., pers. comm.)

² Spruce = *Picea sitchensis*; hemlock = *Tsuga mertensiana*; D. fir = young Douglas fir, *Pseudotsuga menziesii*.

Given the position of the exposures these samples were collected from, we interpret these dates as recording the timing of the ancient Headache Creek landslide, which Haugerud (2014) assigned to his morphologic age class D, the oldest of those he mapped in the valley. Thus, assuming that Haugerud's (2014) mapping of about 15 large landslides in 4 distinct generations shows all the slides from the past 6000 years, we can estimate recurrence intervals of roughly 400 to 1,500 years for large landslides in the vicinity of the Oso Landslide.

5.4 Seismic Signals Generated by the Landslide

The Oso Landslide generated ground vibrations that were well recorded by several seismic stations located in western Washington. Allstadt et al. (2014) performed an initial assessment of these recordings and found two distinct episodes of landsliding separated by a short period of relative quiescence. The first episode of landsliding initiated on 22 March 2014 at 10:37:22 a.m. local time (17:37:22 UTC). Records from Snohomish County Emergency Services indicate that the first emergency telephone calls were received by the agency about 7 minutes later at 10:44 a.m. The second distinct episode of landsliding began at 10:41:53 a.m. In the one-hour period that followed at least 10 low-amplitude seismic signals were detected in the recordings. Allstadt et al. (2014) performed an initial review of seismic station data for the days preceding the Oso Landslide and found no indication of precursory activity. They additionally reviewed Pacific

Northwest Seismic Network records for evidence of earthquake activity in the weeks leading up to the landslide, but aside from a single small magnitude event (M 1.1), no significant seismic activity was found. A magnitude 1.1 earthquake is too small to trigger a landslide and therefore it is highly unlikely that the Oso Landslide had a seismic trigger.

Figure 5.4.1 shows vertical velocity-time histories recorded at the three closest seismic stations to the Oso Landslide. These stations, designated as JCW, B05D, and CMW, are located at distances of approximately 10, 17, and 22 km, respectively, from the landslide. As noted by Allstadt et al. (2014), two distinct episodes of major landsliding are apparent (the time scale was selected to highlight the major episodes; the smaller events that occurred over the following hour are not shown in Fig. 5.4.1). Figure 5.4.2 shows the same data plotted as smoothed, high-pass filtered (<1 Hz) envelopes (i.e., as "stacked" amplitudes) of velocity. This alternative plotting format facilitates a clearer visual interpretation of the high frequency portion of the seismic recording. The high frequency component of landslide-generated seismic signals has been attributed to momentum exchanges resulting from flow over smaller-scale topographic features, frictional processes, and impacts of individual blocks (e.g., Allstadt, 2013). Owing to the smoothing function, the velocity amplitude data (vertical axis) should be regarded as relative rather than absolute. Similarities in the general shapes and relative amplitude of the signals suggest that they largely reflect landslide dynamic rather than wave travel path effects.

The enveloped seismograms are revealing and include several features that are worth highlighting. The shape of the envelope (Figure 5.4.2) for Episode 1 is similar to that recorded for flow-type events (e.g., Surinach et al., 2005). The initial portion of the signal gradually rises in intensity over a ~30 s period. This is followed by a ~30 second intermediate period of varying high amplitude motion. In the third and final portion, motion slowly diminishes (~65 s) and eventually approaches background noise. These three phases are understood to represent progressive initiation, propagation, and deposition of flow-type landslides (Bottelin et al. 2014). The timing of the peak amplitude of motion corresponds to the period when the largest landslide mass is in motion (Dammeier et al. 2011).

The initial portion of the envelope for Episode 2 is steep, which suggests a relatively rapid onset of movement (10 s). This markedly contrasts with the slower and more emergent initiation in the preceding Episode 1. Several distinct high-amplitude spikes punctuate the main portion of the signal. These spikes may represent termination impacts of large masses within a landslide rather than flow-type phenomena (Hilbert et al. 2014). The final portion of the signal quickly decays indicating an abrupt end to landslide movement approximately 70 s after the onset of Episode 2 movement.

While peak amplitudes are somewhat similar for the two episodes, the duration of high amplitude motion is significantly less for the second episode. Dammeier et al. (2011) have demonstrated a strong correlation between duration of seismic signal and the volume of the landslide generating the ground vibration. While this suggests that the volume of material involved with the second

episode was substantially less than that of the first episode, substantial differences in the style of landslide movement (e.g., debris flow versus extensional translation) could also affect the duration and style of the seismic signal.

5.5 Eyewitness Accounts

The Oso Landslide occurred on a Saturday morning when a majority of community residents were at home. Media accounts indicate that 58 people were situated within the inundation zone when the landslide occurred. Of these, 15 individuals survived the debris flow and were rescued. It is reported that 13 community residents were away from their homes at the time of the landslide. Several of the landslide survivors as well as other individuals who were present but located outside of the inundation zone provided observations and recollections of the event to the media. Table 5.5.1 summarizes key aspects of these accounts that pertain directly to the landslide. Owing to the sensitive nature of disaster, the accounts have been anonymized to protect the identity and privacy of eyewitnesses. In addition to collecting eyewitness accounts from the media, members of the GEER team spoke to at least a dozen individuals who were on site shortly after the landslide occurred. Although these post-event accounts cannot describe the landslide event itself, they do support the eyewitness reports of conditions that existed immediately following the event.

Eyewitness accounts vary depending on the individuals' location and vantage point. For example, recollections of individuals located on the valley floor tend to focus on the debris flow, while that of a witness on the north side of the Stillaguamish River recounts the failure of the hillslope. Nevertheless, there are a number of common themes that are repeated in the accounts. These include recollection of:

1. Extraordinary noise (often described as a plane crash or a freight train) and additionally the sound of crashing and breaking from the debris flow (e.g., that of "trees breaking");
2. Rapid inundation by a tall ("above roof lines of homes"), fast-moving, and highly liquid debris flow mass; and
3. Soft and "quicksand-like" condition of the saturated debris flow deposits immediately following the landslide.

Aside from these common themes, there are two specific recollections from eyewitnesses that are worth highlighting because of how they relate to the seismic recordings and other observations:

1. Observation that "half" of the hillslope (i.e., in the source zone) initially "broke away" and surged toward the Stillaguamish River;

2. Reported period of relative quiescence between an initial stage of landsliding (estimated to be 1.5 minutes by eyewitness) and a later mass movement.

Interestingly, several survivors reported that despite the high velocity of the debris flow, sufficient time existed to gather and place on shoes and to alert other household members of the impending debris flow. This is commensurate with the long travel distance of the debris flow.

Finally, an area resident was quoted in an April 3, 2014 Seattle Times story that she and her husband had noticed a change in the bluff above the river in the weeks before it slid. She described how a crack was widening at the top of the slope: "It was just sliding down a little. It wasn't a lot, but we could see that it was opening up."

Table 5.5.1 Summary of Eyewitness Accounts

Eyewitness	Location	Summary of Account	Reference
1	Edge of eastern debris runout zone	<p>Eyewitness heard tremendous rumbling and snapping; looked up and saw Douglas firs falling and breaking and splashes of water shooting up through the woods (within Oso Valley). Mud and limbs raced up driveway in waves.</p> <p>Eyewitness saw trees falling as a mudslide rushed toward the house. "It looked like the trees were just sinking into the ground — that's how fast they were falling. I turned and looked and saw a bunch of water splash up and a bunch of mist. I saw some water going over (Highway) 530."</p> <p>"The water (in the debris field) was only maybe two inches deep, but the ground was so saturated my leg went all the way down to my knee. The sound was like if you were to take a thousand people and had them hold boards and break them over and over again. That's what it sounded like."</p>	Seattle Times, 29 March 2014, and Everett Herald 26 March 2014
2	Edge of eastern debris runout zone	<p>"The noise was awful, it was the sound of tens of thousands of things hitting each other."</p> <p>Eyewitness saw a river of "wet earth" crashing towards home. They placed on boots and then evacuated.</p> <p>"Those trees (in debris) must have come from almost a mile away".</p> <p>Stepping into fresh landslide deposit, eyewitness sank to their waste.</p>	Seattle Times, 22 and 29 March 2014
3	Eastern debris runout zone	<p>Eyewitness "heard a cracking." Through the window they saw "mud, 25 feet high, coming." The wave crashed into the house and sent both occupants tumbling, the slurry caking their nostrils and mouths.</p> <p>"The roar of the hillside collapsing was so loud that they thought an airplane had crashed.</p>	Seattle Times, 29 March 2014

		<p>Looking out the window, they saw a wall of mud racing across the valley. Like a wave hit our mobile home and pushed it up.. It tore the roof off of the house. When we stopped moving we were full of mud everywhere. (It lasted) two minutes." The wall of mud hit their home, engulfing him/her and a companion. They were able to swim to the surface and clung to the unattached roof before more water came in.</p> <p>Eyewitness looked out a window and saw half of a ... foothill break away and surge across the North Fork of the Stillaguamish River toward her house on the opposite bank...A wall of mud estimated to be 25 feet high crashed through the home, taking both occupants with it. "Then it hit and we were rolling, the house was in sticks. We were buried under things and we dug ourselves out."</p>	
4	West flank of landslide on the north side of the Stillaguamish River	<p>Eyewitness was in the front yard of their house on the north side of the Stillaguamish River when they heard a loud, prolonged scraping and noticed the brief fluttering of treetops on the lower bench of Mount Higgins. "The noise sounded like a 747 (airplane) about to crash. It lasted about a minute and a half. It was loud" "When (the landslide) hit the water, it shot way up, way taller than the tallest trees. Then I saw this big black wall — it must have been more than 100 feet high — rise high above the (Steelhead Drive) neighborhood. The houses, in comparison, looked minuscule. It was unbelievable."</p> <p>Eyewitness reports that when landslide hit the river, it accelerated. They also report a period of relative quiescence between initiation and subsequent runout.</p>	Seattle times, 27 May 2014
5	North side of the Stillaguamish River	<p>Eyewitness recalls noise as "loud, like the double-bladed Huey helicopters that occasionally log in the area. It sounded like the engine was just shredding, so my first thought was it was a plane crash or one of those helicopters hauling out a log and he's going to crash into my barn."</p>	Seattle times, 27 May 2014

6	Western debris runout zone	Eyewitness heard a "terrifying noise, then their house began to shake and they witnessed neighboring houses "exploding." When they saw the wave of mud and debris heading their way, they held their infant child. Both became entrained in debris and were carried an estimated 700 feet by the runout. During this time it felt as the debris was moving "superfast but it felt like forever" Debris was a "thick river of mud."	Everett Herald, 9 April 2014 and video footage from KOMO posted 10 April 2014.
7	Western debris runout zone	"I heard this horrible noise," it sounds like a freight train. I opened up the bathroom window and I looked out and it looked like the ground was shooting up." "Being upstairs (in our home), I think that gave us a chance"	Everett Herald, 20 April 2014
8	Motorist on Highway 530	Landslide debris moved fast, coming across the road in (an estimated) 3 seconds.	Video footage
9	Debris runout zone	Eyewitness sank up to their armpits in debris deposits (estimated to be 30 minutes after landslide)	Seattle Times, 29 March 2014

Note: Owing to the sensitive nature of the reports, we have anonymized these accounts. As noted in the table, a majority of these accounts were reported in the local media.

5.6 Impacts on the built environment

The Oso Landslide completely destroyed the Steelhead Haven neighborhood and additionally damaged or destroyed many homes located along State Highway 530. Most of the damaged or destroyed residential structures were removed or otherwise altered by the search, rescue, and recovery efforts of March and April 2014, and therefore the GEER team was not able to make direct observations of the condition of buildings after the landslide. Nevertheless, it is clear from eyewitness reports and post-event photos and video that most structures failed quickly and catastrophically. This is not surprising considering the high velocity and significant height of the debris flow, and the amount of debris (most notably trees) that was entrained in the mass. A significant majority of the building debris was found within approximately 100 m (330 ft) of the distal edge of the debris flow deposit. Debris trajectory maps indicate that debris was often carried across distances exceeding 200 meters (650 ft) (see Figure 5.2.36). These trajectory maps show a clear east-west bifurcation near the middle of the debris deposits.

Although a majority of homes were completely destroyed, there are at least two reports of Steelhead Haven residents who survived the debris flow in their residences. In the first account, two individuals (Eyewitness 7, Table 5.5.1) attribute their survival to their location on the second floor of a home whose first level was directly impacted the debris flow. In the second account, two individuals survived in a mobile home that appears to have been partially carried (rather than destroyed) by the debris flow. Remarkably, two survivors who became entrained in the debris were found 65 m (215 feet) from their home.

The landslide inundated a 600 m (2,000 ft) portion of Highway 530. It is reported that at least one fatality occurred to a motorist whose car was impacted by the debris flow. Motorists in at least 3 other vehicles saw the debris flow traveling towards the highway and were able to avoid impact by immediately stopping their cars. Despite the debris flow and deposition, the roadway surface itself remained largely intact. Exceptions were found near the middle of the debris field, where two pavement sections (150-m-long and 50-m-long, see Figure 5.2.36) were uplifted and carried in pieces to the south side of the road (Figure 5.2.35). These sections of pavement uplift came from the section of the road that was elevated as an embankment. The thickness of the debris flow deposits on the road varied with location but differencing the elevations on the 2013 and 2014 lidar datasets for locations along Highway 530 revealed that net deposition of up to just over 6 m. Debris flow deposits were excavated from the road surface (with a relatively shallow 4h:1v slide slope) in April 2014, and the road was reopened at a reduced speed on 31 May 2014. Even then, more than two months after the landslide, the 4h:1v slopes reveal pockets of up to several meters in each direction that are too wet and soft to support a persons' weight.

Figure 5.2.1 Locations of key observations of GEER team during site reconnaissance.





Figure 5.2.2. Seeps along western (right) margin of the landslide. Photo credit Eric Jensen, King County Sheriff Department, photo date 3/24/2014.

Figure 5.2.3: Interpreted landslide zone map.

94





Figure 5.2.4 Photograph of Zone A1, recessional outwash and gray glacial till exposed in landslide headscarp.

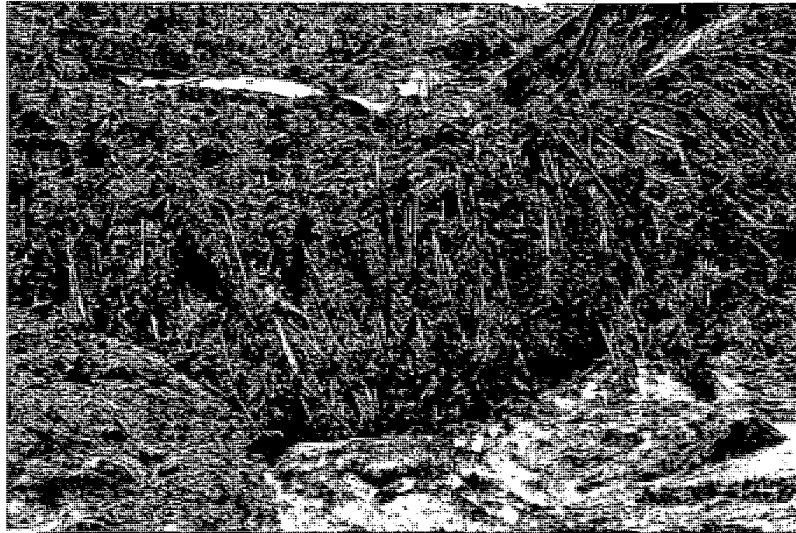


Figure 5.2.5a: Photograph of Zone A2 as seen from top of landslide headscarp; view to south. Note uniform back-rotation of trees and onlap of gray till fragments of Zone A4 from scarp-face failure at left.



Figure 5.2.5b: Photograph of Zone A2 as seen from top of landslide headscarp; view to southwest. Note the topographic depression between Zone A2 (covered by downed trees) and Zone A1 (base of headscarp at right).



Figure 5.2.6 Onlap of gray till in Zone A4 over eastern portion of the downed-tree-covered slump block of Zone A2 (back-rotated slump block); view east from 48.27073, -121.84038.



Figure 5.2.7 Photograph of the eastern margin of Zone A; view toward northeast. Note exposure of in-place till (gray at left) with steep contact (prehistoric landslide scarp) running from upper left corner of photo to lower middle. Sandy oxidized talus in middle and upper right buries log sampled for 14C dating (see Table 5.3.1, sample Oso3).



Figure 5.2.8 Rotational block field of Zone B seen from the air looking west. Photo credit Eric Jensen, King County Sheriff Department, photo date 3/24/2014.



Figure 5.2.9: Zone B slickensides in lacustrine clay.



Figure 5.2.10a. Oblique view of two approximately 100-ft-long (30 m) fallen trees (near the center of the image) that have been dragged downslope after they were felled. They indicate the extension in this part of the slide mass. Photo by Eric Jensen, King County Sheriff Department, photo date 3/24/2014.



Figure 5.2.10b. Aerial view of indicator trees showing trails at least (45 m) 150 ft long showing skid marks from dragging. Location 48.28332, -121.84838. Aerial image dated 3/24/14 was provided by WSDOT GeoMetrix Office.



Figure 5.2.10c. pair of track-like impressions in the loose sand indicate that the log impacted violently and bounced before coming to rest. Photo taken by GEER on May 24, 2014. Camera position: 48.281458°N, 121.848316°W, view south.

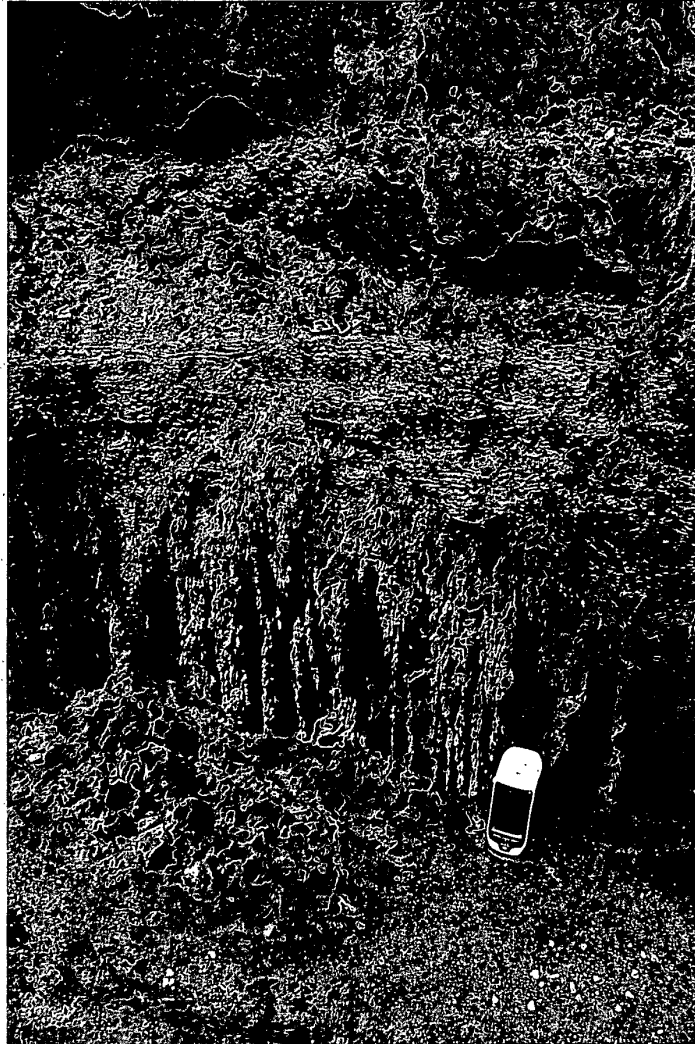


Figure 5.2.11: Lacustrine sediment exposed in western lateral margin in Zone B. Note flow structures running down from seeps in the outcrop face.



Figure 5.2.12 View looking northeast at sand ejecta deposits in Zone B near the Zone C interface. Camera position: 48.28238, -121.84391.

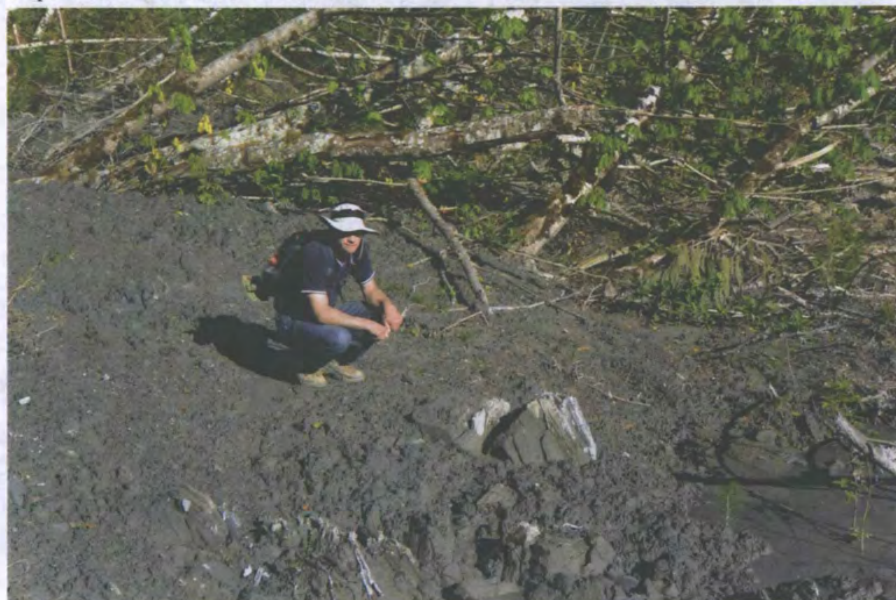


Figure 5.2.13A Liquefied lacustrine sediments in Zone C. Note rafted block of material set in flow matrix.

Figure 5.2.13B Map showing locations where several actively flowing seeps along the eastern margin of the landslide correspond to the uppermost areas of Zone C.

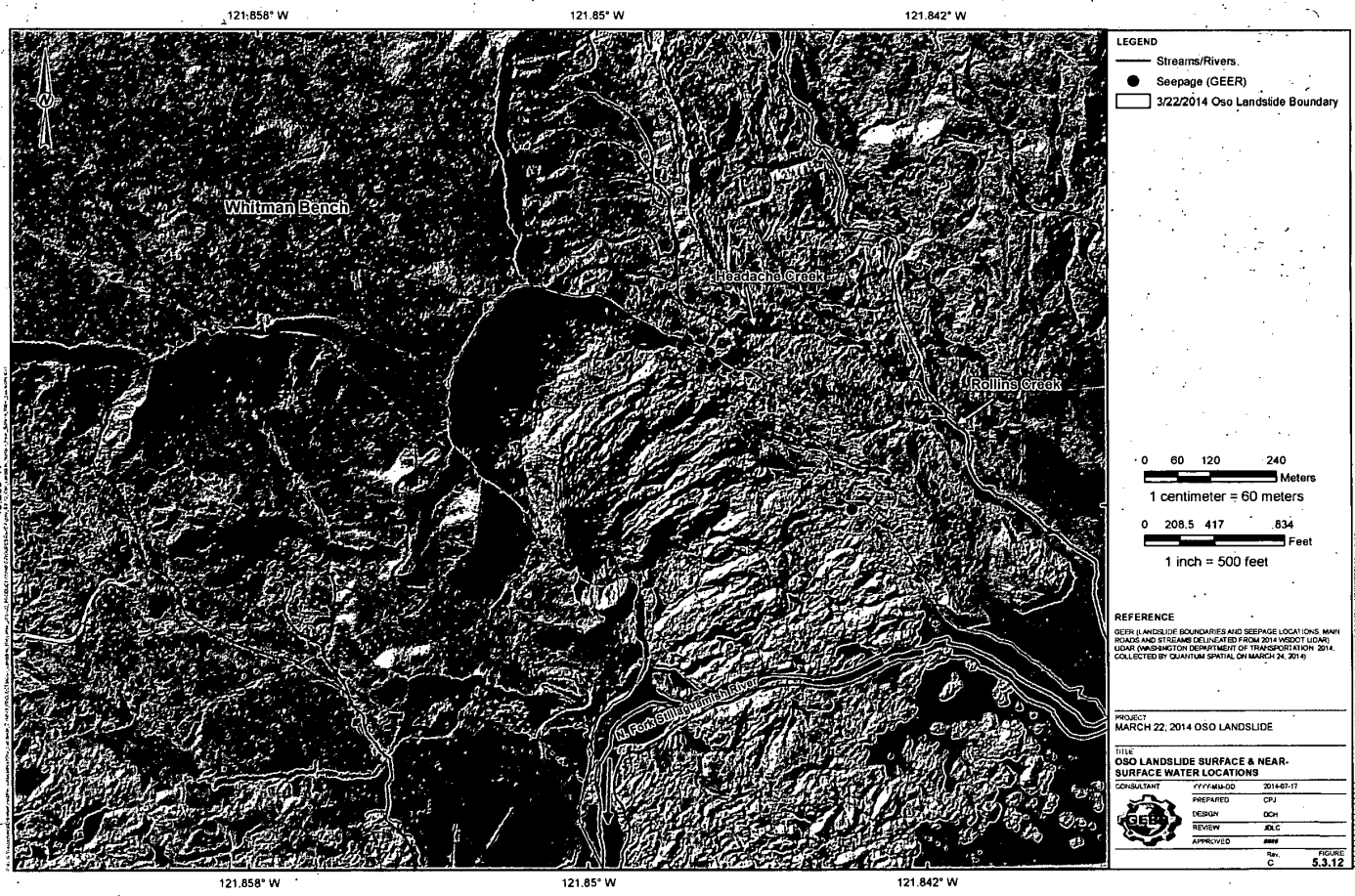




Figure 5.2.14 Seepage and piping near interface between Advance Outwash sand overlying Glacial Lacustrine clay. Location: N 48°17.124' W 121°50.827'; view looking east.



Figure 5.2.15: Hand auger boring (HA-3) into lacustrine material on the northern margin of Zone D. Camera location: 48.28118, -121.84519; view to northeast.



Figure 5.2.16: Southern margin of Zone D (gray on left) overriding northern trailing margin of Zone E debris (brown on right); view is to the east.



Figure 5.2.17. View west at loose and sloughing channel slopes in glacial lacustrine deposits within the landslide in Zone D. Camera position: 48.28026, -121.84339.



Figure 5.2.18 Preserved areas of intact forest floor in Zone E.



Figure 5.2.19 Tilted subvertical trees in Zone E.



Figure 5.2.20 Tumbled and broken trees in the impact zone between Stage 1 and Stage 2. Camera position: 48.27897, -121.84609.



Figure 5.2.21 Typical gray veneer that appears to be a splash deposit. Head of rock hammer in bottom center for scale. Camera position: 48.27903, -121.84611.



Figure 5.2.22 Gravelly and sandy silt veneer. Visible here on a remnant of the forest floor in the foreground, on a fallen tree towards the left of the photo, and coating the sandy bank of the basin in the background. This veneer-ringed basin appears to open only to the south, indicating flow to the north and thus a splash-back or flow reversal in the debris flow runout zone (i.e., from Zone F). Camera position: 48.27735, -121.84674, view south.



Figure 5.2.23 Sub-vertical tree rafted into current location near HA-10. Camera position: 48.27503, -121.84315, view northeast.



Figure 5.2.24 View from north end of Zone F toward rafted deciduous trees in Zone E, in background. Camera position: 48.27781, -121.83851.



Figure 5.2.25 Maple trees north of SR 530 that appear to be in place. Camera position: 48.27521, -121.84814.



Figure 5.2.26 Typical sand ejecta deposit. Camera position: 48.27849, -121.84406.



Figure 5.2.27 Typical sand boil. Location: 48.27616, -121.84686.



Figure 5.2.28 Recreational vehicle (RV) at the distal edge of the flow. Image shows damage to its side by a root-wad that is still present beside the vehicle. There is little evidence of earth debris: the RV was pushed and damaged by woody debris, as if carried by a flood. Camera position: 48.27528, -121.84160.



Figure 5.2.29 Vehicle wrapped around tree as if pushed from the southwest. The landslide source area is to the northwest and is visible in the background. Camera position: 48.27871, -121.83420.



Figure 5.2.30 Log that formed part of the log revetment constructed after the 2006 landslide and found in distal portion of Zone F (note steel cables). Photo taken on May 23, 2014; Camera position: 48.27912°N, 121.83592°W, view toward the northeast.



Figure 5.2.31 Revetment logs with metal identification tags and drilled holes with steel cables being examined by GEER team members on May 23, 2014. Camera location: 48.27737°N, 121.83876°W, view toward the north from SR530.



Date & Time: Sun May 25 12:00:49 PDT 2014
 Position: +048.27580 / -121.84255
 Altitude: 93m
 Azimuth/Bearing: 061 N61E 1084mils (True)
 Elevation Angle: -15.6
 Horizon Angle: -01.4
 Zoom: 1X

Figure 5.2.32 Asphalt with intact base course from SR 530 road bed plucked and transported by the debris flow. Note piece of asphalt in lower right with yellow paint stripe. Camera position: 48.27580°N, 121.84255°W, view to the northeast.



Date & Time: Sun May 25 12:27:13 PDT 2014
 Position: +048.27572 / -121.84240
 Altitude: 92m
 Azimuth/Bearing: 072 N72E 1280mils (True)
 Elevation Angle: -19.9
 Horizon Angle: +00.2
 Zoom: 1X

Figure 5.2.33 Drainage pipe and filter fabric from SR 530 transported to the southwest by initial debris flow. Camera position: 48.27572°N, 121.84240°W, view looking east-southeast.



Figure 5.2.34. Section of guard rail (top) and timber support (bottom) transported from SR 530 by initial debris flow. Camera positions: 48.27478°N, 121.84196°W, view toward southeast (top); 48.27481°N, 121.84217°W, view toward southeast (bottom).



Figure 5.2.35. (upper) Example of one of several Highway 530 pavement sections that were uplifted and transported by the landslide. The pavement section (which is inclined down to the left) shows an intact segment of what is believed to be the first material to have crossed the highway prior to its subsequent uplifting and transport. The scale shown is in feet (location: -121.842560, 48.275860). (lower) Close view of the deposit above the pavement section. The photograph shows a course-grained tan sand over a thin (several mm) film of grey silt and clay over the asphalt. The pavement is underlain by a gravelly pavement base course material that was emplaced during construction of the road. The structure of the tan sand deposit suggests initial arrival of a hyper-concentrated flow rather than a debris flow.

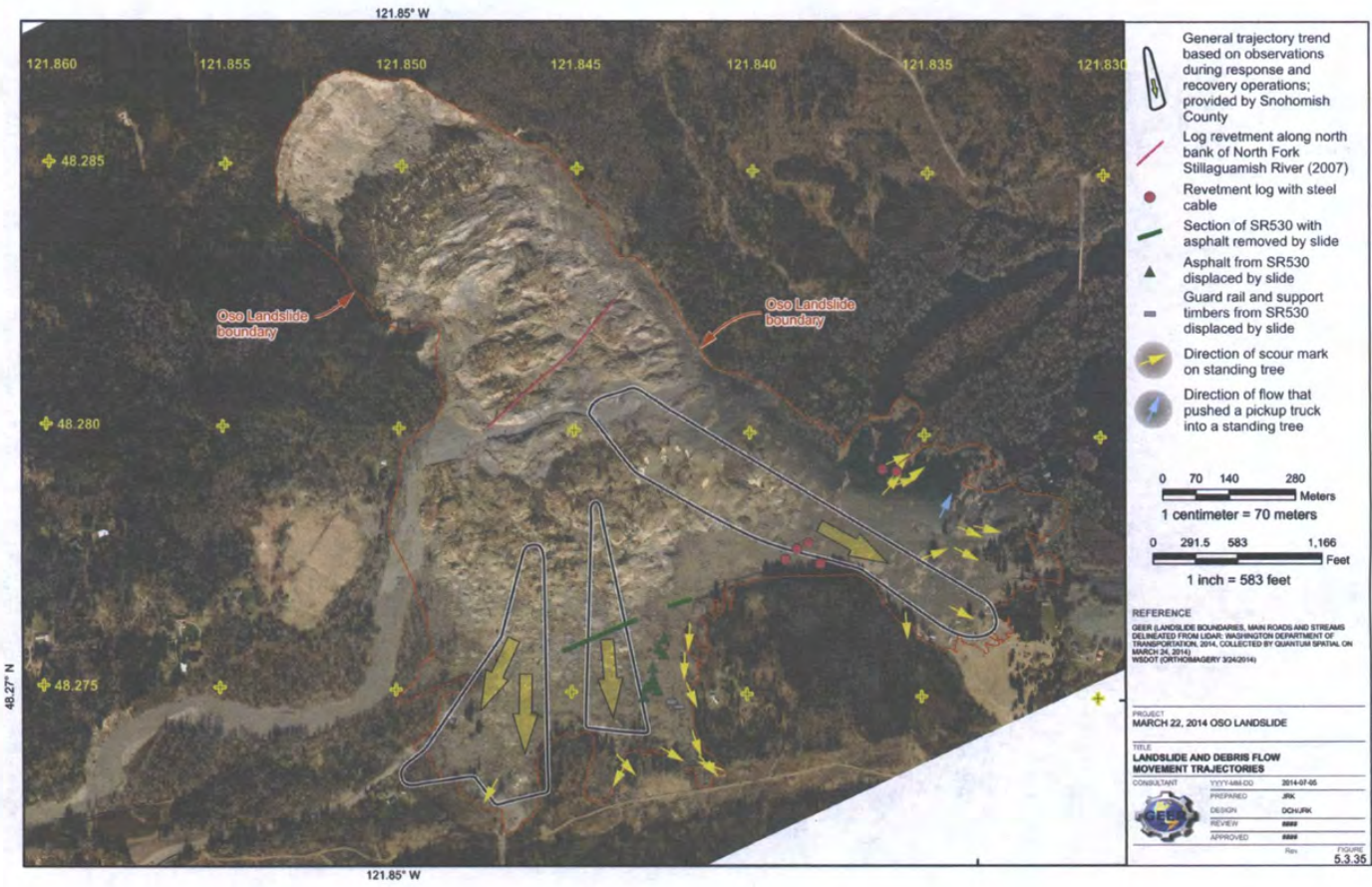


Figure 5.2.36 The travel vectors (vector from point of origin to depositional location) of identifiable materials.



Figure 5.3.1 Digitized trees and sections of trees within the landslide boundary



Figure 5.3.2 Areas used for evaluating tree density within landslide boundary

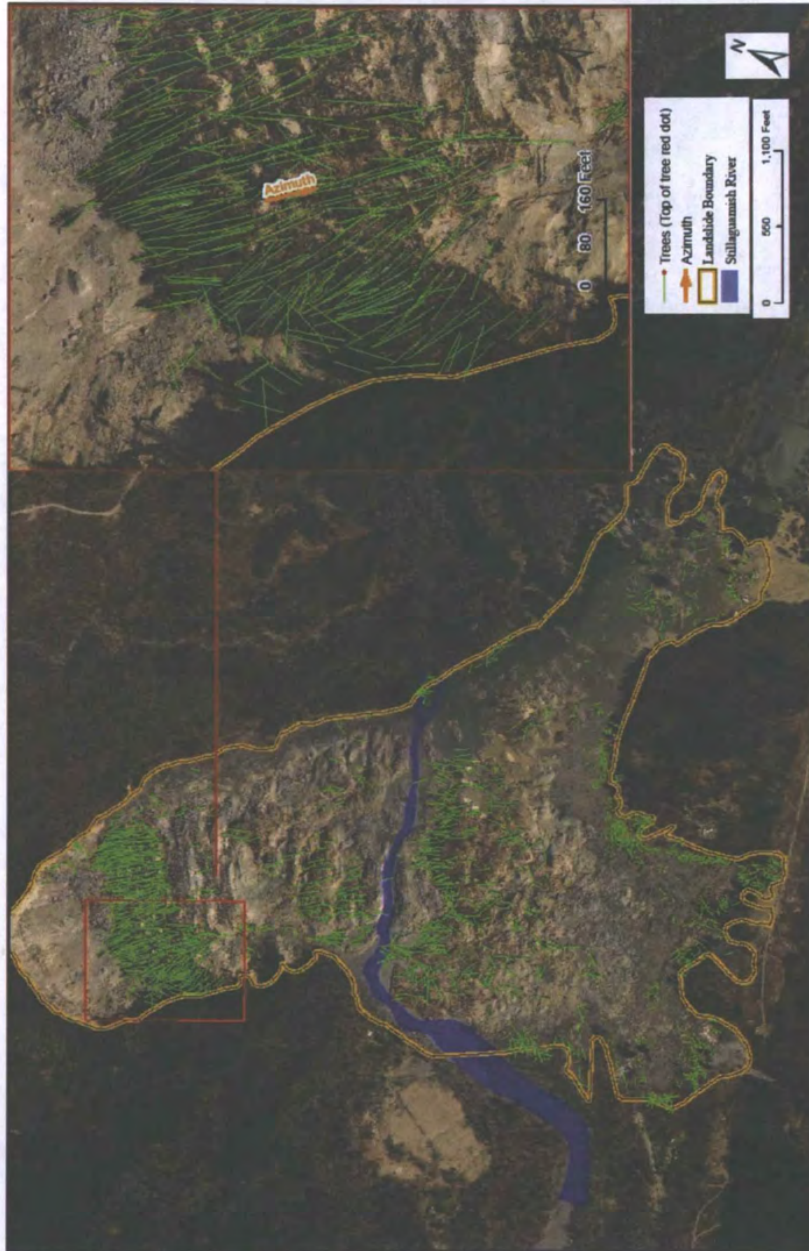


Figure 5.3.3 Example of tree density within area

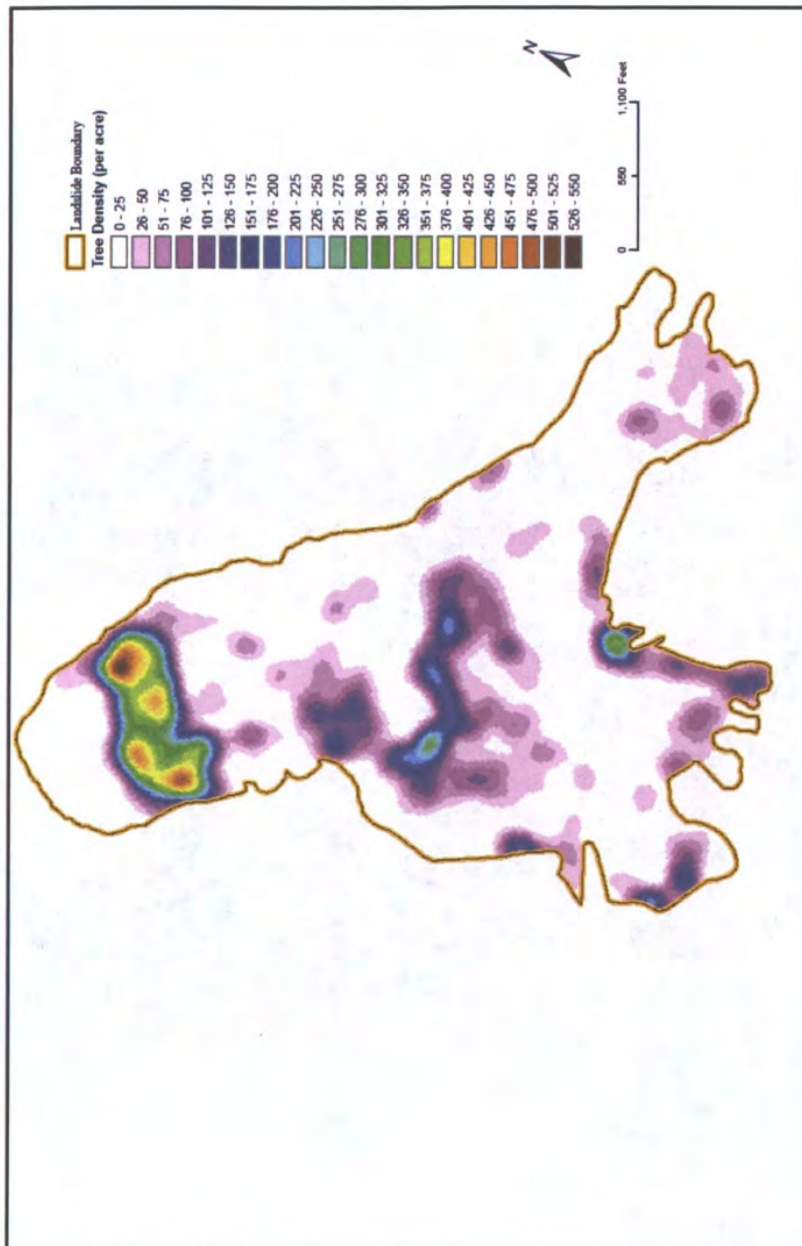
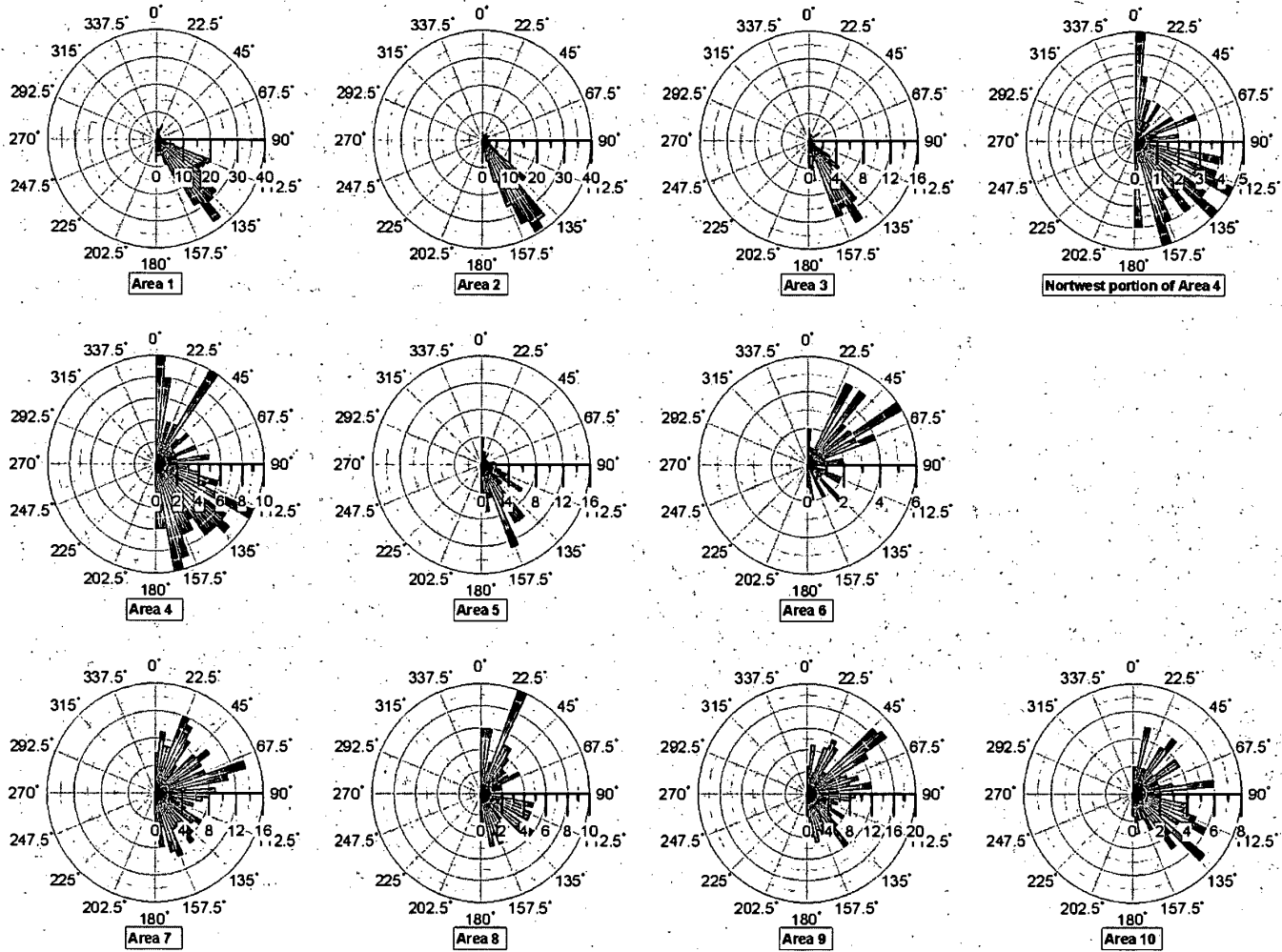


Figure 5.3.4 Tree density within landslide mass and runoff

Figure 5.3.5 Rose diagrams for each tree area shown in Figure 5.3.2.



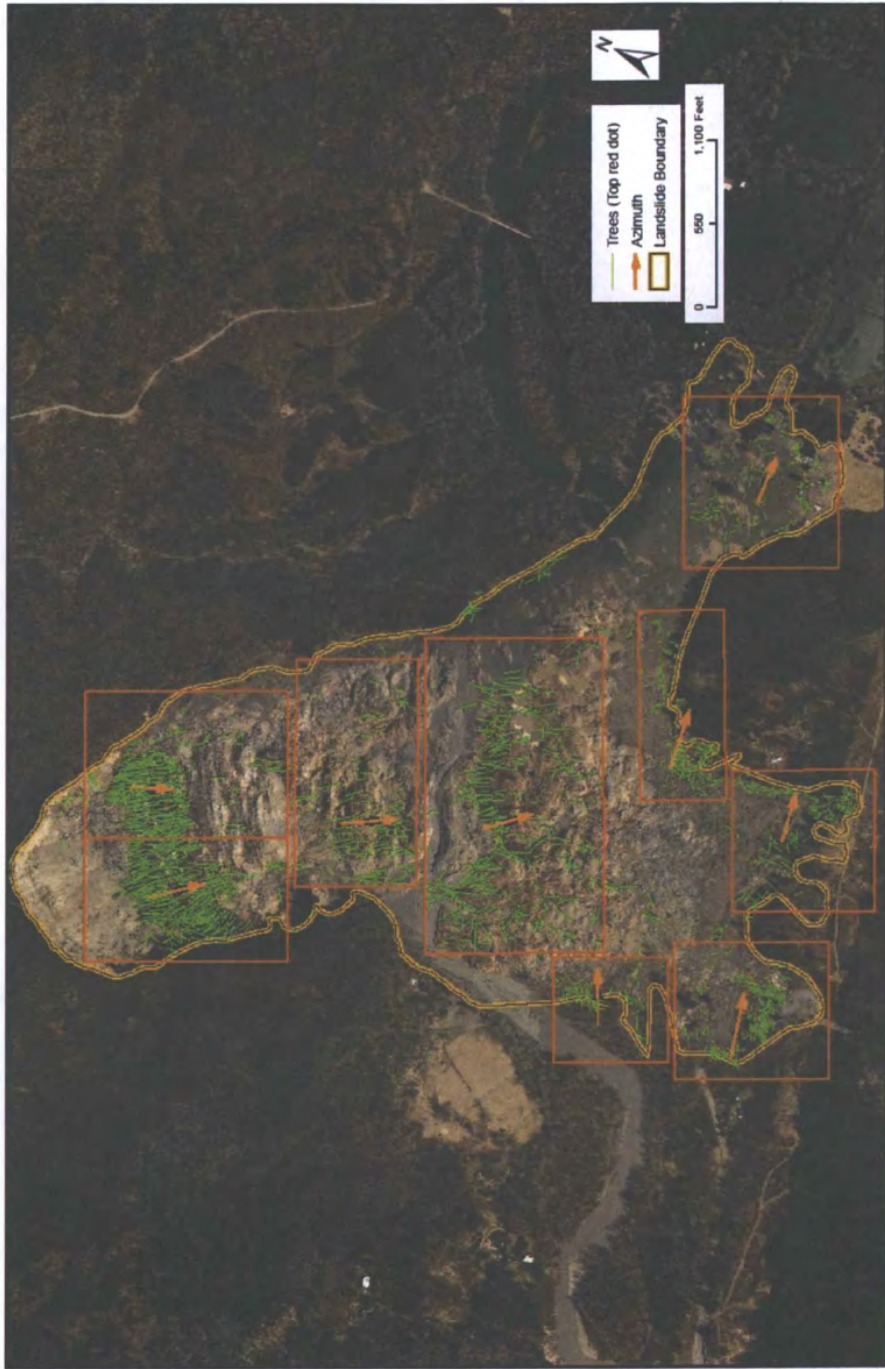


Figure 5.3.6 Average tree azimuths for each area.

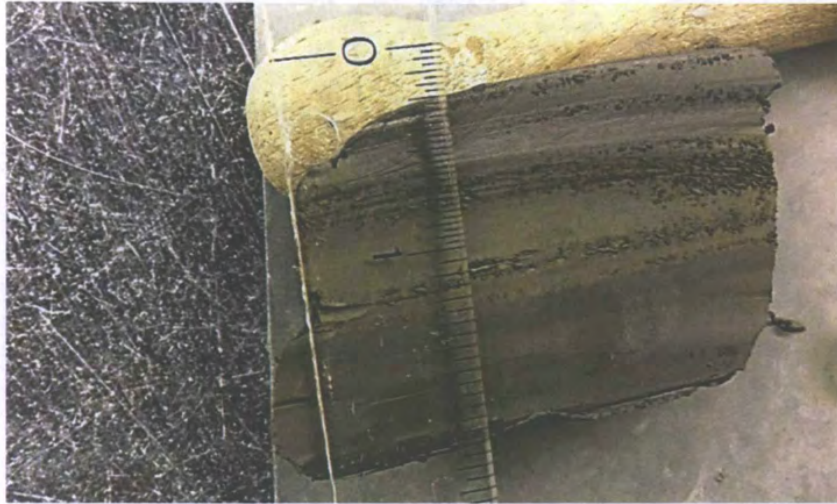


Figure 5.3.7: Varved clay test specimen.

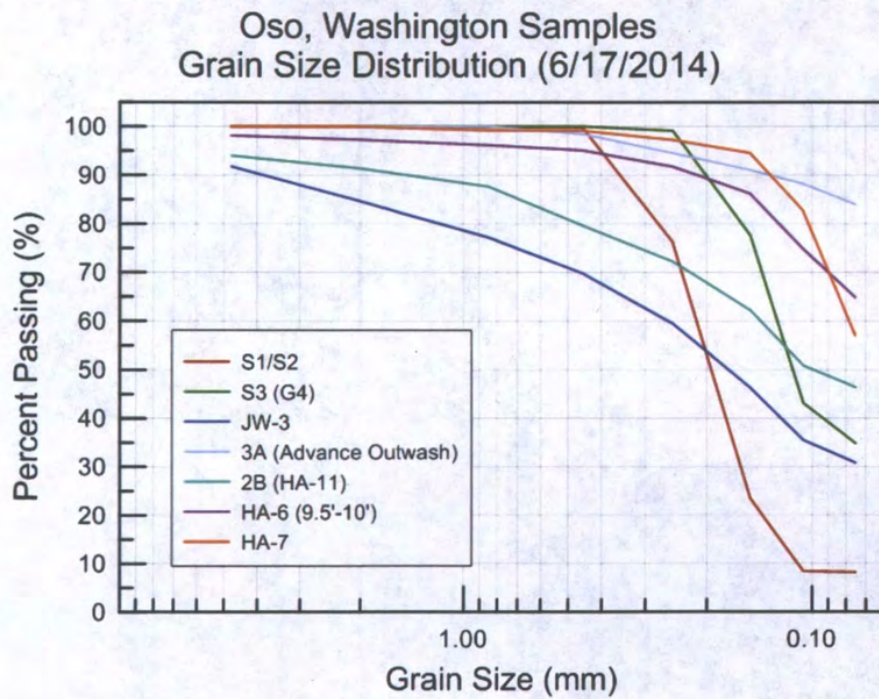


Figure 5.3.8 Grain size distribution plot for data in Table 5.4.2.

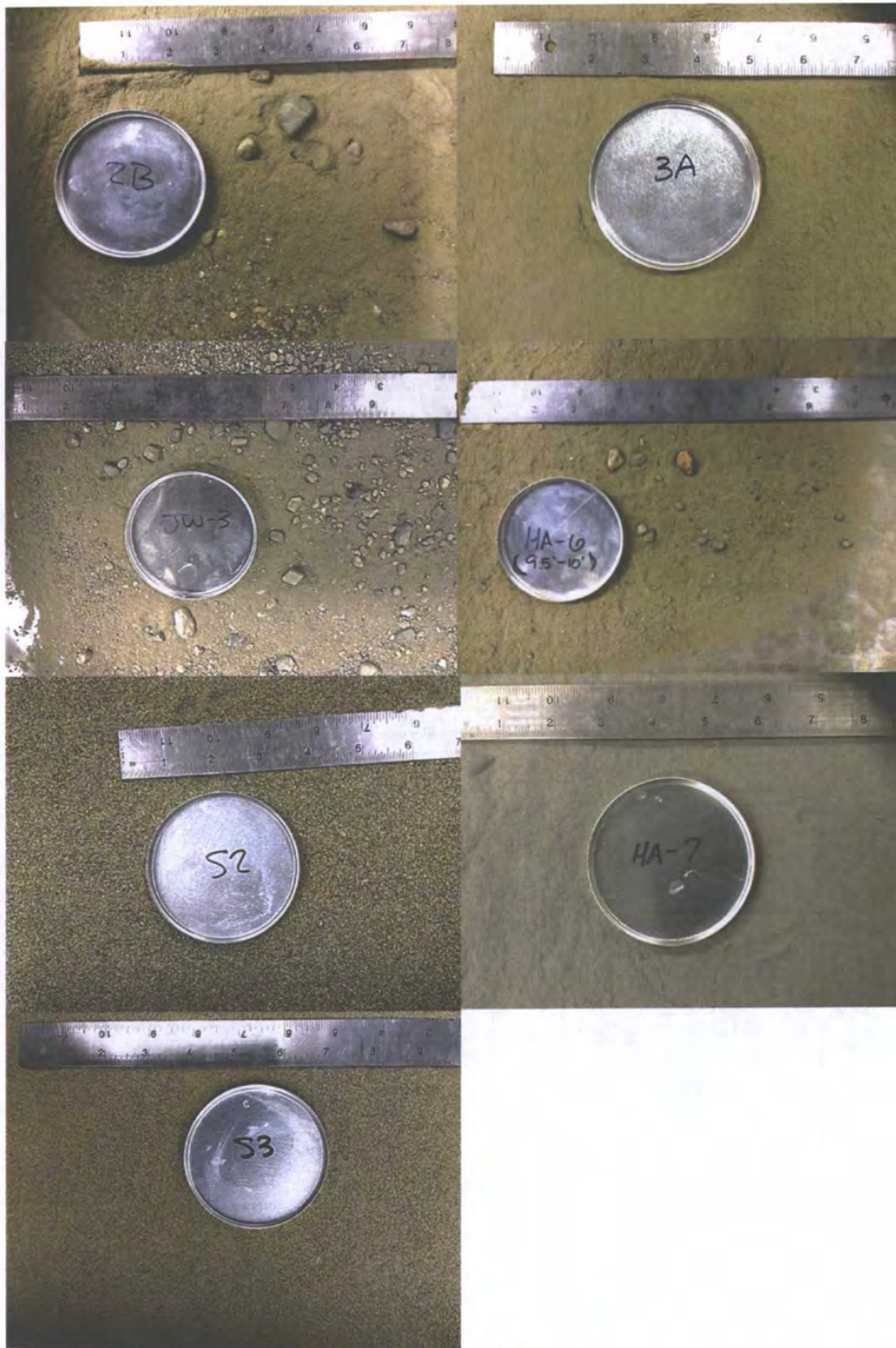


Figure 5.3.9 Photographs of dried and sieved specimens.

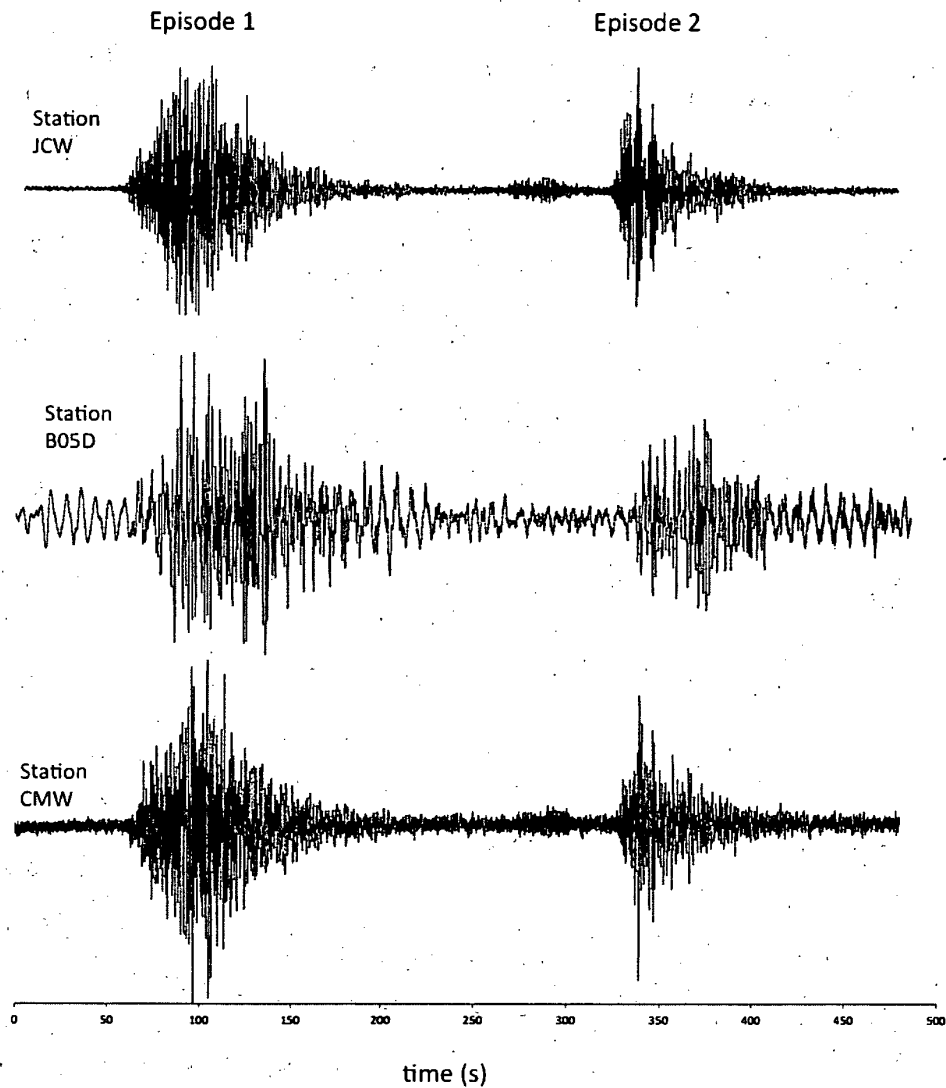


Figure 5.4.1 Velocity-time histories generated by the Oso Landslide. The signals were recorded at seismic stations located within approximately 22 km of the landslide site. A minor baseline correction was made to the signals, which are otherwise unmodified. Velocity values (vertical axis) have been normalized to facilitate a general comparison of the three signals; they are thus relative rather than absolute.

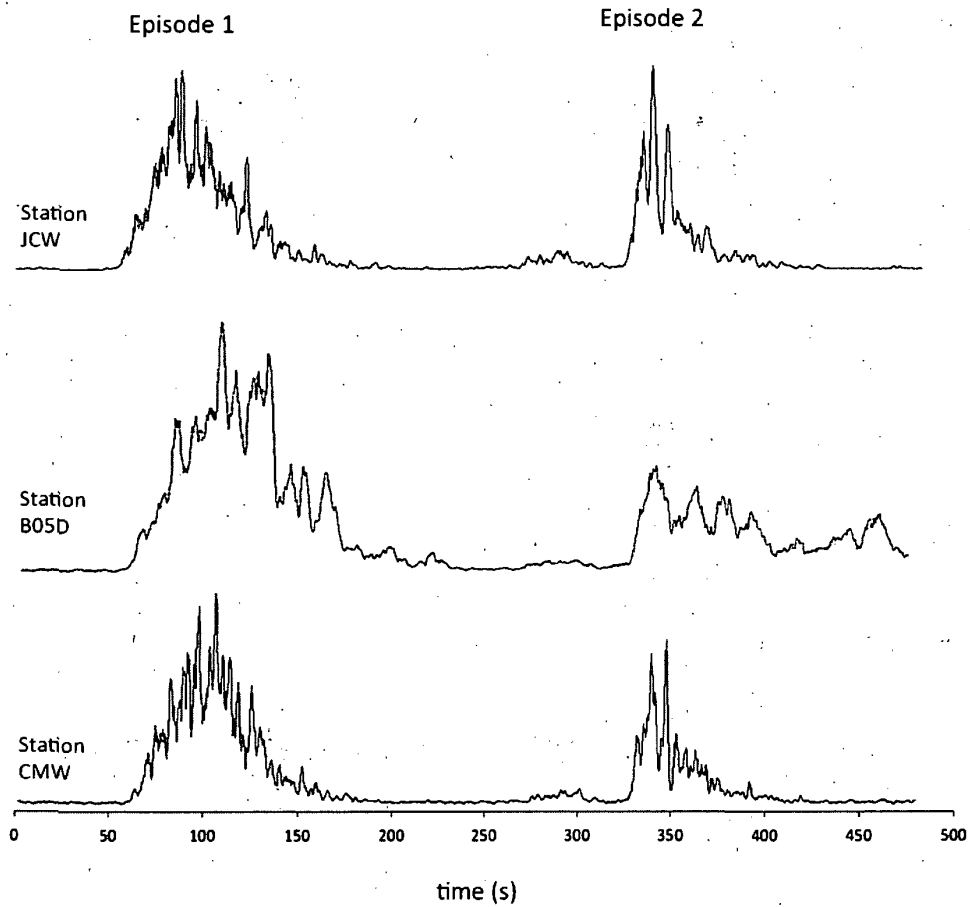


Figure 5.4.2: Landslide-generated velocity-time histories presented plotted as smoothed, high-pass filtered (<1 Hz), smoothed envelopes. Owing to the smoothing function, the velocity amplitude data (vertical axis) is relative rather than absolute.

6. HYPOTHESIZED MECHANISMS OF THE MARCH 22 LANDSLIDE

6.1 Introduction

The mechanism by which the Oso landslide failed may never be known with complete certainty because no eyewitness accounts or video recordings of the entire event exist and much of the structure of the landslide mass was altered by the large displacement and fluid nature of the failure. Moreover, no landslide monitoring instruments were in place and subsurface information prior to the slide was very limited, as summarized in Section 4.4. Nevertheless, the seismograph records are very important as they clearly indicate two major episodes of landsliding separated by a few minutes. They additionally show many smaller events within the hour that followed the main episodes (Section 5.5). The GEER field observations also support multiple stages of landsliding. The hypothesis of the landslide failure mechanics presented here is principally based on the reconnaissance observations and seismic recordings, as well as other findings presented in this report. It is well supported by the data presented in this report; nevertheless, it should be challenged and enhanced through future investigation, analysis, and monitoring.

The first major stage of movement (Stage 1) is interpreted to be a remobilization of the 2006 slide mass and a headward extension that included part of the forested slope of the pre-historic slide. As such, Stage 1 was comprised largely or entirely of previous landslide deposits, some as recent as 2006, and others ancient. It is believed that Stage 1 initiated partly on a shear surface that is essentially the lower portion of the ancient slide surface, as is shown schematically in Figure 6.1.1, and mobilized as a debris flow, traveling across the valley and causing most or all of the damage and destruction south of the river.

The second stage (Stage 2) occurred subsequently in response to the unloading (i.e., loss of "buttressing") and the redirection of principal stresses and possibly, to groundwater seepage forces. Stage 2 was a retrogression into the Whitman Bench of up to nearly 90 m (300 feet) horizontally from the ancient slide scarp. The Stage 2 slip surface probably joined the slip surface of Stage 1 (and that of the 2006 and ancient slides) at depth, but also included up to 300 m (1000 feet) or more of previously deeper in-place outwash, till and lacustrine deposits (Figure 6.1.1). The Stage 2 landslide moved rapidly on the existing Stage 1 slip surface until it essentially collided with the more intact blocks at the trailing edge of the Stage 1 slide mass, and came to rest. The seismic signals show several much smaller events in the time following Stage 1 and these are included as part of Stage 2 in the discussion that follows. Stages 1 and 2 are shown schematically in section in Figure 6.1.2, and in plan view in Figure 6.1.3.

6.2 Stage 1

Stage 1 is interpreted to mostly involve remobilization of slide debris that had also moved in the past; only this 2014 remobilization was far more dramatic and devastating than the previous mass movements within the landslide complex. Past slides on the slope and debris flows (along the

left margin) had on occasion dammed the river but had not mobilized with velocity and fluidity to travel hundreds of meters beyond the river. There are many possible explanations as to why the 2014 landslide was markedly different, and what contributed to it being so. These include the following:

1. Three weeks of extreme rainfall preceding the event. As described in Section 3, it is clear that the three weeks preceding the failure were exceptionally wet. Prior to these weeks in early March, however, the season had been relatively dry. It is well known that precipitation-induced landslides are often strongly influenced by antecedent (versus immediate) rainfall. In general, shallow-to-intermediate depth landslides (i.e., <~10 m deep) are typically influenced by days or weeks of wet weather, whereas large, deep landslides are responsive to longer periods (months or years) of wet weather. It is possible that Stage 1 was of a size that made it particularly sensitive to the three week period of high intensity precipitation, and this was sufficient to trigger movement. It is worth noting that no other landslides on natural slopes occurred in Snohomish County in March or April 2014.
2. Changes to groundwater recharge resulting from timber harvesting on Whitman Bench. As described in Section 2.4, the site has had a history of timber harvesting. The slope itself has not been logged since the 1950s, but Whitman Bench, which is a source area for groundwater that seeps towards the slope, has harvested tracts in various stages of growth. It is possible that in 2014, the location, size and maturity of growth in these tracts was such that groundwater discharge to the slope was greater in 2014 than in previous years when the slope had been stable or the landslides much smaller. The proximity of the logging activity to the landslide is shown in Figures 2.4.2A through 2.4.2F. Evaluating the effects of this activity on the 2014 landslide is beyond the scope of this report".
3. The elevation of the post-2006 slide debris being low enough to capture more of the groundwater from the Headache Creek basin. The 2006 landslide was larger than any in the previous decades and the drop of elevation near its head, as shown in Figure 4.1.5, could have caused a change to the local groundwater regime, essentially "capturing" (or drawing) some of the water that had previously fed the Headache Creek basin, and directing it instead toward the landslide. Seeps along this side of the slope were observed as shown in Figure 5.3.12 and suggest this was occurring to some extent.
4. The post-2006 landslide slope gradient was flatter than it had been previously. The flatter gradient makes natural surface drainage (runoff) of the slide mass less effective and thereby increases infiltration into the mass. As shown in Figures 4.1.5, 4.1.7 and 6.1.1, material was moved lower on the slope, indicating that either the mechanism or effect of the slide was rotation causing increased elevation near the toe and decrease near the head. This reduced surface gradient, along with the hummocky terrain provided by the sliding would be expected to decrease runoff and increase infiltration.

5. Static liquefaction¹ of the 2006 landslide mass. It is possible that the 2006 (and earlier) landslide deposits were loose enough to be susceptible to static liquefaction. The source material of these colluvial (landslide) deposits included recessional outwash, which has not been glacially consolidated and therefore is in a generally loose density state. This loose condition may have been further exacerbated by the 2006 and earlier mass movements, which would have served to further dilate (loosen) these materials. This idea is supported by reports following earlier slide activity (e.g., Thorsen 1969) that some of the colluvial materials on the slope were so loose that they could not support a person's weight. In addition to potentially dilating the deposits, prior landsliding at the site may have also increased static liquefaction susceptibility by increasing shear stresses within the earth mass. It is further noted that the fines (i.e., silt and clay) content of these predominately sandy colluvial materials (see laboratory classification results in Chapter 5) make them particularly vulnerable to static liquefaction (e.g., Papageorgiou et al. 1999). It is well recognized that loose materials subjected to the static shear stress states imposed by a slope can liquefy in response to even very minor increases (<5%) in shear stress (e.g., Kramer and Seed, 1988). For the Oso Landslide, such minor increases in shear stress could have resulted from any of several plausible mechanisms including: (i) changes in groundwater levels and/or seepage conditions due to antecedent rainfall and modifications to the groundwater regime (i.e., items 1-4 above), (ii) erosion of the landslide toe during to fluvial activity of the river, resulting in local stress concentrations, (iii) creep-induced encroachment of the upper portion of the slope onto the 2006 and earlier landslide deposits, and (iv) the cumulative effects of internal erosion and piping resulting in local stress concentrations.

6. Dilation and strain softening on the pre-existing shear surfaces and elsewhere in the glacial lacustrine unit. The glacial lacustrine deposits are in an overconsolidated state on the valley slopes because previous overburden from the glacier, till, and recessional outwash has either been completely removed (as in the case of the glacier), or partly removed, through valley erosion. When these overconsolidated materials are subjected to shear stress as imposed by the slope, they will dilate as they strain in response to the stress. Where the soil is saturated, as would be expected for most of this slope, water flows into the increasing voids that are created by the dilation. Thus, the soil becomes looser, and therefore weaker, while still subjected to the same shear stress. This positive feedback loop of shear strain, dilation and loosening (typically called softening in clay), can go on for years or decades, progressing from one part of a slope to another, before the overall slope becomes too weak to support itself, and fails.

7. Strength degradation toward residual values on pre-existing shear surfaces in the lacustrine deposits. Beds in the glacial lacustrine deposit were observed to vary from fine sand at the coarse and stronger end of the spectrum to high plasticity clay at the fine and weaker end of

¹ Liquefaction is defined as *"a phenomenon wherein a saturated material loses a large percentage of its shear resistance (due to monotonic or cyclic loading) and flows in a manner resembling a liquid"* (Castro and Poulos 1977)

the spectrum. No laboratory strength testing was done but, based on the index properties presented in Section 5.4, the high plasticity beds could be expected to have a drained residual friction angle on the order of 25 degrees if sufficient shear deformation is available for this strength to develop. The reduction of strength to this residual value could have happened in a progressive way along a shear surface and, once the limit of equilibrium was reached, could have led to the initial drained movement and could have triggered the subsequent undrained flow failure.

8. The effect of hydraulic conductivity variations within the glacial lacustrine unit, or within other stratigraphic units. Several orders of magnitude of difference in the value of hydraulic conductivity are likely to have existed within the on-site earth materials. In conjunction with the infiltration from rainfall, these hydraulic conductivity contrasts can lead to hydraulic forces and seepage gradients in adverse directions and unfavorable locations. In the valley floor, artesian conditions could be the result of the confinement of more free draining materials by those that are less permeable. On the slope, these conditions could trigger failure. Additionally, soil piping was observed locally along the slide margin on both the right and left flanks of the landslide. Soil pipes can work like an extreme contrast in hydraulic conductivity and, in a period of rapid infiltration, act to apply large hydraulic pressure, erode material, and destabilize the slope.

9. The relatively short interlude for subsurface drainage and consolidation after the 2006 slide. Landsliding disrupts subsurface drainage, as well as surface drainage (Item 4 in this list), and wet landslide debris can take a long time to dewater. Evidence of this is the many places on the slide mass where, by the time of our reconnaissance two months after the landslide, a crust had formed on the surface, yet the soil beneath could not support a person's weight. These areas will continue to drain but additional rainfall and infiltration also will occur. It could be many years before the groundwater regime in the slide mass is at an equilibrium state, uninfluenced by the water it incorporated in a prior landslide event. In fact, Thorsen (1969) mentions this observation two years after the 1967 reactivation. Consolidation, strength gain, and the increase in density that would make liquefaction unlikely occur with drainage, and take about the same amount of time. As described in Section 4.2, many episodes of sliding have occurred since the 1930s, but no precedent existed for two events of roughly the size of the 2006 landslide occurring within an 8-year period. Thus, the 2006 landslide mass could have been in a particularly loose and weak state when its remobilization initiated the 2014 landslide.

10. The contribution of river and flood plain water in changing the character of a slide that was otherwise similar to the 2006 or earlier slides, only nominally larger. Previous slides had pushed the river to the south but none apparently had the momentum to entrain the river and possibly some of the saturated valley alluvium (which is seen in the Stage 1 deposits). It is possible that, by being just a little larger and by originating a little higher on the slope, the toe

of Stage 1 of the 2014 slide entrained the river water and some saturated valley alluvium, and thereby contributing to rapid strength loss.

The evidence suggests that after mobilization, the front of Stage 1 became a turbulent flow because, not only did it travel a great distance and overwhelm the houses and structures south of the river, but little of its original ground surface was preserved as indicated in photographs taken by first-responders immediately following the disaster. The post-2006 slide mass had a dense deciduous tree forest, but little of the forest floor, or trees from the forest, is preserved on the surface of the current deposit. Furthermore, intact blocks of lacustrine clay, till, or advance outwash near and south of the SR 530 alignment tend to be small, typically less than 1 m (3 ft) in maximum dimension. In fact, the advance front of Stage 1 became so fluid that parts of the deposit appear to be more of a hyper-concentrated flow deposit than debris flow and some of the margin appears to have been a water-borne log-front pushed ahead of the debris flow (Figure 5.3.27). More discussion of this zone (Zone F) is in Section 5.2.

In contrast, the trailing edge of the Stage 1 landslide includes rafts of forest floor and hummocks of sandy outwash material that appear largely intact. This contrast is evident in Figure 6.2.1, which shows the two zones of the Stage 1 deposit (Zones E and F) beyond the river, as viewed from the top of the main scarp.

The great size of the trees along the northern end of Zone E indicates that this portion of Zone E originated upslope of the 2006 landslide headscarp, as pre-2014 landslide aerial photographs show that only smaller and dominantly deciduous trees were present on the surface of the 2006 landslide. Relatively small, deciduous trees are increasingly prevalent toward the middle and distal areas of Zone E where progressively smaller block sizes reflect disintegration of the original land surface, indicating that these distal portions of Zone E originated within the 2006 slide mass. Aerial photographs show the 2006 slide surface as having immature deciduous vegetation (Figures 2.4.2E and 2.4.2F). Most such vegetation in Zone E was observed in the center and at the southern margins of the block field, which we therefore infer originated from the 2006 landslide surface. We interpret the observations that the topographic block size diminishes with distance travelled (indicating that the blocks broke up with displacement to the south), the preservation of patches of original forest floor with live, rooted ferns, and that some trees remain upright (although not vertical), as evidence of rafting of coherent sections of the original ground surface above a deeper slide plane or liquefied material zone.

Sand boils (Figure 5.2.27) and sand ejecta (Figure 5.2.26) were observed in the Stage 1 deposits and sand ejecta were also in the distal portions of Stage 2. Sand boils are a clear indication of liquefaction and sand ejecta may be the same. Sand ejecta may also be the result of Stage 2 impacting the relatively fluid and loose deposits of Stage 1, and indicate the way the deposits were subsequently dewatered.

6.3 Stage 2

Stage 2 was also a rapid and dramatic failure, with the main scarp block dropping approximately 350 feet (100 m) and parts of the mass traveling longitudinally for 1000 to 2000 feet (300 to 600 m) in less than approximately two minutes. Portions of the Stage 2 slide mass remained much more coherent than in Stage 1, with the main scarp block remaining intact for the full 1300 foot (400 m) width of the slide (Figure 5.2.6). Blocks that travelled farther are progressively smaller but still easily discernable in photographic or lidar images, and on the ground surface. Field evidence of a two-stage failure is most recognizable south of the river and north of the SR 530 alignment, where signs of impacts between the two stages are visible:

An area of broken and more randomly oriented trees is one of the key signs of impact and is shown in Figure 5.3.19. Another sign of impact in this area is a thin gray, gravelly, sandy veneer which is no more than two inches (50 mm) thick and generally less than one inch (25 mm) thick. In some locations this veneer appears to define a certain elevation in a channel or basin and in others it is splashed randomly on higher, sandy ground. It is the splashed veneer on either side of the impact zone where the trees are broken that indicates the impact of a collision.

With respect to the mechanism of movement, Stage 2 can be subdivided into four types and areas. The upper part of Stage 2 underwent no more than 700 feet (210 m) of lateral movement and rotated backward as a slump block so that the ground surface is largely intact and all trees have fallen and been laid flat by the downward acceleration or the back rotation and stopping of the block. This area has a classic slump-block morphology and the stratigraphy of recessional outwash over till appears largely intact (Zone A2 and A3 in Figure 5.3.1; Figure 6.1.3). Note that the till appears to have been a little more mobile and to have travelled farther downslope near the east margin, as can be seen in Figure 5.3.1 (Figure 6.1.3).

The upper middle part has an extensional morphology with back rotation evident by ground surface slopes, exposure of repeating stratigraphy, slickensides, and, in one location shown in Figure 5.3.8b, the skid marks left by fallen trees are clearly inscribed upon a slope. The lower middle part of the Stage 2 slide mass shows more signs of extension, including thinning of the outwash cover, and less back rotation of slump blocks. The area of extension is the lower part of Zone B as shown in Figure 5.3.1 (Figure 6.1.3).

The lower part of the Stage 2 mass is the exposure of sheared lacustrine deposits that are the expression on the toe of the shear surface and the bottom of the slide mass. The Stage 2 slide mass in this area contributed to the damming of the river by plugging the low spot left by the trailing edge of Stage 1 and by pushing the Stage 1 debris higher near the area of impact. This is generally the area identified as Zone D in Figure 6.1.3 and includes the lower part of Zone B, where the recessional outwash cover is thin. Since this area, which adjoins Zone C and is downslope of many of the observed seeps on the left flank, probably was exceptionally wet as it

was overridden by the Stage 2 failure, the sand ejecta found here could be evidence of the means by which the sand was dewatered.

Seismic records show that several discernable events also occurred within an hour of the Stage 1 failure and these are all considered to be part of Stage 2 in that they happened after the Stage 1 collapse, remained north of the river, and, therefore, did not contribute to the damage south of the river. Some of these are likely smaller failures of the main scarp, for example, Zone A4, which is clearly visible (Figure 6.1.3). Some of these likely had other origins because, despite the continued raveling of soil for over two months (at the time of our visit the scarp was continuously and audibly raveling and a few approximately 10 cubic meter collapses occurred each day during our field reconnaissance), the scarp and slump block still are clearly defined and look fresh. In fact, that fresh appearance helps to make Zone A4 stand out as an exception. Other possible sources for these small seismic signals include debris flows in Zone C and the back-rotation of slump blocks in Zones A3 and B, as they came to equilibrium after their rapid emplacement.

6.4 Summary

The hypothesis presented here is that the Oso Landslide moved in two primary stages. Stage 1 mobilized as a debris flow comprised largely of colluvium and recent to prehistoric Holocene landslide debris. It caused the destruction of human life and property south of the river. Thus, observations related to the initiation and mobilization of Stage 1 are particularly important. Our observations through reconnaissance and minimal associated testing and analysis led to the following possible contributing factors that rendered Stage 1 was so devastating;

1. Three weeks of extreme rainfall preceding the event.
2. Changes to groundwater recharge from slope movements and possible with contributions from timber harvesting on Whitman Bench.
3. The elevation of the post-2006 slide debris being low enough to capture more of the groundwater from the Headache Creek basin.
4. The post-2006 landslide slope gradient was flatter than it had been previously and thus was more receptive to capturing runoff.
5. Static liquefaction of the 2006 landslide mass.
6. Dilation and strain softening on the pre-existing shear surfaces and elsewhere in the glacial lacustrine unit.
7. Strength degradation toward residual values on pre-existing shear surfaces in the lacustrine deposits.

8. The effect of hydraulic conductivity variations within the glacial lacustrine unit, or within other stratigraphic units.

9. The relatively short interlude for subsurface drainage and consolidation after the 2006 slide.

10. The contribution of river and flood plain water in changing the character of a slide that was otherwise similar to the 2006 or earlier slides, only nominally larger.

It is noteworthy that there are so many possible contributing factors and mechanisms of material behavior. In other words, our work did not conclude that only one path could have led to the Stage 1 failure. It is likely that a combination of a number of these is predominantly responsible, with more minor influence from others. Further research will better identify the most probable contributions from each and how they influenced the initiation, timing and consequence of this failure. Pending such investigations, we believe that all of the above factors and mechanisms warrant further consideration regarding how they contributed to the Stage 1 failure, and how they might apply to other slopes. Other factors and mechanisms could well emerge from additional research on the Oso Landslide.

Stage 2 followed Stage 1 within no more than a few minutes. Stage 2 was a retrogressive slide that mobilized on a new steeply dipping slip surface in outwash, till, and lacustrine deposits, and then travelled rapidly downslope on an ancient, existing shear surface that has contributed to many slides, and most recently to Stage 1. Stage 2 came to rest at the headward (upslope) edge of the Stage 1 deposit and the evidence of impact here is central to the interpretation of two main stages of rapid movement separated by at least as much time as it took the trailing edge of Stage 1 to come to rest. The Stage 2 deposit is still present on the slope and is estimated to be up to 150 feet (45 m) deep above the existing slide surface and in some places it is less deep than prior to the March 22 slide and in others it is deeper.

Stages 1 and 2 likely represent the two large seismic records and approximately 1 hour of several other recognizable seismic events probably include scarp retrogression (Zone A1 and A4), slump block rotation in Zone A3 and the upper part of Zone B, and possibly debris flows emanating from Zone C. It is possible, however, that Stages 1 and 2 both mobilized in the period of the first seismic signal because that could be enough time for the trailing edge of the Stage 1 deposit to have come to rest before being hit by Stage 2, though we think this timing is less likely, however, as that would mean that the second seismic signal would be due to far smaller failures, such as that of Zone A4.

Other hypotheses of failure mechanisms were also evaluated, including a full-height flow slide and a slide that started with failure of the Whitman Bench, bringing the prominent slump block with the felled trees down with the initial movement. These were judged to be less representative of what must actually have happened for a couple primary reasons. The full-height flow slide is

inconsistent with the amount of material left high on the slope, the relatively intact morphology of the slump block (Zone A) and the blocks in Zone B showing extension through translation, but also rotation. Rather, these observations suggest many slip surfaces coalesce on a basal slide surface. A mechanism having the new failure into the Whitman Bench coming first, as could be envisioned because of the way the 2006 landslide debuttressed the upper slope, is inconsistent with the observations of impact between this material and that which must have been in place already (Zones E and F).

Of course one attribute of a mechanism involving a full-height flow slide or the collapse of the Whitman Bench is the potential energy released at that time would be greater, and lead to easier explanation of the flow extent. However, the prevalence of water near the distal margin and the fluidity of the debris as understood through observations in the field and eyewitness accounts from those nearby and from first responders may be enough to explain the extremely low shear strength and large travel distance of Zone F. Section 7 describes some preliminary analyses of runout distance and comparison with other historical landslide events and it appears that a full-height failure of the Whitman Bench slope is not needed to produce the observed runout. Future research into the Oso Landslide runout will be quite valuable.

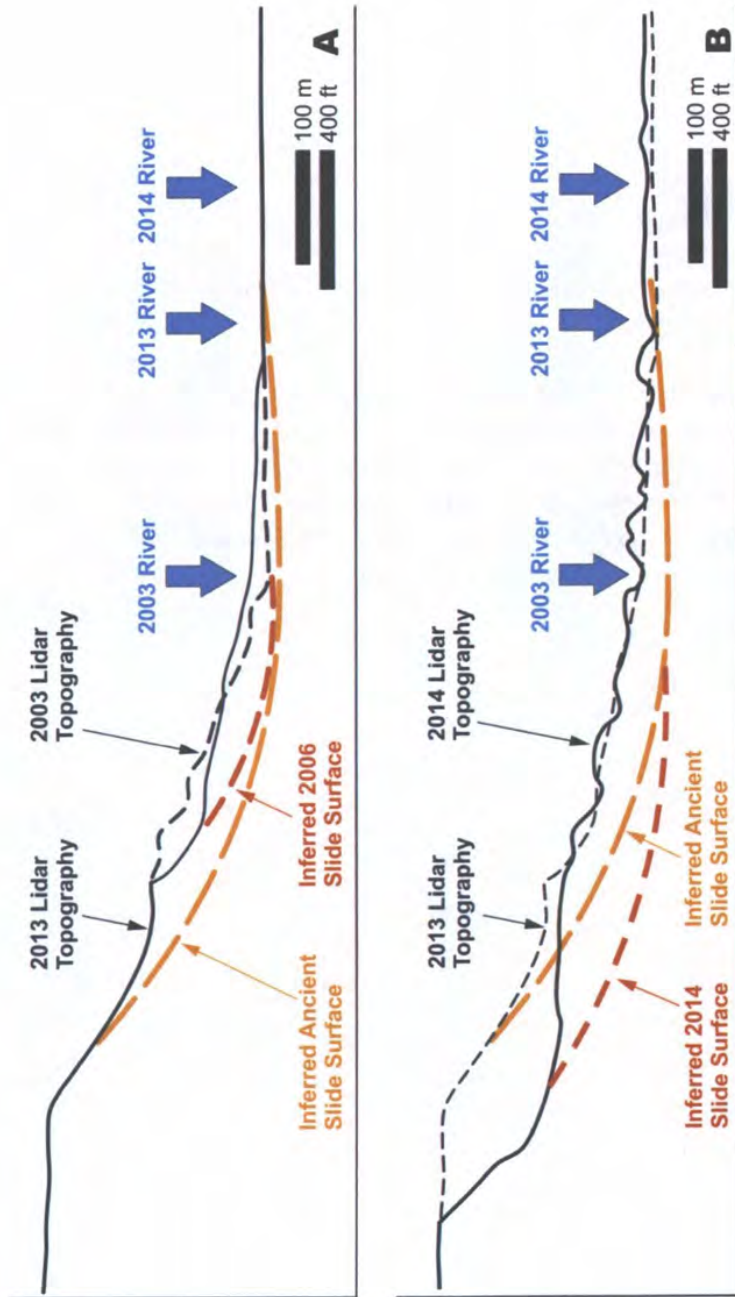


Figure 6.1.1: Schematic cross section (modified from A-A' from Figure 4.1.8) showing conceptualized 2006 and ancient slide surfaces (upper diagram). Also shown is a conceptualized 2014 slide surface (lower diagram).

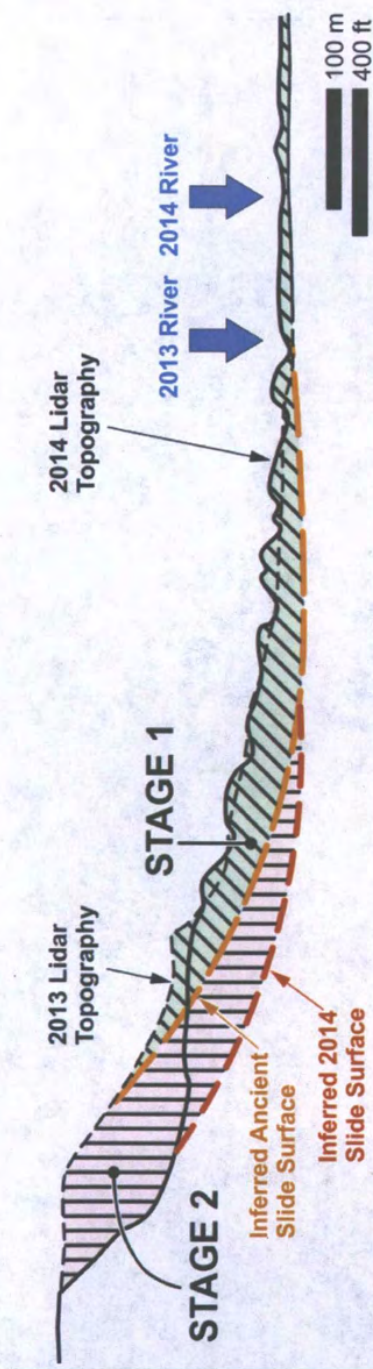


Figure 6.1.2 Schematic cross section (modified from A-A' from Figure 4.1.8) with conceptualized boundaries of Stage 1 and Stage 2 shown by hatch marks. Stage 1 evolved to be essentially a remobilization to the prehistoric slide surface. Stage 2 mobilized the material between the prehistoric slide surface and the 2014 slide surface.

Figure 6.1.3. Conceptual landslide stage map.



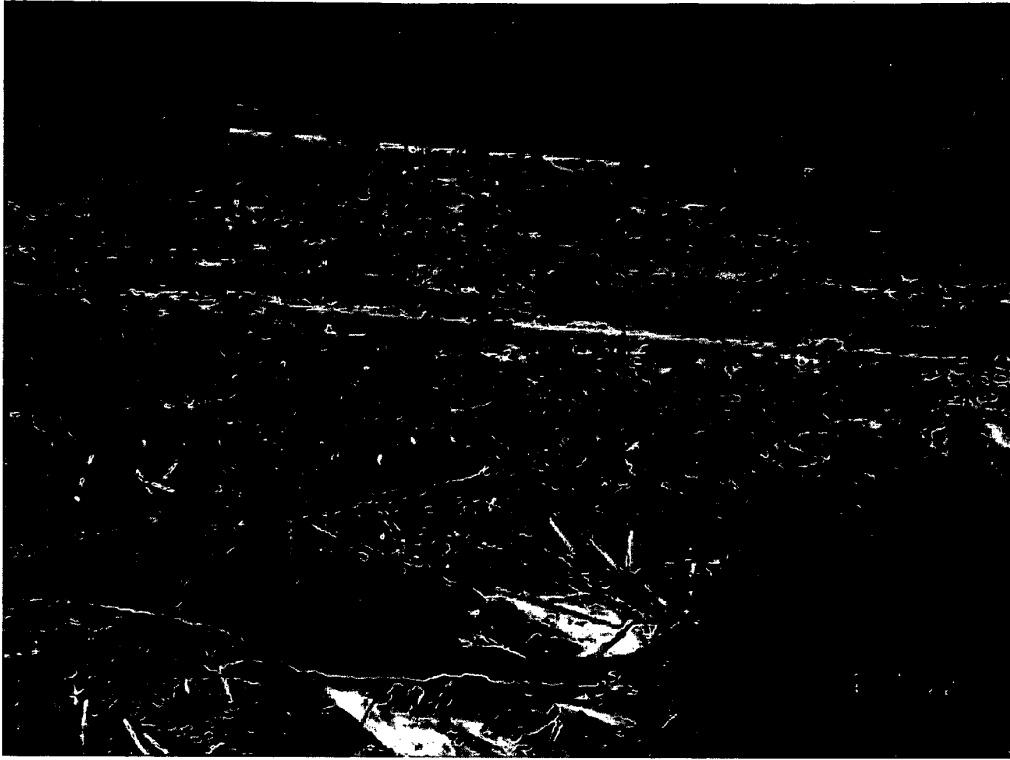


Figure 6.2.1 View of the distal zones of the deposit from the headscarp showing excavation of Highway SR 530 in the approximate center of the photograph. The highway is an approximate boundary between the distal zone where very little of the original ground surface is preserved and trailing part of Stage 1 where remnants of the forest floor have been rafted into position. View from the headscarp.

7. DISCUSSION

This discussion section provides context for some of our observations. The mission of the GEER reconnaissance is to observe conditions in the field rather than determine the causality of the event. However, the extent of our reconnaissance effort has allowed us to point to some of the factors that we believe pertinent to the landslide at Oso.

7.1 Historical Context

Slope failures can occur on natural slopes or as a result of excavations, cuts, fills, embankment loadings, groundwater flow and seepage forces, earthquakes, and other processes that induce stresses. Understanding and predicting the timing and extent of these events have challenged the geotechnical engineering community for decades. Some slope failures result in significant losses and casualties, especially when they occur in developed areas and debris flows accompany them. Several well-documented cases have shown that the runout from these events can reach significant distances even on relatively shallow slopes and occur at great velocities. Fast-moving debris flows are arguably the most destructive class of mass movements. For example, an M7 earthquake in El Salvador in 2001 caused the collapse of a section of the crest of the Balsamo Ridge overlooking the suburb of Santa Tecla (Evans and Bent, 2004; Konagai et al., 2001). About $150,000 \text{ m}^3$ ($\sim 196,000 \text{ yd}^3$) of pyroclastic material slid down slopes varying from 30° to 15° for about 275 m (900 ft) and then ran out an additional 460 m (1,500 ft) on a slope of about 3° . The velocity was estimated to range from about 16 m/sec (35 mph) to 5 m/sec (11 mph \sim top speed of running person) on the flatter slope. Once it reached the residential area it continued for another 200 m (650 ft) burying houses. The furthest reach was 740 m (2,400 ft) with flow thickness of about 2 m (6.5 ft) at the distal end. The slide caused more than 700 fatalities with a total duration estimated to be less than one minute.

Rainfall-induced landslides are also common occurrences. For example, the 1985 Jizukiyama landslide in Japan was thought to be triggered by 449 mm (17.7 inches) of rainfall in the rainy season which is twice the amount of rainfall in a typical year in the Nagano area. The volume of the slide was estimated at $5 \times 10^6 \text{ m}^3$ (~ 6.5 million yd^3) with a total length of 700 m (2,300 ft), and an initial slip surface located at 30 to 50 m (100 to 165 ft) depth. The runout travelled approximately 200 to 300 m (650 to 1000 ft) resulting in the destruction of 50 houses and 26 deaths (Sassa, 1985). The Jizukiyama landslide runout moved at fairly low velocity ($\sim 10 \text{ cm/sec}$, 0.22 mph) and entrained several meters of surficial soils as it travelled. The landslide mass consisted of ancient landslide debris, probably ten thousand years old, and was composed of volcanic tuff (ash and pumice). The 2006 Guinsaigon slide on the island of Leyte in the Philippines was also triggered by rainfall, where an 11 million m^3 (~ 14.4 million yd^3) rockslide entrained an additional 4 million m^3 (~ 5.2 million yd^3) of finer debris, evolving into an extremely rapid slide which traveled about 1.3 km (0.8 mi) on a practically flat surface, burying the town of Guinsaigon and resulting in more than 1000 fatalities (Evans et al., 2007).

Before the Oso Landslide occurred, most landslide disasters in the US resulted in significant material losses with fewer casualties. Nevertheless, according to USGS, the average death toll in the United States from landslides and debris flows is about 25 per year (NRC, 2004). The largest documented rock slide-debris flow, estimated at 2.8 km^3 (0.7 mi^3) (Schuster and Highland, 2001), was produced by the eruption of Mount St. Helens, Washington in May 1980. The flow traveled roughly 22 km (14 mi), damaging or destroying roads, railway lines, bridges, and creating landslide-dammed lakes. Other well documented events include La Conchita in Southern California which had two events a decade apart (1995 and 2005). The bluff above La Conchita, composed chiefly of weakly cemented materials, had a long history of landslides, some prehistoric, with the 2005 rainfall-induced slide causing extensive destruction as well as 10 fatalities (Gibson, 2006).

7.2 Empirical Predictions of Runout

It is generally agreed that rapid flows involve liquefaction of the granular matrix of the sliding material, resulting in segregation of grain sizes into a coarser snout and lateral levees which basically exhibit drained behavior and a liquefied interior made up of finer particles that is capable of violently impelling the coarser snout over long runout distances (Iverson, 1997; Major and Iverson, 1999; Wang and Sassa, 2001). In the Guinsaugon case, for example, boulders up to 5 m in diameter were observed at the distal limit of the slide (Evans et al., 2007).

A clear understanding of the mechanics of flow slides and debris flows is essential to model the consequences of this type of failure and to help decision makers regarding hazard zoning and possible mitigation measures. However, a full understanding is lacking of how flow slides maintain the ability to move long distances at high velocities over low-angle slopes. Their mobility is greatly dependent on the nature and volume of the slide mass, the presence of water in the sliding mass, the size and nature of debris that is entrained in the flow, the slope angle at failure zone, the slope angle and ground surface roughness and constrictions/obstacles in the run out zone, and the presence of any water bodies, such as entrainable river or stream flow, along the runout path.

Two issues are involved: 1) triggering of the slide and 2) subsequent high-velocity, unsteady, non-uniform motion. With regard to triggering, a high degree of saturation in the pre-slide failure zone seems to be required; one basic scenario would be that, as pore pressures increase due to a rising groundwater table, the effective stresses decrease, and thus the shearing resistance on the potential failure plane decreases allowing the slope to fail and the sliding material to mobilize (e.g., Anderson and Sitar, 1995). Whereas many landslides can be modeled as solid blocks sliding over defined failure surfaces, debris flows ultimately mobilize the whole mass of sliding material as a viscous flow with distributed shearing.

Evaluating runout distances is based on several factors including volume of the sliding mass, slope height, slope angle, site topography and morphology, obstructions, geologic material type,

grain size distributions, water content, degree of saturation, strength parameters, and failure types. Determining runout distances remains highly empirical though critical in establishing zoning for safe development. Methods to predict runout distances have been developed using landslide volumes, which can potentially expand by 10 to 30 % compared to in-place material (Jaboyedoff et al., 2008). The methods are simple and based on historical observed data on events with broad variations in conditions, materials and morphology. Significant scatter of the observed past events results in estimates that cannot be used in practice with great certainty (McDougall, 2006). Analytical prediction methods also have been developed and can in some cases improve on the empirical estimations. However, the analytical methods tend to be complex and require knowledge and/or estimation of several parameters. Discussion of analytical methods is beyond the scope of this report. Runout distances also are influenced greatly by material entrainment as the initial failed mass travels downhill gathering surface materials, trees, scouring the landscape, and incorporating water from valley sediments and bodies of water such as creeks and rivers. Runout distances also are influenced by various obstacles in the debris runout zone which can either shorten the distance or increase it as a result of channelization. The presence of water, silt and clay tends to promote greater runout distances. As the silt and clay content increases, it helps maintain high excess pore water pressures within the debris flow (Iverson, 2003). Using several flume experiments, Wang and Sassa (2001) found that those high excess pore pressures occur after the initiation of failure rather than prior to failure.

The angle of reach (α) or travel angle, also known as fahrböschung (Heim, 1932), represents the angle from the top of the landslide scarp to the distal edge of the debris flow (Figure 7.2.1) and can be used to estimate runout distances based on volume, V . From the landslide geometry, the ratio of landslide height (H) to the horizontal distance from the top of the scarp to the distal edge (L) is defined as $\tan(\alpha)$.

Figure 7.2.2 shows a graph of the travel angle as a function of landslide volume (note that the travel angle is indiscriminately represented as α or β). The trend also shows that for the same volume, as the $\tan(\alpha)$ decreases, the runout increases. Estimating the runout distance for the Oso Landslide is challenging because of the stages of the sliding, the spreading of the debris flow to the east and west side and the incorporation of river water from the North Fork Stillaguamish River. In addition, the initiation point for Stage 1 can only be estimated consequently making the debris volume of Stage 1 difficult to assess with certainty. Corominas (1996) used debris flows, debris slides and debris avalanches to develop the following empirical relationship relating the angle of reach and the debris flow volume, V :

$$\tan \alpha = H/L_{\max} = 0.97 V^{-0.105} \quad \text{Equation 7-1.}$$

Hungr et al. (2005) later revised this expression by landslide type, resulting in a slightly improved relationship for debris flows, as given in with the regression coefficients given in Table 7.2.1.

$$\text{Log } \tan \alpha = A + B \text{ Log } V \quad \text{Equation 7-2.}$$

Table 7.2.1 Regression coefficients for Equation 7-2 (adapted from Hungr et al. 2005).

Landslide Type	Paths	A	B	R ²
Debris Flows	All	-0.012	-0.105	0.76
	Obstructed	-0.049	-0.108	0.85
	Unobstructed	-0.031	-0.102	0.87

Rickenmann (1999) estimated the maximum runout distance based on data from 154 debris flow events as shown in Equation 7-3:

$$L_{\max} = 1.9 V^{0.16} H^{0.83} \quad \text{Equation 7-3.}$$

Legros (2002) proposed a relationship between landslide runout length and volume rather than the apparent friction angle, travel angle or angle of reach (H/L). He contended that the ratio H/L is physically meaningless in predicting runout length and therefore proposed a relationship based on volume (V in km³) rather than height of fall. Equation 7.4 shows the general form of his powerlaw equations with the coefficients c and n shown in Table 7.2.2 for non-volcanic and volcanic landslides and debris flows:

$$L_{\max} = c V^n \quad \text{Equation 7-4.}$$

Table 7.2.2 Parameters for empirical relationships of Legros (2002) in Equation 7-4.

Event Type	c	n
Non-volcanic	8	0.25
Volcanic	15.6	0.39
Debris Flow	235	0.39

Landslides tend to develop into debris flow given sufficient fluid input and consequently increase in mobility (Iverson, 1997). Figure 7.2.3 displays the data gathered from numerous case histories (Legros, 2002)

These various formulations have been used with the observations made at the Oso landslide considering the possibility of a two phase failure as well as a single phase incorporating the entire slide mass.

For Phase 1 of the Oso Landslide, L_{\max} can be measured from cross-sections shown in Figure 7.2.4 and is estimated at 1,433 m (4,700 ft) with a height H equal to 90 m (300 ft). Incorporating both phases yield an L value of 1,677 m (5,500 ft) and H of 182.9 m (600 ft). The total volume of the Oso slide can be estimated at approximately at 7.6 million m³ (9.9 million yd³) with Stage 1 being estimated anywhere between 50 and 85 % of the total volume. Using values shown in Table 7.2.2, the predicted runout using Equation 7-3 from Rickenmann (1999) underestimates the

runout for a two phase failure but agrees well with the less probable one stage failure. The method of Legros (2002) using Equation 7-4 for the volcanic debris flows shows the observed runout in closer agreement with the volume of Phase 1 being 50% of the total landslide volume. These predictions support that the hypothesis of a two phase event likely occurred and are consistent with the seismic signals recorded and previously discussed in Section 5. Using the powerlaw relationship from Legros (2002) for debris flows yielded unrealistic runouts in excess of 35 km. Overall these other empirical methods seem to predict reasonably well the observed runout distances.

The travel angles obtained using Corominas' (1999) improved expression given in Hungr et al. (2005) as well as the calculated values from the Oso landslide are overlaid onto Figure 7.2.2. The results suggest that for the Oso Landslide the prediction method based on the total volume of 7.6 million m³ (9.9 million yd³) gives a travel angle as predicted by Corominas. However, using the assumed travel angles for the Phase 1 and Phase 1 and 2 cases fall below or are at the lower bound of the Corominas line but similar to the Swiss Alps debris flows.

Table 7.2.3 Predicted runout distances for 2014 Oso Landslide based on estimated total volume of 7.6 million cubic meters (268 million ft³)

Failure Scenarios	Volume (km ³)	H (m)	tan (α)	tan (α) Hungr et al. (2005)	Measured L _{max} (m)	Predicted L _{max} (m) Rickenmann (1999)	Predicted L _{max} (m) Legros (2002)
Total Volume	0.0076	183	0.109	0.185	1,675	1,808	2,326
80% of Total	0.00608	92	0.064	0.189	1,435	982	2,132
50% of Total	0.0038	92	0.064	0.199	1,435	910	1,775

Legros (2002) for volcanic landslides; Hungr et al. (2005) for unobstructed debris flows

7.3 Influence of Forest Practices on Groundwater Levels and Slope Stability

While it is unclear, at this point, as to whether or to what degree logging may have influenced the stability of the slope at the Oso Landslide, monitoring of other deep-seated landslides has revealed ties to timber harvest at other locations (Swanston et al., 1988). The shallow depth of root penetration relative to the depth of the slide plane of deep-seated landslides generally is taken to result in little direct influence of reduced post-harvest root strength. Instead, the potential connection is thought to lie in timber harvest effects on groundwater recharge. Deep-seated landslides in general are more influenced by seasonal, and multi-year groundwater fluctuations than by individual precipitation events (Iverson and Major, 1987, Iverson, 2000). After rainfall begins in the autumn months, the soil moisture must be replenished before recharge to deeper groundwater can occur and it takes time for infiltrating flow to reach a deep groundwater table. Hence, it is not unusual for deep-seated landslides in the region to occur late in the winter, or in spring months.

Groundwater flow to the Oso Landslide is controlled by local topography and stratigraphy. The outwash sand and gravel capping the slope are highly permeable, whereas the glacial till and lacustrine silt and clay have much lower permeability. This permeability contrast creates an unconfined aquifer in the outwash deposits above the till and a confined aquifer between the till and glacial-lacustrine deposits. Thus, multiple seepage pathways exist in the site stratigraphy. Evidence for local seeps along the recessional outwash/till contact was apparent on the headscarp face after the 2014 landslide. In addition, active seepage (with associated hydrophyllic) vegetation was observed flowing at and over the topmost exposure of till observed along the trail leading down from the Whitman Bench through the Headache Creek basin along the eastern margin of the Oso Landslide.

Shannon and Associates (1952) and Benda et al. (1988) noted the potential for the Oso (Hazel) slide to capture flow from Headache Creek. Along these lines, the increase in local relief between the Headache Creek basin and the body of the Oso Landslide due to slope movement in 2006 (Figure 4.1.5) would have increased groundwater transfer from the Headache Creek basin into the Oso landslide. Springs mapped along the eastern portion of the Oso slide scarp (Figure 5.3.12) likely reflect this effect as the potential recharge area for those springs lies within the topographically defined Headache Creek drainage basin. At the top of the eastern scarp are numerous tension cracks filled with water.

During our field reconnaissance, no evidence of overland flow or surface water diversion was observed along the logging roads on Whitman Bench immediately upslope of the 2014 Oso Landslide. The roadside ditches were uniformly overgrown and exhibited no observable evidence of erosion or sediment transport by overland flow. Likewise, such evidence was not apparent on the roadway surfaces. Nor was evidence of overland flow or erosion observed in areas of the undisturbed forest floor examined during field reconnaissance. We thus see no basis for inferring a role for road surface runoff from the Whitman Bench in triggering the landslide. It appears that rainfall onto the Whitman Bench infiltrates with minimal (and likely negligible) runoff and thus the fraction of incoming precipitation not lost to interception by tree canopies and evapotranspiration contributes to groundwater recharge. Hence, we infer that groundwater recharge to the 2014 Oso Landslide came from direct precipitation onto the landslide and from groundwater flow from both the Whitman Bench and the adjacent Headache Creek drainage basin.

Miller and Sias (1997; 1998) noted several studies that identified apparent correlations between the timing of slope movement and nearby timber harvest at the Oso Landslide and at other nearby sites with similar geology. Benda et al. (1988), for example, noted a 1950s era increase in landslide activity following 1940 harvests on Whitman Bench, and a similar pattern of mid-1960s landsliding following additional harvests in 1960. Miller and Sias (1998) noted localized slumping visible on 1991 aerial photographs following timber harvest in the groundwater recharge area on Whitman Bench in 1988. They suggested that an apparent time lag of 5 to 20

years between timber harvest and landslide movement at the site reflected the influence of increased groundwater recharge following timber harvest (Miller and Sias, 1997).

Increased groundwater levels have been correlated with increased deep-seated landslide activity at other sites (e.g., Iverson and Major, 1987). Hydrologic studies have reported significant increases in streamflow after clear cutting and partial harvest, and in general a decrease of forest cover leads to an increase in both annual water yield and in groundwater levels due to decreased evapotranspiration and thus increased infiltration (Harr, 1986, Troendle and King, 1987, Grant et al., 2008). A number of studies have shown post-logging increases in peak groundwater levels during rainfall or snowmelt events (Gray and Megahan, 1981; Megahan, 1984; Wu 1984), and Peck and Williamson (1987) found that annual minimum and peak water tables increased steadily over the decade following timber harvest. Groundwater modeling studies also have demonstrated a link between timber harvest and increased soil moisture and groundwater levels (Hillman and Verschuren, 1988). Other studies have shown the converse effect of how maturing trees can lower groundwater tables. For example, using a spatially distributed hydrologic model to examine the effects of vegetation on the hydrologic regime of a deep-seated earthflow in the French Alps, Malet et al. (2005) found that planting 20-year-old conifers could reduce the water table level by almost 1 m.

Moore and Wondzell (2005) estimated that interception loss in Pacific Northwest conifer forests ranged from 10% to 30%. Dingman (2002) reported similar values for Pacific Northwest plant communities, ranging from 21% to 35%, based on canopy characteristics and climate conditions. Hannel (2011) reported hydrologic modeling (DHSVM) that predicts a 27% decrease in evapotranspiration resulting from forest conversion to shrub for a site on western Olympic Peninsula, Washington.

The importance of groundwater flow to prior movement of the Oso (Hazel) slide was pointed out in a number of studies dating back to the 1950s (Shannon and Associates, 1952; Benda et al., 1988; Miller and Sias, 1998). In the summary of their report: Environmental Factors Affecting the Hazel Landslide to the Washington State Department of Natural Resources, Miller and Sias (1997) note that “the results indicate that clearcut logging in the groundwater recharge area of the landslide will accelerate landslide activity.” Assessing in more detail the potential effects of historical timber harvest on groundwater levels and movement of the Oso (Hazel) landslide are beyond the scope of our reconnaissance effort.

7.4 Influence of Renewed Riverbank Erosion on Slope Stability

A series of Google Earth images from 2003 to 2013 show the effect of the 2006 landslide on the river channel location and the subsequent construction of a log revetment designed to prevent river incision into the toe of the 2006 landslide (Figures 2.4.2E and 2.4.2F). The image from July 2005 (Figure 7.4.1a) shows the meander bend of the North Fork Stillaguamish River and the unstable bare slope to the northwest on the outside of the meander (flow is from right to left).

The subsequent photograph, from March 2006 (Figure 7.4.1b) shows that the 2006 landslide pushed the river several hundred feet to the south where a new, narrower channel was established with a right-angle bend. The photograph from August 2007 (Figure 7.4.1c) shows that a detention pond was constructed, a grove of relatively large trees was removed, and the river was moved to the north, and a log revetment was constructed running along the toe of the 2006 landslide deposit. This photo also shows the development of a point bar on the inside of the meander bend. The photograph from April 2009 (Figure 7.4.1d) shows the detention pond filled with sediment and the log revetment apparently beginning to deform. The photograph from June 2009 (Figure 7.4.1e) shows re-excavation of the detention pond, the apparent stockpiling of excavated material on the toe of the 2006 landslide, repair of the log revetment, and a temporary access road across the river. The photograph from September 2011 (Figure 7.4.1f) shows revegetation of the 2006 slide and further erosion behind the log revetment. The photograph from July 2013 (Figure 7.4.1g) shows the partial dismantling of a portion of the log revetment on the downstream side of the apex of the meander bend where the erosive force of the flow would be expected to be greatest. Erosion along the outer bank of the meander bend also reportedly incised a roughly 3 m (10 ft) deep pool at this location where, according to some accounts, it had been possible to wade across the channel immediately after construction of the log revetment. Another second-hand account related to us commented on the fluid or liquefied nature of the soil material behind the revetment.

A tribal fisheries biologist forwarded his observations from a visit to the “Steelhead Haven cribwall” on the Thursday, March 20, 2014, two days prior to the catastrophic March 22, 2014, landslide. He noted that at one location over the previous 7+ years, the river had eroded several meters (about 10 feet) into the material behind the log revetment but that during his March 20 visit he did not notice evidence that would indicate further erosion behind the revetment during 2013 or the high river flows in 2014. He noted that the lower (submerged) portions of the revetment remained connected to large ballast structures installed to anchor the logs.

7.5 Benchmarks for Risk

A rough approximation for the annual probabilities of multiple fatalities due to landslides in the site vicinity (the 5-km stretch of valley shown in Figure 4.1.2) based on historical performance through March 2014 is established as follows:

- Slope failures that translate the river channel and potentially impact people within hundreds of meters of the toe (such as the landslides in 1951, 1967 and 2006) occur between once per decades (say 30 years) and once per centuries (say 300 years). The probability of fatalities is taken to be less than the probability of a landslide to account for the possibility that these landslides do not necessarily lead to fatalities (e.g., several properties were destroyed but no lives were lost in the six decades prior to 2014). The possible number of fatalities is taken to be roughly bounded between one and ten.

- Large slope failures that run-out thousands of meters across the valley and its inhabitants (such as the March 2014 event) occur between once per centuries (say 300 years) and once per millennia (say 3,000 years). This assessment for the annual probability is based on Haugerud's (2014) mapping of previous landslides (Figure 4.1.2) together with the carbon dating from our reconnaissance indicating 15 slides occurred over the past 6000 years. The possible number of fatalities depends on the number of people present in the valley below the slope at the time of the event; it is taken to be roughly bounded between ten and 100.

The rough assessments of failure probabilities for different human safety consequences are plotted in Figure 7.5.1 for this 5-km stretch of the valley. This plot shows the annual probabilities for different events versus the consequences of those events; both probabilities and consequences are expressed as order-of-magnitude ranges due to the limited information used to assess them.

No national or state guidelines exist in the United States for levels of risk due to natural landslides that warrant action. However, several benchmarks exist for the risk to human safety that provide informational context for the risk in this 5-km stretch of valley; these benchmarks are included in Figure 7.5.1 for comparison.

One benchmark is for natural slopes in other developed countries. For example, Hong Kong (GEO 1998) and Australia (AGS 2000) have recommended guidelines for risk levels that warrant action to reduce the risk. If this valley were located in one of these countries, then action to reduce the risk would be considered warranted (Figure 7.5.1). However, neither of these countries have the same legal system or regulatory system as the United States.

A second benchmark is the level of risk associated with major flood-protection systems in the United States (IPET 2009 and DWR 2008). This information provides context for what we are achieving in this country for a related natural hazard that is more regulated than natural landslides. The risk to human safety due to natural landslides in this valley is smaller than what exists for two major levee systems, one in California and one in New Orleans (Figure 7.5.1), primarily because the population at risk in the North Fork Stillaguamish River Valley is smaller.

A third benchmark is the risk from flooding in the developed Green River Valley, located south of Seattle (Gilbert 2013). The risk of flooding on the Green River is regulated by a major dam. It is possible that the risk from flooding in the North Fork Stillaguamish River Valley may be larger than that due to natural landslides.

A fourth benchmark is for major dams in the United States. The United States Bureau of Reclamation has established guidelines for risk levels that warrant action to reduce the risk in order to prioritize resources for remediating existing dams (USBR 2003). While the USBR (2003) risk thresholds are expressed in a way that cannot be plotted directly on Figure 7.5.1, they are similar to those shown on the figure for existing slopes in Australia and Hong Kong. If the risk in

this valley were due to a major dam rather than natural landslides, then “justification to take expedited action to reduce the risk” would be warranted (USBR 2003). However, this natural slope is not an engineered facility like a dam. In addition, the risk from a dam is to some extent imposed by society on the people living downstream from the dam in contrast to a risk that is accepted voluntarily.

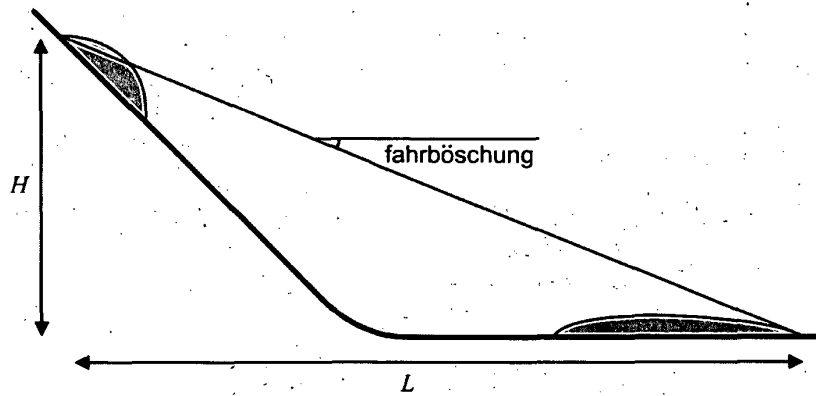


Figure 7.2.1 Definition of angle of reach or fahrböschung (after McDougall, 2006).

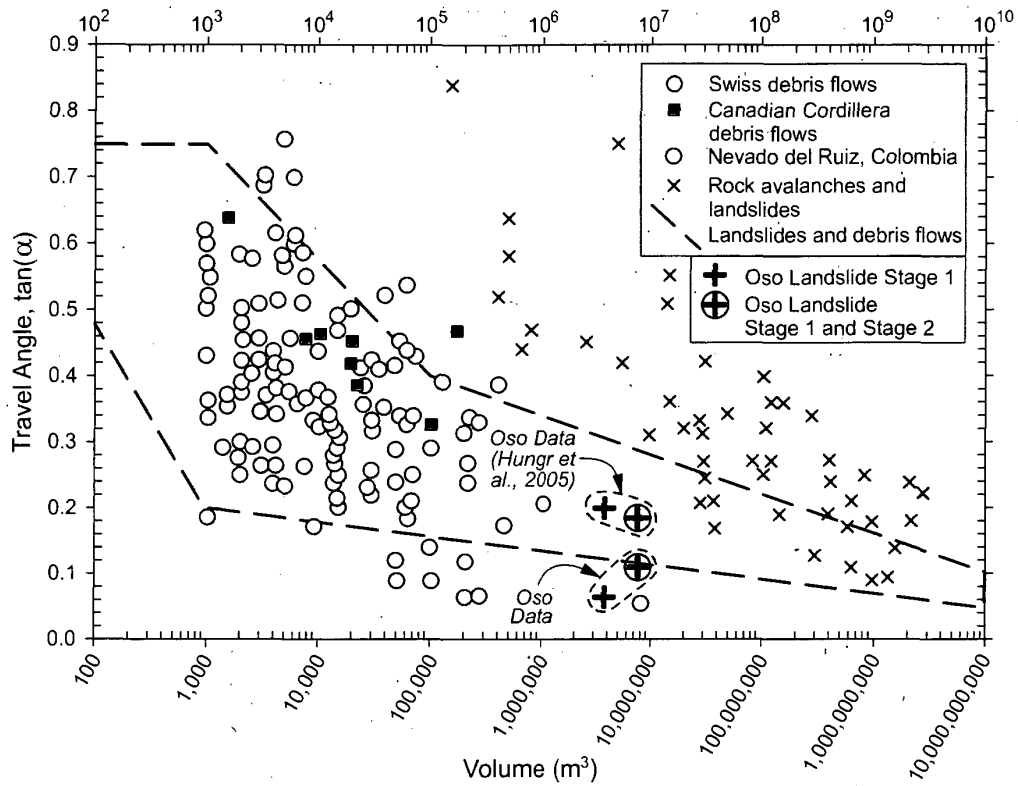


Figure 7.2.2 Travel Angle versus Volume of Mass Movement (adapted from Jakob and Hungr 2005). The data represented in this figure is from various case histories including debris flows, debris avalanches, rock falls and landslides. The travel angle for the Oso Landslide was estimated using the empirical relationship of Hungr et al. (2005) for debris flows using the total volume of the Oso slide and using 50% of the total volume. The lower data points are the travel angles based on the landslide height, H and the horizontal distance from the headscarp to the distal edge, L measured at Oso for the total volume and for 50% of the total volume of the slide.

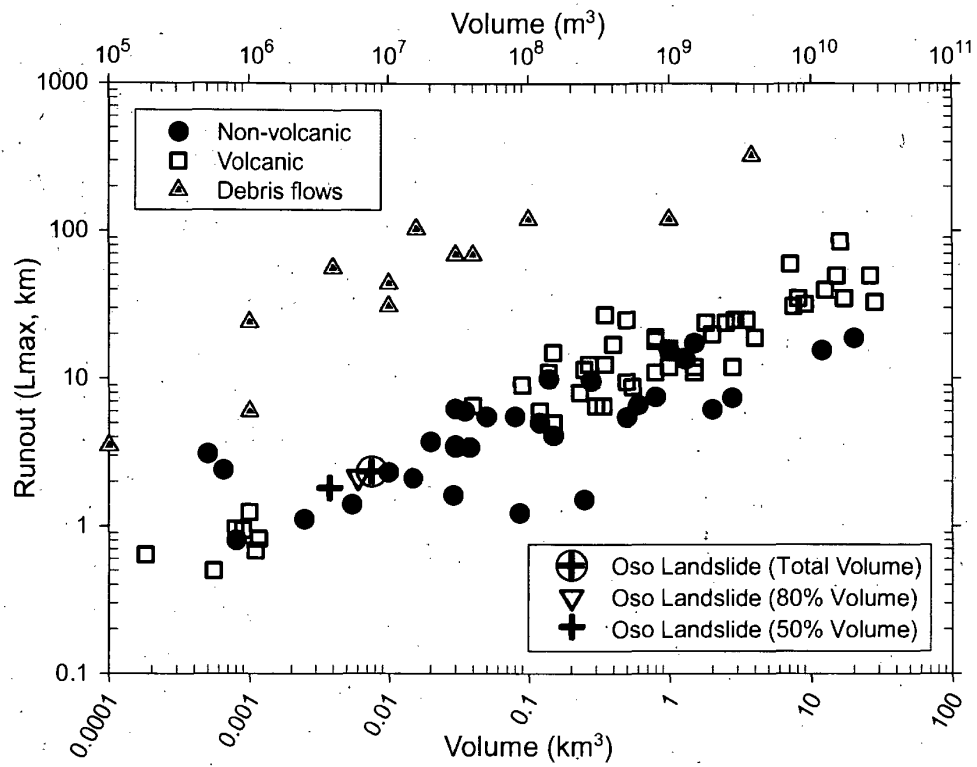


Figure 7.2.3 Relationship between volume and runout distance (after Legros, 2002):

Figure 7.2.4 Profile showing starting locations for Stage 1 and Stage 2 events at Oso.

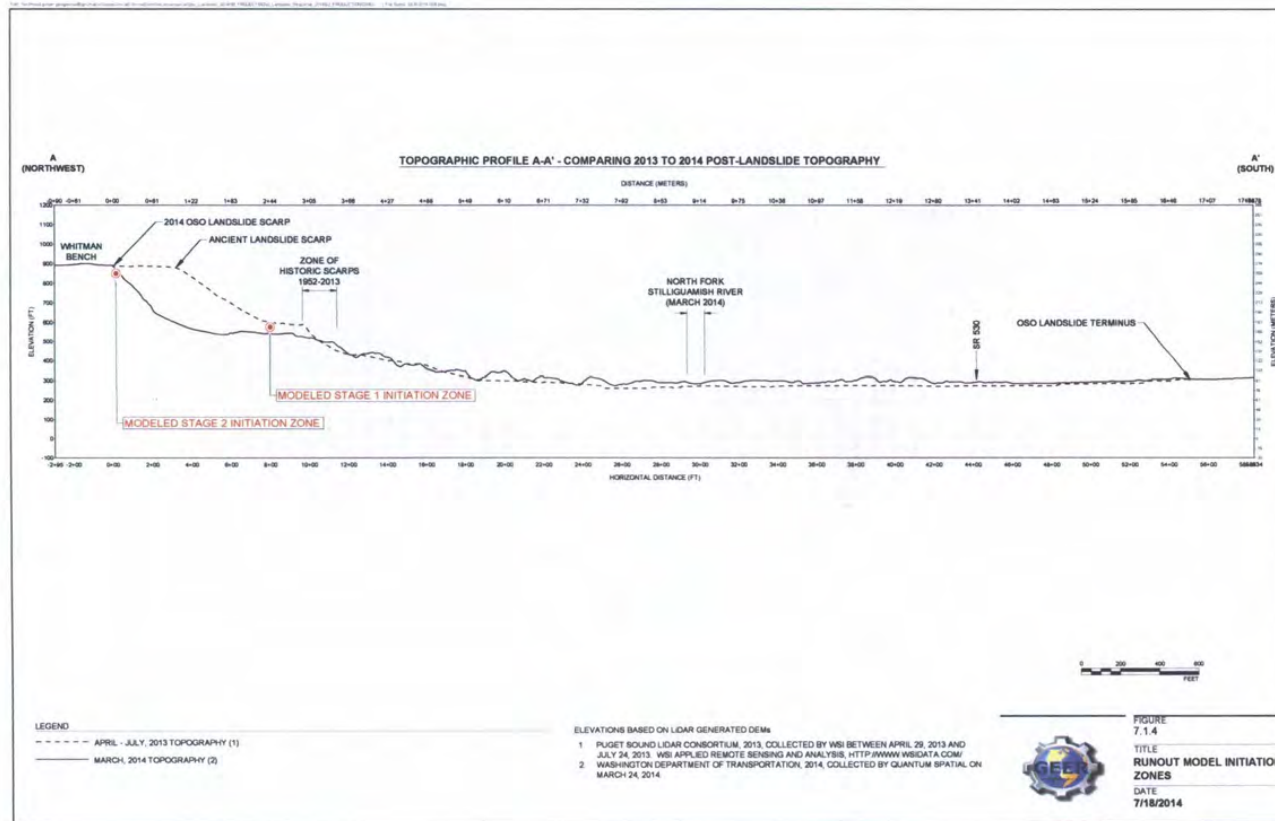




Figure 7.4.1a Google Earth image from 7/2005.



Figure 7.4.1b Google Earth image from 3/2006



Figure 7.4.1c Google Earth image from 8/2005



Figure 7.4.1d Google Earth image from 4/2009.



Figure 7.4.1e Google Earth image from 6/2009.



Figure 7.4.1f Google Earth image from 9/2011.

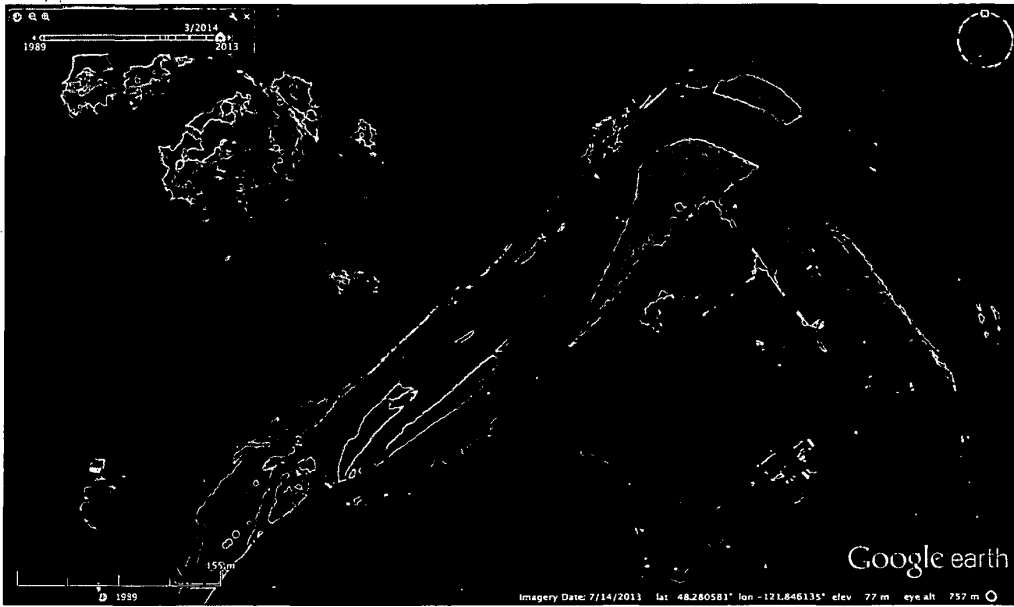


Figure 7.4.1g Google Earth image from 7/2013.

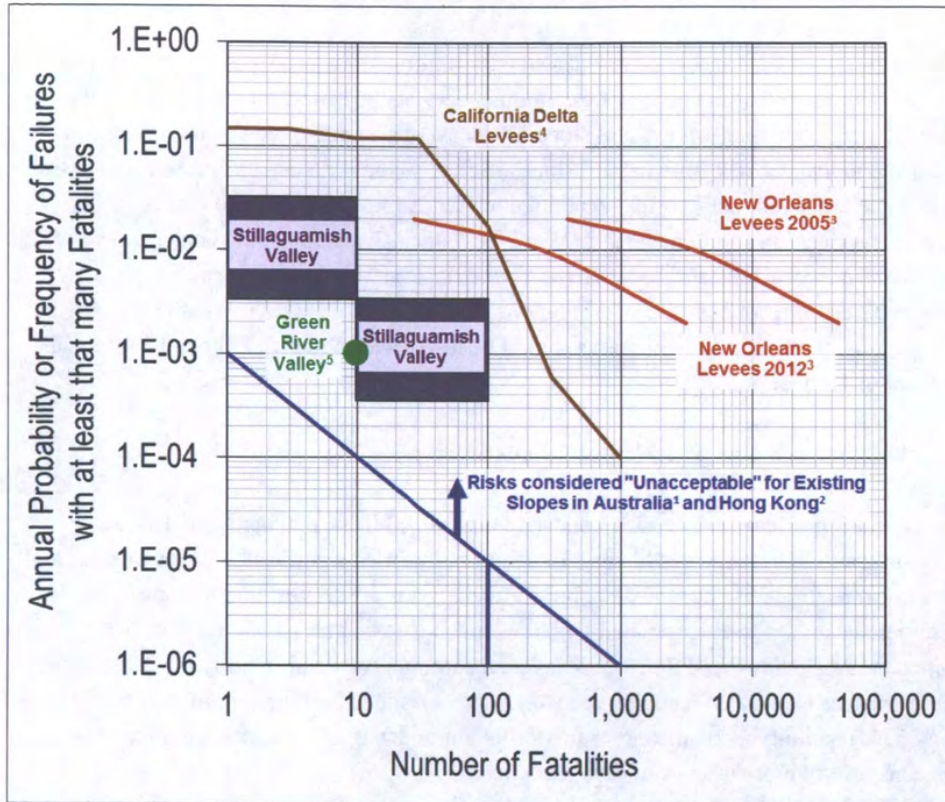


Figure 7.5.1 Rough approximation of risk from landslides in 5-km stretch of North Fork Stillaguamish River Valley in vicinity of Oso compared with related benchmarks for human safety risk (¹AGS 2000; ²GEO 1998; ³IPET 2009; ⁴DWR 2008; ⁵Gilbert 2013).

8. CONCLUSIONS AND RECOMMENDATIONS

The 22 March 2014 Oso Landslide provides an opportunity for the profession to build on our knowledge of the stability and behavior of natural slopes and to reflect on the influence of people, climate, and time on natural valleys and slopes. This event also highlights the importance of assessing and managing risk from natural slopes. Below we present conclusions specific to the 2014 landslide and additionally offer several recommendations. As discussed earlier in this report, our investigation is not intended to be a final, conclusive study of the landslide and we did not seek to unequivocally establish causative factors; instead, this report is a preliminary assessment based on reconnaissance observations and other available data. We recommend that our conclusions, findings, and hypotheses should be tested and challenged through additional research and investigation.

8.1 The 22 March Oso, Washington Landslide

- **Impacts and Significance:** The Oso Landslide claimed 43 lives, making it the deadliest landslide disaster in United States history. In addition, it caused significant injuries to at least 10 people who were struck by the landslide, but fortunately survived. Washington State officials have estimated capital losses associated with the landslide to be at least \$50 million. The landslide completely destroyed Steelhead Haven, a community of almost 50 homes, as well as several residences located off a nearby roadway. The landslide also buried portions of State Highway 530, resulting in complete closure of this important arterial thoroughfare for over 2 months, and several more months of reconstruction.
- **Landslide Setting:** The last glacial advance into the Puget Lowland deposited a thick sequence of sediments into the North Fork Stillaguamish River valley, including the portion of the valley at the Oso Landslide. The glacially-derived sediments include interbedded layers of clay, silt, sand, gravel, cobbles, and boulders. Some of these glacially-derived sediments are landslide susceptible, especially when they form steep slopes or have abundant groundwater. The geomorphic evidence in the valley reveals that the portion of the North Fork Stillaguamish River Valley in the vicinity of Oso Landslide has experienced multiple large landslides over at least the past six thousand years. Many of these ancient landslides have similar morphology to the 2014 Oso Landslide, and indeed the Oso Landslide was a reactivation of one of these ancient landslides. The 2014 Oso Landslide was large, but the other ancient landslides in the valley are of similar size. There is geomorphic evidence that a landslide that is even larger than the Oso landslide is located immediately to the west of the Oso Landslide. This larger unnamed landslide similarly ran out across almost the entire North Fork Stillaguamish River Valley and appears to have pushed the river channel to the south margin of the valley. Many portions of the valley bottom are covered with old landslide deposits. We believe areas of the valley bottom not currently covered with landslide deposits have been covered in the past but the deposits in these areas been reworked by active channel migration and floodplain-forming alluvium deposition.

We estimate a maximum recurrence frequency of about 400 to 1,500 years for large landslides in this portion of the valley. The range in this estimate is constrained by carbon dating, which suggests four generations of large landslides, and a total of 15 mapped large landslides over about 6,000 years, as described herein. It is not known how many prior landslides occurred during valley incision and widening and which are no longer preserved in the topography; the presence of additional landslides in this immediate portion (~12 km² or ~5 mi²) of the valley could reduce the recurrence interval to the order of hundreds of years.

• **History of Landslides at the Oso Site:** Multiple episodes of historic movement of the Oso landslide have been described in several studies dating back to the 1950s. The historic landslide activity is occurring within the ancient Oso Landslide. The observed historic activity appears to be periodic with the modern headscarp (i.e., upper portion) episodically advancing headward between 1952 and 2006, but with the main slide mass constrained to approximately the same portion of the slope where the earlier 2006 landslide failed. Review of the available historic data indicates several dates of renewed activity on portions of the slope since the 1930s. A complete chronology of actual dates and the sizes and type of failures has not been compiled; however these are known to include rotational slumps, transverse sliding of blocks where the forest has remained intact, and debris flows. The size of the landslide area grew relatively slowly until a large increase occurred in 2006, followed by the catastrophic enlargement in 2014.

• **Initiation of the 2014 Oso Landslide:** The Oso Landslide initiated on Saturday, 22 March 2014, at approximately 10:37 a.m. local time on a clear, sunny day. Records indicate no significant seismic activity in the days preceding the landslide and therefore it is unlikely that it had a tectogenic origin. Instead, it is highly probable that the intense 3-week rainfall that immediately preceded the event played a major role in triggering the landslide. The intense rainfall in the first three weeks of March at the nearest rain gauge was determined to be less than the 100-year event for this period of time, and the previous months in the fall and winter of 2013 and 2014 were relatively dry. Precipitation in the Oso region is highly variable and analysis of weather radar for the area for the week preceding the landslide indicates that precipitation at the Oso Landslide was at least 229 mm (9 inches), suggesting that the precipitation at the Oso Landslide for March 2014 might have been more than 760 mm (30 inches).

Beyond the rainfall trigger itself, there are many other factors that likely contributed to destabilization of the landslide mass. These include: (i) alteration of the local groundwater recharge and hydrogeological regime due to previous landsliding and, possibly, land use practices, (ii) weakening and alteration of the landslide mass due to previous landsliding and other natural geologic processes, and (iii) changes in stress distribution resulting from removal and deposition of material from earlier landsliding. Detailed consideration of land use practices (most notably, timber harvesting) was beyond the scope of our investigation; however, it is known most of the large landslides in the Stillaguamish River Valley pre-date logging. Given the size and depth of the landslide, if timber harvest practices did influence on the landslide, it was

through modification of the groundwater recharge regime rather than by any shallow-depth loss of root mass reinforcement.

- **Oso Landslide Morphology and Dynamics:** During our field reconnaissance we identified six distinctive zones and several subzones of the landslide mass that are characterized by different geomorphic expression resulting from different styles of deformation, geologic materials, and vegetation. These reflect the highly complex nature of the landslide. It is apparent from the seismic recording of the landslide that the event was marked by two major episodes of mass movement separated by a few minutes. This corroborates with our data found during the reconnaissance, which provides evidence of multiple stages of failure. Clearly the most significant episode of landsliding involves the massive and fast-moving debris flow ("mudflow"), which devastated Steelhead Haven and caused most if not all of the fatalities. We found that the runout of this debris flow was indeed long (greater than 1 km); however, it was not exceptional for a landslide of its size. Runout may have also been aided by the inclusion of the Stillaguamish River water increasing the mobility of the debris flow, particularly on the east side, where the debris flow travelled up the river channel.

- **Hypothesized Landslide Sequence:** Based on the reconnaissance observations, seismic recordings, and other available data, we hypothesize that the landslide occurred in two distinct and markedly different stages. The first major stage of movement (Stage 1) is interpreted to be a remobilization of the 2006 slide mass and a headward extension that included part of the forested slope of the ancient landslide. As such, Stage 1 was comprised largely or entirely of previous landslide deposits and it mobilized as a debris flow and traveled across the valley. The second stage (Stage 2) occurred several minutes later in response to the unloading (i.e., loss of "buttressing") and the redirection of stresses within the landslide mass. Stage 2 was a retrogression into the Whitman Bench of up to nearly 90 m (300 feet) horizontally from the ancient slide scarp. The Stage 2 slip surface probably joined the slip surface of Stage 1 (and that of the 2006 and ancient slides) at depth, but also included shearing along a length up to 300 m (1000 feet) or more through previously in-place outwash, till and glacial lacustrine deposits that had not been part of earlier landslides. The Stage 2 landslide moved rapidly on the existing Stage 1 slip surface until it essentially collided with the more intact blocks at the trailing edge of the Stage 1 slide mass, and came to rest. The current morphology suggests there was back rotation and extension of the Stage 2 landslide mass as it failed and came to a reestablished equilibrium on the slope.

- **Landslide Risk Assessment, Management, and Communication:** Studies conducted in the decades preceding the Oso Landslide clearly indicated a high landslide hazard at the site. However, these studies were primarily focused on the impacts of landslides to the river versus the impacts to people or property. In addition, it does not appear that there was any publicly communicated understanding that the debris from a landslide could run-out as much as 1 km, as it did in the 2014 event. Since the 1950s, a variety of means were considered to manage the risk associated with this slope, ranging from stabilizing the riverbank to minimize erosion to moving

the river channel and removing development by buying out properties. At the time of the 2014 event, two means had been employed to manage risk from a landslide: (i) conventional land-use restrictions implemented by Snohomish County and the Washington Department of Natural Resources and (ii) riverbank stabilization implemented by the Stillaguamish Tribe of Indians. Our assessment of the risk for fatalities due to landslides in this portion of the valley indicates that it is comparable to risks from flooding in other areas in the United States but relatively high compared to guidelines for landslides in other developed countries and for large dams in the United States. Currently there are no national or state guidelines in the United States concerning levels of risk due to natural landslides that warrant action.

8.2 Recommendations

Several broader lessons have been learned in this investigation that may benefit others involved in the study of landslides and the zoning of communities adjacent to sloping ground and potentially unsafe slopes.

- The history and behavior of past landslides and associated colluvial soil masses should be carefully investigated when mapping areas for zoning purposes. At the Oso Landslide site, multiple past failures retrogressively moved upslope each time creating new conditions with increased susceptibility to groundwater infiltration, and preferential underground seepage pathways, and further weakening the previously failed mass over time and increased overall volume of potentially unstable landmass.
- The risk of landslides to people and property should be assessed and communicated clearly and consistently to the public. These assessments should be continuously updated as new information about slope behavior becomes available and as potential consequences change due to changes in development or mitigation.
- The ability to implement monitoring and warning systems to reduce the impacts of landslides to people and property should be considered and advanced.
- The influence of precipitation on destabilizing a slope should consider both cumulative amounts and short-duration intensities in assessing the likelihood of initial or renewed slope movement.
- Methods to identify and delineate potential landslide runout zones should be revisited and reevaluated.
- Advancements in imagery to understand slope behavior should be exploited to the greatest extent possible. Lidar imagery has proven to be a very useful and valuable tool in identifying landslide deposits, reconstructing landslide history, and evaluating mass movements of the current landslide event. This technology has been made feasible over the last decade or so and still does not cover most of the country. Its availability here, and its availability at multiple times

(2003, 2013, and after the failure in 2014) allows an understanding of slope and landslide morphology, and thereby hazard and risk, that was not present prior to 2003 in this valley and is currently not present in most locations. Additionally, high-resolution aerial photography also is a valuable tool to help delineate zones within the failed mass and document damages prior to recovery and clean up efforts

- Seismological recordings of landslides should be utilized to assist in understanding failure sequence in terms of the timing of significant movements, especially in large and complex events. Use of conventional slope stability analysis methods alone may be insufficient for accurate evaluation of failure mechanisms.
- Doppler weather radar should be utilized in providing data regarding precipitation intensity, amount, and variability estimates at locations of interest that are distant from established gauges.

9. ACKNOWLEDGMENTS

The Geotechnical Extreme Events Reconnaissance (GEER) Association, supported by the U.S. National Science Foundation (NSF), organizes the response of the geoenvironmental community to earthquakes and other natural disasters such as floods, landslides, tsunamis, etc. GEER members donate their time, talent, and resources to collect time-sensitive and potentially perishable field observations and data of the effects of extreme events. The GEER Association web site, which contains additional information, may be found at: www.geerassociation.org

The authors of this report on the Oso Landslide are greatly indebted to a number of individuals, agencies, consulting firms and organizations for their support in providing access to the Oso Landslide disaster area, assisting in the field reconnaissance effort, generating and compiling data and information, and assembling the final report. These numerous collaborators, listed below, are gratefully recognized:

- Oso Fire Department and Rescue Personnel accompanied the GEER team during the reconnaissance work ensuring safety
- Harvey Greenberg, University of Washington, for his assistance with lidar data
- Dale E. Topham and Jeffrey Jones, Snohomish County, Public Works and Engineering Services, for assistance in the field and for sharing their knowledge of the geology, the site and surrounding terrain
- Dave Norman, Washington State Department of Natural Resources, State Geologist
- Washington State Department of Transportation (WSDOT) and in particular Tom Badger, Casey Kramer and the WSDOT GeoMetrix Office for sharing their observations and analysis, and for high definition aerial imagery
- Darrington Ranger Station provided the precipitation data for the Darrington RS gauge
- Golder Associates Inc. personnel provided several GIS and other figures prior and following the GEER reconnaissance: Clayton Johnson and Ben Vang-Johnson
- University of New Hampshire graduate students performed the tree distribution analysis and the laboratory testing: Michael Bogonko, Evangelos Korkolis and Americo Santamaria
- Patrick Stevenson, Representative for Stillaguamish Tribe of Indians, and Randolph R. Sleight, Chief Engineering Officer, Snohomish County Planning and Development Services, for sharing information about land-use policies and risk management
- Kjristine Lund, Consultant, Gregory Baecher, University of Maryland, Farrokh Nadim, Norwegian Geotechnical Institute, and Mark Lee, Ebor Geoscience Limited, for reviewing sections on risk
- Steve Kramer for feedback on static liquefaction, and Kate Allstadt and Colin Stark for helpful conversations about seismic signals of landslides.
- E. Leopold for preliminary identification of tree bark used in 14C dating.

This material is based upon work supported by the National Science Foundation under Grant No. CMMI 1266418. Any opinions, findings, and conclusions or recommendations expressed in this material are those of the authors and do not necessarily reflect the views of the National Science Foundation.

10. REFERENCES

AGS, (2000), "Landslide Risk Management Concepts and Guidelines," *Australian Geomechanics* v. 35/1, pp. 49-92.

Allstadt, K., Malone, S., Vidale, J., Bodin, P., and Steele, B. (2014), Seismic Signals generated by the Oso Landslide - Pacific Northwest Seismic Network summary - 26 March 2014, unpublished report.

Allstadt, K. (2013), Extracting source characteristics and dynamics of the August 2010 Mount Meager landslide from broadband seismograms, *J. Geophys. Res. Earth Surf.*, 118, 1472–1490, doi:10.1002/jgrf.20110

Anderson, S. A. and Sitar, N. (1995), "Analysis of rainfall-induced debris flows," *Journal of Geotechnical Engineering*, 121, 7, pp. 544-552.

Beechie, T. J., Collins, B. D., and Pess, G. R., (2001), Holocene and recent geomorphic processes, land use, and salmonid habitat in two North Puget Sound river basins, in *Geomorphic Processes and Riverine Habitat*, Dorava, J. M., Montgomery, D. R., Palcsak, B. B., and Fitzpatrick, F. A., editors, Water Science and Application Volume 4, American Geophysical Union, Washington, D.C., pp. 37-54.

Benda, L., Thorsen, G. W., and Bernath, S., (1988), *Report of the I.D. team investigation of the Hazel Landslide on the North Fork of the Stillaguamish River*, Report F.P.A. 19-09420, Report to the Washington Department of Natural Resources, Northwest Region, Sedro Wooley, Washington, 13 p.

Benda, L., Beechie, T. J., Wissmar, R. C., and Johnson, A., (1992), Morphology and evolution of salmonid habitats in a recently deglaciated river basin, Washington State, USA, *Canadian Journal of Fisheries and Aquatic Sciences*, v. 49, pp. 1246-1256.

Bishop, A. W., (1955), The use of the slip circle in the stability analysis of slopes, *Geotechnique*, v. 5, pp. 7-17.

Booth, D. B., 1989, *Surficial Geologic Map of the Granite Falls 15-Minute Quadrangle, Snohomish County, Washington*, U. S. Geological Survey Miscellaneous Investigations Series, Map I-1852.

Bottelin, P., Jongmans, D., Daudon, D., Mathy, A., Helmstetter, A., Bonilla-Sierra, V., Cadet, H., Amitrano, D., Richefeu, V., Lorier, L., Baillet, L., Villard, P., and Donzé, F.: Seismic and mechanical studies of the artificially triggered rockfall at the Mount Néron (French Alps, December 2011), *Nat. Hazards Earth Syst. Sci. Discuss.*, 2, 1505-1557, doi:10.5194/nhessd-2-1505-2014, 2014.

Cao, Q., Henn, B., and Lettenmaier, D.P., (2014), *Analysis of local precipitation accumulation return periods preceding the 2014 Oso Mudslide*: Unpublished paper, Department of Civil and Environmental Engineering, University of Washington, 9 p.

Corominas, J. (1996), The angle of reach as a mobility index for small and large landslides, *Canadian Geotechnical Journal*, 33, pp. 260–271.

Castro, G. and Poulos, S. (1977), Factors affecting liquefaction and cyclic mobility, *Jour. of the Geotech. Eng. Div., ASCE*, p. 501-516.

Cruden, D.M., and Varnes, D. J., (1996), Landslide types and processes, in *Landslides: Investigation and Mitigation*, Turner, A.K., and Shuster, R.L., eds.: Transportation Research Board, Special Report 247, pp 36–75.

Dammeier, F., J. R. Moore, F. Haslinger, and S. Loew (2011), Characterization of alpine rockslides using statistical analysis of seismic signals, *J. Geophys. Res.*, 116, F04024, doi:10.1029/2011JF002037.

Dingman, S.L., (2002), *Physical Hydrology*, Prentice Hall, 646 p.

Dragovich, J. D., McKay, D. T., Jr., Déthier, D. P., and Beget, J. E., (2000), Holocene Glacier Peak lahar deposits in the lower Skagit River valley, Washington, *Washington Geology*, v. 28, pp. 19-21.

Dragovich, J. D., Stanton, B.V. W., Lingley, W. S., Jr., Briesel, G. A., and Polenz, M., (2003), *Geologic Map of the Mount Higgins 7.5-minute Quadrangle, Skagit and Snohomish Counties, Washington*, Washington Division of Geology and Earth Resources, 1:24,000 scale, Open File Report 2003-12.

Dragovich, J. D., Logan, R. L., Schasse, H. W., Walsh, T. J., Lingley, W. S., Jr., Norman, D. K., Gerstel, W. J., Lapen, T. J., Schuster, J. E., and Meyers, K. D., (2002), *Geologic Map of Washington-Northwest*

Quadrant, Washington Division of Geology and Earth Resources, 1:250,000 scale, Geologic Map GM-50.

DWR, (2008), *Delta Risk Management Strategy Phase 1, Risk Analysis Report*, California Department of Water Resources.

Evans, S. G. and Bent, A. L., (2004) "The Las Colinas landslide, Santa Tecla: a highly-destructive flowslide triggered by the January 13, 2001, El Salvador earthquake," *Geological Society of America*, Special Paper 375, pp. 25-37.

Evans, S. G., Guthrie, R. H., Roberts, N. J. and Bishop, N. F. (2007), "The disastrous 17 February 2006 rockslide-debris avalanche on Leyte Island, Philippines: a catastrophic landslide in tropical mountain terrain," *Natural Hazards and Earth Systems Science*, 7, pp. 89-101.

Franklin, J. F., and Dyrness, C. T., (1973), *Natural Vegetation of Oregon and Washington*, USDA Forest Service General Technical Report PNW-8.

GEO, (1998), *Landslides and Boulder Falls from Natural Terrain: Interim Risk Guidelines*, Geotechnical Engineering Office Report 75, Government of Hong Kong.

GeoEngineers, (2001), *Steelhead Haven Landslide Remediation Feasibility Study, Alternatives development and analysis and preliminary project designs, RM 20, NF Sillagumish River*, Prepared for The Stillaguamish Tribe of Indians, Prepared by GeoEngineers Inc., April 26, 2001, 62 p.

Gibson, K.B. (2006), *Mudslide in La Conchita, California, 2005*, Mitchell Lane Publishers, 32 p.

Gilbert, R. B. (2013), "Expert Engineering Independent Third-Party Review, Briscoe-Desimone Levee Design, Green River Basin, State of Washington," Prepared for the King County Flood Control District, Prepared by R. B. Gilbert, February 16, 2013, 39 p.

Grant, G. E., Lewis, S. L., Swanson, F. J., Cissel, J. H., and McDonnell, J. J., (2008), *Effects of Forest Practices on Peak Flows and Consequent Channel Response – a State-of-Science Report for Western Oregon and Washington*: U.S. Department of Agriculture, Forest Service, Pacific Northwest Research Station, General Technical Report PNW-GTR- 760, 76 p.

Gray, D. H., and Megahan, W. F., (1981), *Forest Vegetation Removal and Slope Stability in the Idaho Batholith*, Research Paper INT-271, U.S. Department of Agriculture, Forest Service, Intermountain Forest and Range Experiment Station, Ogden, UT, 23 p.

Hannel, C. R., (2011), *Groundwater Response to Precipitation Events, Kalaloch, Olympic Peninsula, Washington*, M. S. Thesis, Western Washington University, Bellingham.

Harr, R. D., (1986), Effects of clearcutting in rain-on-snow runoff in western Oregon: a new look at old studies, *Water Resources Research*, v. 24, pp. 305-314.

Haugerud, R. A., (2014), *Preliminary Interpretation of Pre-2014 Landslide Deposits in the Vicinity of Oso, Washington*, U.S. Geological Survey Open-File Report 2014-1065, U.S. Geological Survey, Reston, <http://dx.doi.org/10.3133/ofr20141065>.

Heim, A., (1932), *Bergsturz und Menschenleben*. Naturforschenden Gesellschaft, Zürich. Translated by Skermer, N.A., 1989. *Landslides and Human Lives*. BiTech Publishers, Vancouver, British Columbia.

Hibert, C., G. Ekström, and C. P. Stark (2014), Dynamics of the Bingham Canyon Mine landslides from seismic signal analysis, *Geophys. Res. Lett.*, 41, doi:10.1002/2014GL060592.

Hillman, G. R., and Verscuren, J. P., (1988), Simulation of the effects of forest cover, and its removal, on subsurface water, *Water Resources Research*, v. 24, pp. 305-314.

Hungr, O., Corominas, J. & Eberhardt, E. (2005), Estimating landslide motion mechanism, travel distance and velocity. In *Landslide Risk Management*. Edited by O. Hungr, R. Fell, R. Couture & E. Eberhardt, A.A. Balkema, Leiden, pp. 99-128.

IPET, (2009), *Performance Evaluation of the New Orleans and Southeast Louisiana Hurricane Protection System - Volume VIII Engineering and Operational Risk and Reliability Analysis*, Final Report of the Interagency Performance Evaluation Task Force, U.S. Army Corps of Engineers.

Iverson, R.M., (1997), The physics of debris flows: *Reviews of Geophysics*, v. 35, pp. 245-296.

Iverson, R.M., (2000), Landslide triggering by rain infiltration, *Water Resources Research*, v. 36, pp. 1897-1910.

Iverson, R. M. (2003), "The debris-flow rheology myth," *Proc. Debris-Flow Hazards Mitigation: Mechanics, Prediction and Assessment*, Millpress, Rotterdam, ISBN 90 77017 78 X.

Iverson, R. M and Denlinger, R. P. (2001), "Flow of variably fluidized granular masses across three-dimensional terrain: 1. Coulomb mixture theory," *Journal of Geophysical Research*, V 106, B1, pp. 537-552.

Iverson, R.M. and Major, J.J., (1987), Rainfall, ground-water flow, and seasonal movement at Minor Creek landslide, northwestern California: Physical interpretation of empirical relations, *Geological Society of America Bulletin*, v. 99, pp. 579-594.

Jaboyedoff, M., Horton, P., Loye, A and Pedrazzini, A. (2008), Runout – Empirical Approaches, Workshop on Quantitative Landslide Risk Assessment and Risk Management, Barcelona, Spain, powerpoint presentation.

Konagai, K., Johansson, J., Mayorca, P., Uzuoka, R., Yamamoto, T, Miyajima, M., Pulido, N., Sassa, K, Fukuoka, H. and Duran, F. (2004), "Las Colinas landslide: rapid and long-traveling soil flow caused by the January 13, 2001, El Salvador earthquake," *Geological Society of America*, Special Paper 375, pp. 39-53.

Kottek et al., (2006), World map of Köppen-Geiger climate classification updated: *Meteorology Zeitschrift*, v. 15, p. 259-263, <http://koeppen-geiger.vu-wein.ac.at>.

Kramer, S. and Seed, H. (1987), Initiation of soil liquefaction under static loading conditions, *Journ. of Geotech. Enf.*, ASCE, P. 412-430

Legros, F., (2002), The mobility of long-runout landslides, *Engineering Geology*, v. 63, p. 301-331.

Major, J.J., and Iverson, R.M., (1999), Debris-flow deposition — effects of pore-fluid pressure and friction concentrated at flow margins, *Geological Society of America Bulletin*, v. 111, pp. 1424-1434.

Malet, J.P., van Asch, Th. W.J., van Beek, R., and Maquaire, O., (2005), Forecasting the behaviour of complex landslides with a spatially distributed hydrological model, *Natural Hazards and Earth Systems Sciences*, v. 5, p. 71-85.

McDougall, S., (2006), A new continuum dynamic model for the analysis of extremely rapid landslide motion across complex 3D terrain. Ph.D. Dissertation, Department of Earth and Ocean Sciences, University of British Columbia, Canada, 253 pp.

Megahan, W. F., (1984), Snow melt and logging influence on piezometric levels in steep forested watersheds in Idaho, Transportation Research Board, Washington, D.C., *Transportation Research Record 956*, pp. 1-8.

Miller, D. J., (1995), Coupling GIS with physical models to assess deep-seated landslide hazards, *Environmental & Engineering Geoscience*, vol. 1, pp. 263-276.

Miller, D. J., (1999), Hazel/Gold Basin Landslides: Geomorphic Review Draft Report, Report to U.S. Army Corps of Engineers, 25 pp.

Miller, D. J., and Sias, J., (1997), *Environmental Factors Affecting the Hazel Landslide*, Report to Washington Department of Natural Resources, Sedro Wooley, Washington.

Miller, D. J., and Sias, J., (1998), Deciphering large landslides: linking hydrological, groundwater and slope stability models through GIS, *Hydrological Processes*, v. 12, pp. 923-941.

Moore, D. R. and Wondzell, S. M., (2005), Physical hydrology and the effects of forest harvesting in the Pacific Northwest: a review, *Journal of the American Water Resources Association*, v. 41, pp. 763-784.

National Research Council (NRC), (2004), *Partnerships for Reducing Landslide Risk: Assessment of the National Landslide Hazards Mitigation Strategy*, National Research Council, Washington, D. C., 144 p.

Peck, A. J., and Williamson, D. R., (1987), Effects of forest clearing on groundwater, *Journal of Hydrology*, v. 94, pp. 47-65.

Palladino, D. J., and R. B. Peck, (1972), Slope failures in an overconsolidated clay, Seattle, Washington, *Geotechnique*, v. 22, pp. 563-595.

Papageorgiou, G., Fourie, A., and Blight, G. (1999), Static liquefaction of Merriespruit gold tailings, Proc. Geotechnics for Developing Africa, Balkema.

Porter, S. C., and Swanson, T. W., (1998), Radiocarbon age constraints on rates of advance and retreat of the Puget Lobe of the Cordilleran Ice Sheet during the last glaciation, *Quaternary Research*, v. 50, pp. 205-213.

Prochaska, A.B., Santi, P.M., Higgins, J.D. and Cannon, S.H. (2008), Debris-flow runout predictions based on the average channel slope (ACS), *Engineering Geology* 98, pp. 29-40.

Rickenmann, D. (1999), Empirical relationships for debris flows, *Natural Hazards*, 19, pp. 47-77

Rickenmann, D. (2005), Runout prediction methods, M. Jakob, O. Hungr (Eds.), *Debris-flow Hazards and Related Phenomena*, Praxis, Chichester, UK, pp. 305-324.

Sassa, K., (1988), Motion of landslides and debris flows—prediction of hazard area. Report for Grant-in-Aid for Scientific Research by Japanese Ministry on Education, Science and Culture (Project No. 61480062), 52 p.

Schuster, R. L. and Highland, L. M. (2001), Socioeconomic and environmental impacts of landslides in the Western Hemisphere, USGS Open File report 01-0276.

Shannon, W. D., and Associates, (1952), *Report on Slide on North Fork Stillaguamish River near Hazel, Washington*, unpublished report to the State of Washington Departments of Game and Fisheries, 18 p.

Stuiver, M., and Reimer, P. J., (1993) (version 7.0), Extended 14C database and revised CALIB radiocarbon calibration program; *Radiocarbon*, v. 35, pp. 215-230.

Suriñach, E., I. Vilajosana, G. Khazaradze, B. Biescas, G. Furdada, and J. M. Vilaplana (2005), Seismic detection and characterization of landslides and other mass movements, *Nat. Haz. And Earth. Syst. Sci.*, 5, 791-798.

Swanston, D. N., Lienkaemper, G. W., Mersereau, R. C., and Levno, A. B., (1988), Timber harvest and progressive deformation of slopes in southwestern Oregon, *Bulletin of the Association of Engineering Geologists*, v. 25, pp. 371-381.

Tabor, R. W., Booth, D. B., Vance, J. A., and Ford, A. B., (1988), *Geologic Map of the Sauk River 30-by 60-Minute Quadrangle*, Washington, U. S. Geological Survey Open File Report 88-692.

Thorsen, G. W., (1969), *Landslide of January 1967 which diverted the North Fork of the Stillaguamish River near Hazel*, Memorandum dated November 28, 1969, to Marshall T. Hunting, Department of Natural Resources, Geology & Earth Resources Division, Olympia, WA.

Thorsen, G. W., (1989), Landslide provinces in Washington, in R. W. Galster (ed.), *Engineering Geology in Washington*, v. 1, Bulletin 78, Washington Division of Geology and Earth Resources, Department of Natural Resources, pp. 71-89.

Troendle, C. A., and King, R. M., (1987), The effect of partial and clearcutting on streamflow at Deadhorse Creek, Colorado, *Journal of Hydrology*, v. 90, pp. 145-157.

USBR, (2003), *Guidelines for Achieving Public Protection in Dam Safety Decision Making*, Dam Safety Office, United States Bureau of Reclamation, Denver, Colorado.

USGS (2014), http://www.usgs.gov/blogs/features/usgs_top_story/landslide-in-washington-state/

Wang, G., Sassa, K., 2001. Factors affecting rainfall-induced flowslides in laboratory flume tests. *Geotechnique* 51 (7), pp. 587-599.

Wu, T. H., (1984), Effect of vegetation on slope stability, Transportation Research Board, Washington, D.C., *Transportation Research Record 956*, pp. 37-46.

APPENDIX A

Field reconnaissance

Members of the GEER Oso Landslide team conducted a ground-based field reconnaissance during the month of May 2014. Specific dates of visits (and areas covered) are as follows:

- Team members JW and JdIC conducted an overview visit to the lower portion of the landslide (i.e., south of the North Fork of the Stillaguamish River) on 2 May 2014
- Team member JW conducted a reconnaissance of the lower portion of the landslide on 13 May 2014
- Team member JW and DM conducted an reconnaissance of the upper portion of the landslide (i.e., north of the North Fork of the Stillaguamish River) on 15 May 2014
- The entire team conducted a reconnaissance of the upper portion of the landslide on 22 and 24 May 2014, and of the lower portion of the landslide on 23 and 25 May 2014

During the reconnaissance, team members recorded key features and observations using both traditional manual and GPS-assisted mapping methods. Additionally, all key features were captured using geo-referenced digital photographs. A Gigapan robotic imaging system (see www.gigapan.com for complete details) was used to record gigapixel panoramic digital images at 15 different vantage points. The gigapan images have a resolution that is approximately 1000 times that of High Definition Television (HDTV) [Frenkel 2010]. These images can be openly viewed using Gigapan's on-line viewer. See the following page for direct links to the Gigapan images.

Reference

Frenkel, K. (2010) Panning for Science, *Science*, DOI: 10.1126/science.330.6005.748

GEER Oso Landslide Investigation: Gigapans Imagery Log

Reference Number	Coordinates	Approximate Center Bearing	Notes	Date Acquired	Gigapan link
1	48.277077°, -121.840187°	320 deg	Distant view toward head scarp	13-May-2014	http://www.gigapan.com/gigapans/17bc6af9bdf865dd3871003d7b145184
2	48.277077°, -121.840187°	20 deg	Downslope view to east runoff area	13-May-2014	http://www.gigapan.com/gigapans/8a308bb04e5bcc2ea4366b913e8d0b8
3	48.276863°, -121.840942°	270 deg	Downslope view to west runoff area	13-May-2014	http://www.gigapan.com/gigapans/25736e9c0b706500b71036e8e654a57
4	48.278484°, -121.842712°	320 deg	Lower mid-slope view toward head scarp	13-May-2014	http://www.gigapan.com/gigapans/0df7e3ca6667a5e8220a6f3d6cad1493
5	48.278461°, -121.842766°	270 deg	Lower mid-slope view of hummocky debris field	13-May-2014	http://www.gigapan.com/gigapans/e9893c39659965d45d57594c838787a8
6	48.278336°, -121.842834°	200 deg	Lower mid-slope view toward west runoff area	13-May-2014	http://www.gigapan.com/gigapans/ff69716c3692de0299cacff30282cf55
7	48.278179°, -121.842613°	110 deg	Lower mid-slope view toward middle-east runoff area	13-May-2014	http://www.gigapan.com/gigapans/1dc6ad64e75f922dec29f439c3e02205
8	48.286289°, -121.852844°	132 deg	Overview from head scarp	15-May-2014	http://www.gigapan.com/gigapans/4011966490129a5d27ea8094fca8ec5c
9	48.28641°, -121.84906°	213 deg	Overview from upper east flank	15-May-2014	http://www.gigapan.com/gigapans/156395
10	48.28505°, -121.85072°	313 deg	Head scarp detail from upper middle	15-May-2014	http://www.gigapan.com/gigapans/89960324599124f33d90de74a082a244
11	48.28263°, -121.85068°	105 deg	Overview from upper west flank	15-May-2014	http://www.gigapan.com/gigapans/865a4ba760f9a6fb732680d2e8c536ab
12	48.28148°, -121.8427°	35 deg	View of east flank runoff area	24-May-2014	http://www.gigapan.com/gigapans/fbbf1766b8ffa2cc3437e6d5a9786002

13	48.28144°, -121.84271°	283 deg	Mid-level view toward west scarp	24-May- 2014	http://www.gigapan.com/gigapans/cde713b7063c71c7412f29819bdb6a55
14	48.28152°, -121.84271°	300 deg	Mid-level view toward head scarp	24-May- 2014	http://www.gigapan.com/gigapans/c7c8b5255b3362817b18e398423a7f29
15	48.28101°, -121.84272°	144 deg	View of river- downcut of landslide deposits on south side of river	24-May- 2014	http://www.gigapan.com/gigapans/7a4d8795f86cfeae98e4f4e4e0335d7c

Note: Gigapan Images Copyright 2014 Joseph Wartman (wartman@uw.edu)